Centrifugally Stiffened Rotor

Eternal Flight as the Solution for 'X'

NIAC Phase I Final Report

Principal Investigator
Mark D Moore
Aeronautics Systems Analysis Branch
NASA Langley Research Center
mark.d.moore@nasa.gov

Controls Research Lead
Justin M Selfridge
University of Virginia (UVA)

Aerodynamics Lead
Sean Brown
National Institute of Aerospace (NIA)

Experimental Prototype Lead
Todd Hodges
National Institute of Aerospace (NIA)

October 6th, 2014

Table of Contents

Chapter 1

Introduction

Flight has always captured man's imagination. This is evidenced by the great variety of aerial vehicles that exist today. Everything from fixed-wing to rotorcraft; satellites to spaceships; mono-wing to quadrotor. However, despite the wide variety of flying vehicles, not one of them has attained eternal flight. Accomplishing this feat is one of the great challenges still facing the aviation community.

Motivation

Achieving eternal flight opens the doors to atmospheric satellites. Existing satellites have a great number of capabilities that enrich our lives; however, their distance from the surface of the earth precludes certain types of transmission capabilities. Once eternal flight is achieved, that vehicle can serve the same role as ordinary satellites, but its close proximity will allow for real time two way communications, like wireless broadband internet. And with active controls, atmospheric satellites would not be constrained to geosynchronous orbits, like our existing satellite technology.

Objective

Many projects are under way to achieve this goal; however, most of these research efforts follow the same design methodology, and have exhausted the limits of this particular design. This concept introduces a completely new aerial vehicle structure, which uses the best features of fixed-wing and rotorcraft designs. Combining the best features of different classes of aircraft, expands the capabilities beyond what either one can achieve on its own.

Outline

This research introduces a revolutionary concept vehicle that shows great promise in achieving eternal flight capabilities. This chapter introduces the concept vehicle and outlines its features and benefits.

Section 1.1 presents the *Executive Summary* which outlines the past and present state of satellite technology. Current efforts are under way to expand these capabilities, but an alternative approach is required to achieve the objective.

Section 1.2 describes the *Goal of Eternal Flight*. Different types of satellites provide various functions, but a technology breakthrough is essential to satisfy the existing commercial interest.

Section 1.3 outlines the *Mission Objective* which decomposes the problem. It illustrates the majority of existing concepts are based on Human Powered Aircraft designs, and describes several competing designs currently underway.

Section 1.4 presents the *Technical Challenge* of eternal flight. It shows that improvements in energy capture and energy storage alone are not enough to attain the goal.

Section 1.5 introduces a new *Concept Approach*

called the Centrifugally Stiffened Rotor (CSR). It provides an overview of the concept vehicle and describes the individual components.

Section 1.6 performs the *CSR Feasibility Analysis*. It outlines the benefits of centrifugal stiffening, and illustrates how the CSR achieves high Lift to Drag ratios with low parasitic drag.

Section 1.7 conjures up *Unique New Missions* applicable to this concept vehicle. Low disk loading, large swept areas, and a stationary hub, make this attractive for several different types of projects.

1.1 Executive Summary

Satellites have fundamentally changed our lives, providing dramatic improvements to our quality of life that could have been accomplished in no other way. New research efforts are attempting to satiate demand for increased capabilities, but no existing platform has fully achieved eternal flight. This research presents a novel alternative approach, which exceeds existing capabilities, outpaces current research efforts, and may be the answer to attain eternal flight.

1.1.1 Existing and Future Demand

Over the past 50 years, satellites provided worldwide telecommunications to connect the world, geopositional navigation to permit precise location determination, and imaging and sensor systems that have let us develop a depth of understanding of our planet as well as the entire universe. While incredibly expensive, and by far the most expensive aerospace products on a dollar per pound basis, their unique ability to provide a "God's eye view of the world" also provides productivity that is difficult to match.

Yet there is need for even greater capabilities, and at lower costs. Society has developed an increased appetite for omnipresent communications and surveillance capabilities, but with the added desire for these services to be achievable in real-time as on-demand services. These new capabilities are not well met by existing satellites, but instead require a new solution that can achieve several orders of magnitude lower signal latency, with greater operational flexibility, while at dramatically lower cost.

1.1.2 Present Research Efforts

The question this study asks is whether a new form of satellites is possible, and proposes a unique advanced concept approach which has never been previously explored. Low Earth Orbit (LEO) satellites are about 50x closer than Geosynchronous (GEO) satellites; Atmospheric Satellites (AT-Sats) are another 50x closer than LEO satellites.

AT-Sats are aerial platforms that operate at altitudes of around 60,000 feet where air density and winds aloft offer the operating conditions requiring the lowest power without weather concerns. Several concept approaches have been developed over the past decade through efforts such as DARPA Vulture and ISIS. Each of these DARPA programs exceeded $150 million, and had the intent of achieving a large-scale flight demonstrator. Vulture researched High Altitude Long Endurance (HALE) fixed wing concepts that utilized ultra-lightweight structure techniques pioneered in Human Powered Aircraft (HPA). ISIS researched HALE airships that use Lighter-Than-Air (LTA) structures and buoyant gases.

Both approaches applied advanced solar cells to provide a renewable energy source with the objective of staying aloft for years at a time. Both of these programs were cancelled due to lack of feasibility in closing the day-night energy balance required for staying aloft without excessive altitude loss. Because of this, new concept approaches are desired that can achieve lower cruise power requirements to remain airborne throughout the year, even at high latitudes, while accommodating seasonal wind and solar flux variations.

1.1.3 Alternative Approach

A novel vehicle concept approach was developed with the objectives of achieving a 50% reduction in the structural mass while maintaining a robust structural configuration, as well as enabling a 33% increase in the Lift to Drag ratio. The approach uses the tensegrity principle to attempt to put as much of the structural loads into tensile load paths, where advanced carbon composites provide incredible strength to weight, while minimizing compression load paths. The method to achieve this is to

rotate several wings around a stationary hub at very large diameters via a tether at quite low airspeeds, but with a concentration of the large battery mass required for night energy storage at the outer extremities. The concept is called the Centrifugally Stiffened Rotor (CSR) because the resulting centrifugal forces applied to the tether and wing limit the bending through in-plane stiffening.

Three rotor-wings rotating around the hub provide maximum concentration of centrifugal force, with a minimum number of wings to form a stable planar summation of forces and moments. Because of this structural stiffening, wing aspect ratios (the ratio of span to chord length) can be dramatically increased while using thin airfoil sections to achieve extremely low levels of induced and parasite drag.

Traditional rotors achieve poor aerodynamic efficiency because of poor, triangular span loading due to a linearly decreasing velocity distribution across the rotor that results in high induced drag. However with this concept, the large radius of rotation of the rotor-wings with the tether comprising the inner 80% enables the rotor-wings to achieve elliptic span loading. The tether takes advantage of advanced aerospace grade compressed Spectra providing incredible strength to weight at small cross-sectional tether diameters that result in less than 10% of the drag being associated with the tether.

Aerodynamic efficiency is further increased by taking advantage of a highly synergistic Outboard Horizontal Stabilizer (OHS) configuration layout to achieve thrust instead of drag from the tail pitch trim surface. Another favorable aerodynamic characteristic of the CSR concept is that since the outer rotor-wings are producing the lift and the inner hub is stationary, large payload volumes can be incorporated into the center hub without incurring drag from the "cruise speed" required for lift generation.

1.1.4 CSR Evaluation

New tools were required to analyze this concept since this rotating multibody approach is far outside of existing aeronautic systems analysis tool capabilities. Initial performance and aerodynamic analysis results of the CSR concept indicate compelling advantages for this approach in comparison to existing Vulture HPA flying wing solutions. LTA airships were not compared because prior studies have shown those approaches are unable to provide station keeping capability for a large portion of the year due to winds aloft, and the high parasite drag associated with the large volumes required at high altitude for buoyancy.

While the CSR concept performance results are compelling and indicate feasibility to achieve day-night energy balance, the key concept risk identified early on is the ability to maintain control of the multibody dynamics that are inherent in the design. Therefore, the majority of project scope focused on performing detailed control modeling and simulation of the system with non-ideal, real world disturbances which introduce dynamic instabilities. The control efforts are discussed in detail, as this is a very unique multibody controls problem with methods developed that can be applied to other problems of interest, such as asteroid capture with tethered systems.

In order to validate the developed control algorithms, a subscale prototype testing effort has been initiated. The CSR subscale experiment will establish control feasibility, but was outside of the scope of this Phase I study and therefore is only outlined at the end of this report. The CSR controls effort has led to a PhD topic by the lead control researcher, which will be completed in the following months as part of his final dissertation.

1.2 Goal of Eternal Flight

A variety of existing satellites fulfill different technology roles. Corporations have shown a sincere desire to expand the realm of satellite capabilities, to meet their ever expanding needs.

1.2.1 Technology Breakthroughs

Google initiated a "Solve for X" conference in 2012 (https://www.solveforx.com), to engage in radical moonshot visions where *Huge Problems* intersect *Breakthrough Technologies*. Such ideas are already being developed in the little known Google-X Lab, and have started to achieve huge impacts in technology and mission areas that are critical to aerospace.

The Google "Driverless Car" is one of these

breakthrough attempts to turn-on-it's-head the preconceived notions of what is not only possible, but what we will soon wonder how we ever lived without. Google has already achieved what critics said would be a 'hard stop' to such idealistic visions by making robotic cars legal in 4 states; with almost every auto company now mirroring their autonomy goals.

The "Solve for X" conference has many themes congruent to NASA's mission; such as *Cheaper Satellite Pictures*, *Low Power Broadband Wireless Everywhere*, *Inexpensive Renewable Energy*, and *Reversing Climate Change*. What if an aerospace mission concept had the potential to achieve all these moonshot goals? What if NASA could show the potential to dramatically impact many of the top national challenges with a single mission concept path and technology suite? How could this be possible...?

1.2.2 Expanding Needs

The first satellite was placed into orbit in 1957, and within 15 years satellites became highly capable platforms providing essential services through standardized satellite bus designs. Satellites have fundamentally changed our lives, providing dramatic improvements to our quality of life that could have been accomplished in no other way. Over the past 50 years, satellites provided worldwide telecommunications connecting the world, geopositional navigation permitting precise localization, and imaging and sensor systems that let us develop a depth of understanding of our planet as well as the entire universe.

While incredibly expensive, and by far the most expensive aerospace products on a dollar per pound basis, their unique ability to provide a "God's eye view of the world" provides productivity that is difficult to match. Yet there is need for even greater capabilities, and at lower costs. Society has developed an increased appetite for omnipresent communications and surveillance capabilities, with the added desire for these services to be achievable in real-time as on-demand services. These new capabilities are not well met by existing satellites, but instead require a new solution that can achieve several orders of magnitude lower signal latency, with greater operational flexibility, while at dramatically lower cost.

1.2.3 Geosynchronous Satellites

Geosynchronous (GEO) satellites are able to remain over a fixed location above the Earth for continuous surveillance or communication across a large coverage area because of their extreme distance. Because of their distance away from the Earth's surface, a long transmission delay (or signal latency) occurs. This delay makes the use of GEO satellites for two way communications impractical; however, can provide a large, constant coverage area with one way communications with great effectiveness. Due to the large transmission distances, the power required is considerably increased due to power loss being inversely proportional to the transmission distance. With such a broad coverage area, frequency reuse is extremely limited. Coverage at high latitude locations is challenging due to very low looking angles from the satellites, which increases signal obstruction and losses from building, trees and mountains.

1.2.4 Low Earth Orbit Satellites

Low Earth Orbit (LEO) satellites are significantly closer proximity to Earth, with a decrease in coverage area, but lower signal latency. However, LEO satellites are required to constantly orbit, and are unable to maintain a fixed reference location above the Earth. This necessitates large fleets of LEO satellites to maintain continuous coverage over any specific location, with very high associated capital costs for both the satellites and the cost to launch and insure the satellites. While the signal latency is reduced, it is still extremely challenging to use for two-way digital data transmission with an inability to achieve broadband speeds.

1.2.5 Atmospheric Satellites

Atmospheric satellites (AT-Sats) are a new breed of aircraft that operate at altitudes around 60,000 feet, where air density and winds aloft offer operating conditions that require the lowest power without weather concerns. AT-Sats operate over relatively fixed locations for continuous coverage with a single vehicle. Because of their proximity to Earth, the signal latency is extremely low, along with the trans-

mission power required (enabling the entire payload to shrink in size). The coverage area is greatly reduced, essentially down to the size of a single urban area with the most direct lines of communication or the size of several states for the full coverage area. Since the aircraft is able to takeoff and land, the cost of deployment (and recovery) is very low, with the added ability to upgrade and refurbish satellite payloads as equipment ages. Likely the total system costs of AT-Sats are several orders of magnitude less than other satellite solutions, however current High Altitude Long Endurance (HALE) aircraft are only able to maintain flight for several weeks at a time, and lack the ability to provide the highly reliable and persistent capabilities that satellites offer.

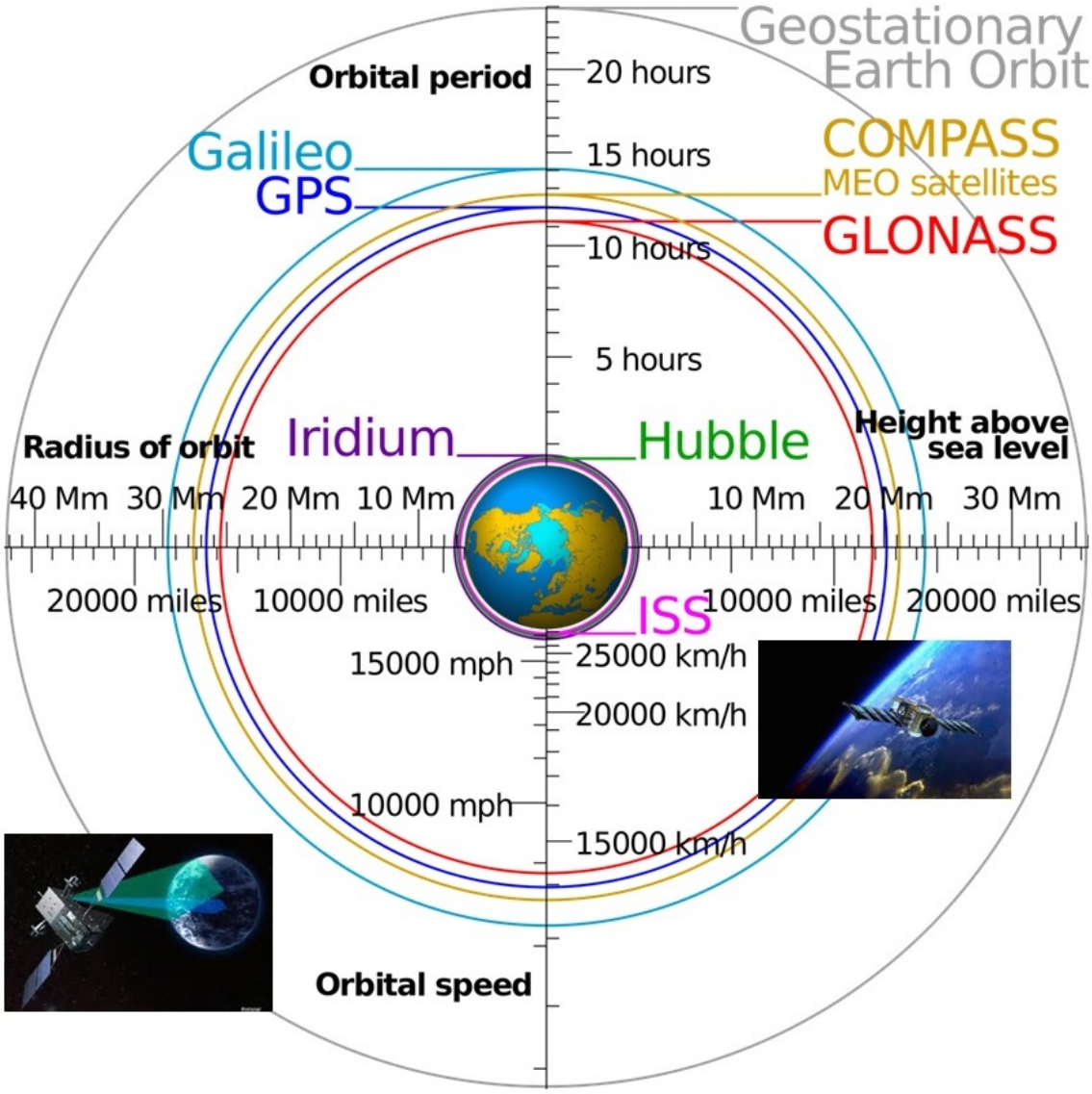

Figure 1.1: Existing GEO/LEO satellite orbit: height above Earth, period and speed.

Satellite	GEO	LEO	AT-Sat
Example	XM Ecostar	Motorola Iridium	AV Global Observer
Distance above Earth (mi)	22,230	500	10
Coverage Diameter (mi)	7926	2300	500
Fleet Required	1	50-60	1
Satellite Cost	$300M	$50M x50	< $20M
Launch & Insurance Cost	$100M	$25M x50	< $1M
Ideal Signal Delay	> 250	5-40	0.1

Table 1.1: GEO, LEO, and AT-Sat comparison.

1.2.6 Commercial Interest

Satellite solutions vary in their strengths and weaknesses, with each type providing value. The orbits of existing satellites is depicted in Figure 1.1. GEO satellites offer a continuous capability with a single satellite, LEO offers 50x closer proximity for improved single latency, power requirements, and imaging resolution. AT-Sats offer another 50x closer proximity than LEO satellites for even better latency, power, and resolution; while also offering reusability and extremely low capital costs. The summary in Table 1.1 provides a comparison between the different varieties of satellites.

Referring back to two of the highest priorities of Google's "Solve for X" challenges, *Cheaper Satellite Pictures* and *Low Power Broadband Wireless Everywhere*; AT-Sats offer an incredible match to these desired goals. Just within the period of this Phase I study, both Google and Facebook have entered into AT-Sat development, with each purchasing aerospace companies focused on aircraft for this mission. Google purchased Titan Aerospace in April, 2014 (http://techcrunch.com, 2014/04/14, *Google Acquires Titan Aerospace, the Drone Company Pursued by Facebook*), with Facebook buying Ascenta (a spin-off of the QinetiQ Zephyr project) in March, 2014 (http://www.theguardian.com, 2014/03/28, *Facebook Buys UK Maker of Solar Powered Drones to Expand Internet*).

Google also initiated test flights from their Google-X Lab Project Loon this year, which utilizes a large network of balloons that drift with the winds while using limited directional control by changing the buoyancy (and resulting altitude which have different wind speeds and directivity). The Project Loon approach is severely limited as it requires uncontrolled flight over countries, and is therefore only being tested in the southern hemisphere. The balloons also only have a flight duration of 50 to 100 days before requiring descent and payload pickup, with the trajectories starting at the most southern latitudes and spiraling their way eventually to the equator with the prevailing winds. Clearly these investments showcase the interest that exists in developing alternative platform solutions to satellites.

1.3 Mission Objective

Several research groups, both commercial and government sponsored, are attempting to design feasible AT-Sat solutions which achieve eternal flight. The problem reduces down to an energy balance relationship, where HPA techniques dominant the majority of current design paths.

1.3.1 Problem Decomposition

The basic problem of AT-Sats is decomposed into *Power Required = Vehicle Drag* x *Flight Velocity*. Thus, to minimize the power required to remain aloft, both the vehicle drag and flight velocity need to be minimized.

Minimizing drag means flying at the highest cruise altitudes where the Lift to Drag (L/D) ratio is maximized. Altitudes where the air density is low, but not so low that there is insufficient density to maintain flight. High structural efficiency is achieved with lightweight motors and system components, as well as with high efficiency components that experience the least energy losses.

The key determining factor for vehicle feasibility is based on achieving *Energy Collected in Daylight* >

Energy Expended During Night Operation + Energy to Maintain Flight. Maintaining this energy balance is most difficult during the winter months at high latitudes, where there is low solar flux and low incidence angles on the solar cells. Wind velocities are minimized by operating at altitudes between 60 and 70 thousand feet. However, even operating at these altitudes, when considering greater than 99% of days, the winds aloft can reach 120 miles per hour.

1.3.2 Human Powered Aircraft Approach

Conventional Human Powered Aircraft (HPA) concepts are able to achieve L/D ratios of about 35 at optimal aspect ratios of around 25. The aspect ratio is a dimensionless parameter that tracks the span to chord ratio of the wing and is defined as span squared divided by the wing area. L/D is an effective metric for tracking the overall aerodynamic efficiency that includes the parasite drag (skin friction drag associated with wetted area) and induced drag (both 2D and 3D pressure and vorticity drag sources resulting from creating lift).

The resulting payload mass fractions of the HPA inspired aircraft is less than 5%, with about 45% of the mass required for the structure and about another 45% allocated for the propulsion system, all while using the most advanced solar cell and battery technologies. The growth factor (a dimensionless weight sensitivity parameter that compares the resulting increase in vehicle weight that results from increasing the payload weight by one pound) of such concepts are quite high, which is an indicator that the feasible design space is quite restricted.

1.3.3 Best In Show

The current world record holder for High Altitude Long Endurance (HALE) flight was set four years ago by the QinetiQ Zephyr 7 aircraft. Figure 1.2 illustrates this vehicle, along with the other concept approaches currently pursued. The Zephyr is a HPA inspired structure that maintained high altitude flight for a two week period in midsummer in New Mexico. The aircraft was 110 pounds, with a wing span of 74 feet, and had a wing loading of less than 1 pound per square foot. The payload was less than 5 pounds, and while the Zephyr achieved 70,741 feet during flight, it was not able to maintain altitude during night operation. Essentially, the aircraft used its altitude as potential energy during night operation, when energy was being used from the batteries which had been stored from the solar cells during day light operation.

AT-Sat operational products cannot utilize such altitude energy storing. Lower altitudes limit communication line of sight and weather effects impede the ability to station keep. The Zephyr is highly reflective of all the other aircraft concept approaches currently pursued and provides many indicators relating to future concept feasibility.

The Zephyr was only able to maintain flight for two weeks because they used the most advanced lithium-sulfur batteries. The batteries were capable of about 530 Watt hours per kilogram, which is more than twice the specific energy of any other lithium rechargeable batteries at that time. Lithium-sulfur chemistry only permits up to approximately 20 recharge cycles before seriously degrading their specific energy. Also, they are only capable of providing very low power discharges rates below a 1 C rating, where C is the battery rating that relates to how quickly a battery can discharged in comparison to its charge time, and a 1 C rating means the discharge rate can only be as high as the charging rate.

By far, the two largest mass fractions for the Zephyr were the batteries and wing spar. Since HPA structures have done everything possible to achieve ultra-lightweight structures for conventional flying wing configurations, the major focus for research programs such as DARPA Vulture has been to optimize the energy system. These efforts currently focus on high specific energy regenerative fuel cells (energy storage) and high efficiency/lightweight solar cells (energy capture). The Zephyr project has just recently been purchased by Airbus (http://defense-update.com, 2014/04/25, *Airbus Invites Partners to Test Mission Payloads with Zephyr 8 'Pseudo-Satellite'*) and a new Zephyr 8 is under development as a follow-up next generation airframe.

Figure 1.2: Current HALE AT-Sat approaches under development.

1.3.4 DARPA Concepts

Several concept approaches have been developed over the past decade through efforts such as DARPA Vulture and ISIS. Each of these DARPA programs exceeded $150 million, and intended to achieve a large-scale flight demonstrator.

Vulture researched HALE fixed wing concepts that utilized ultra-lightweight structure techniques pioneered in HPA, where concepts follow design and construction techniques pioneered by Paul Macready with the Gossamer Albatross 35 years ago. The aircraft have very low wing loading which provides substantial surface areas for solar cells, and minimizes the cruise velocity and required power. The structures are extremely delicate with Mylar surfaces for much of the wing surface, but they still have huge root bending moments absorbed through these thin wings. This approach results is a relatively small payload and has great sensitivity to winds.

ISIS researched HALE airships that use Lighter-Than-Air (LTA) structures. LTA concepts utilize enormous hydrogen/helium filled vehicles to achieve a difference in buoyancy between the internal volume, and the already very low density air at high altitudes. Such large volumes require equally large surface areas. If winds aloft could be ignored, such approaches would be ideal. However during the majority of the yearly seasons, and at the majority of latitudes, LTA approaches yield such high drag that the power requirements at even modest winds exceed a feasible solution.

Both approaches applied advanced solar cells to provide a renewable energy source with the objective of staying aloft for years at a time. Both of these programs were canceled due to lack of feasibility in closing the day-night energy balance required for staying aloft without excessive altitude loss. Because of this, new concept approaches are desired that can achieve lower 'cruise' power requirements to remain airborne throughout the year, even at high latitudes, while accommodating seasonal wind and solar flux variations.

1.3.5 Commercial Concepts

Clearly a great deal of momentum and interest is building in AT-Sat vehicle development, with a focus by all (except the Google Loon Project) on conventional HPA conventional wing configurations. Several variants of wing-tail configurations are shown in Figure **??**, but each concept maintains a highly similar HPA structural approach while span-loading the vehicle weight across the span as much as possible to decrease the wing bending moments.

Lockheed utilizes a bottom strut across the fuselage element to achieve greater effective wing spar depth; however, without trussing between the fuselage elements this approach does not provide significant improvement. Furthermore, wire crisscrossing trusses between each fuselage element at flight speeds would dramatically increase drag.

Aurora utilized a combinatory Z-wing arrangement. Each wing element would dock together in flight with a hinge element that does not transmit bending moments. Also, each wing element would fly at inclination angles better suited to capture the solar flux for energy storage.

Boeing utilized an Outboard Horizontal Surface (OHS) to minimize the induced drag and augment the pitch trimming capability. Only Boeing was selected for the Phase II DARPA Vulture program. However, after detailed studies, this concept showed questionable feasibility and was descoped into a focused effort to advance the energy storage and capture technologies.

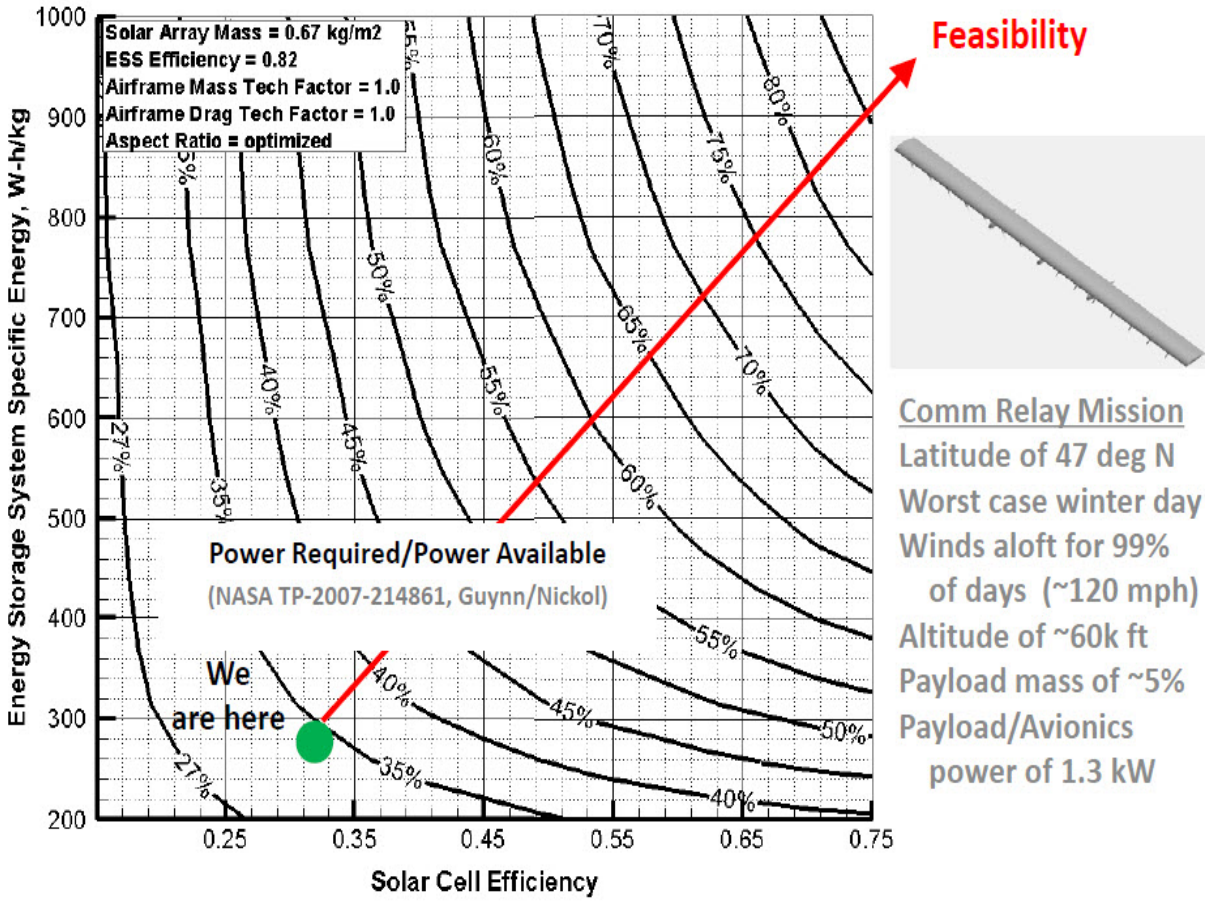

Figure 1.3: Pareto sensitivity frontier of energy required compared to energy available.

1.4 Technical Challenge

A number of improved technologies are required to achieve feasible AT-Sat operational capability. Key advances are required to increase reliability, decrease payload weight, and expand current energy collection and capture efficiency.

1.4.1 System Reliability

One such topic area includes achieving satellite-like reliability. Enabling continuous flight for a year or more requires confidence across all aircraft components. This reliability must be accomplished in all systems including: energy storage, control surface actuators, flight control avionics, and sensors that provide an autonomous flight capability.

1.4.2 Light Weight Antennas

Another technology area includes ultra-lightweight antenna systems. While targeting eternal flight, these improved systems can minimize the payload weight. Phased-array multi-beam systems of 10 or even 100 beams will likely be required for cell phone providers to support 100,000 concurrent lines for millions of customers within the coverage area.

1.4.3 Energy Capture and Storage

Performing technology sensitivity analysis of the conventional wing configurations helps to understand why DARPA descoped the Vulture program. Examining all these sensitivities is beyond the scope of this Phase I study. However, NASA/TP-2007-214861 (High Altitude Long Endurance UAV Analysis of Alternatives and Technology Requirements Development) is an excellent source that provides comprehensive understanding.

A key result from this study is a Pareto technology frontier chart that shows the sensitivities of the two primary energy parameters: collection and storage. Figure 1.3 presents the Pareto sensitivity frontier of the energy required compared to energy available for completing a day/night cycle during the worst winter day conditions. They are specified as a function of the specific energy of the energy storage system and the solar cell efficiency. The infeasibility of this mission concept at current technology levels is clearly seen with only about 34% energy available versus energy required for accomplishing a day/night cycle on the worst winter day.

Currently, lightweight thin-film solar cells are at 32% efficiency (Micro Link Devices) and the best lithium rechargeable batteries that are capable of at least 365 cycles (one year of operation for an AT-Sat) are nearly 280 Whr/kg (Panasonic/NCR cells with the 18650 form factor).

If energy storage and solar cell technology are the only improvements provided for future AT-Sat vehicles, the required feasibility to achieve a 100% energy balance requires battery specific energies greater than 1000 Whr/kg and solar cells that exceed 75% efficiency. Therefore, it is highly desirable to not only focus technology development efforts on improved energy, but also on a new concept approach that could dramatically lessen the energy required for sustained high altitude flight.

1.5 Concept Approach

The proposed concept has never been attempted before. This vehicle is a new approach that dramatically lowers structural weight, greatly reduces drag, and provides a far more robust structure in weather than existing HPA structures. The approach uses three extending and retracting tethered wings which rotate around a stationary central hub, and the rotation balances all the forces and moments within the system. Figure 1.4 depicts the vehicle, and a detailed description is provided below for each of the three major components: the rotor-wing satellite components, the central stationary hub, and the tethers that connect them together.

1.5.1 Rotor-Wing Satellites

All the controls, and the majority of the vehicle mass is located within the rotor-wing satellites. This section provides the general description of these structures, why three arms are used, and how they impart controls on the entire CSR system.

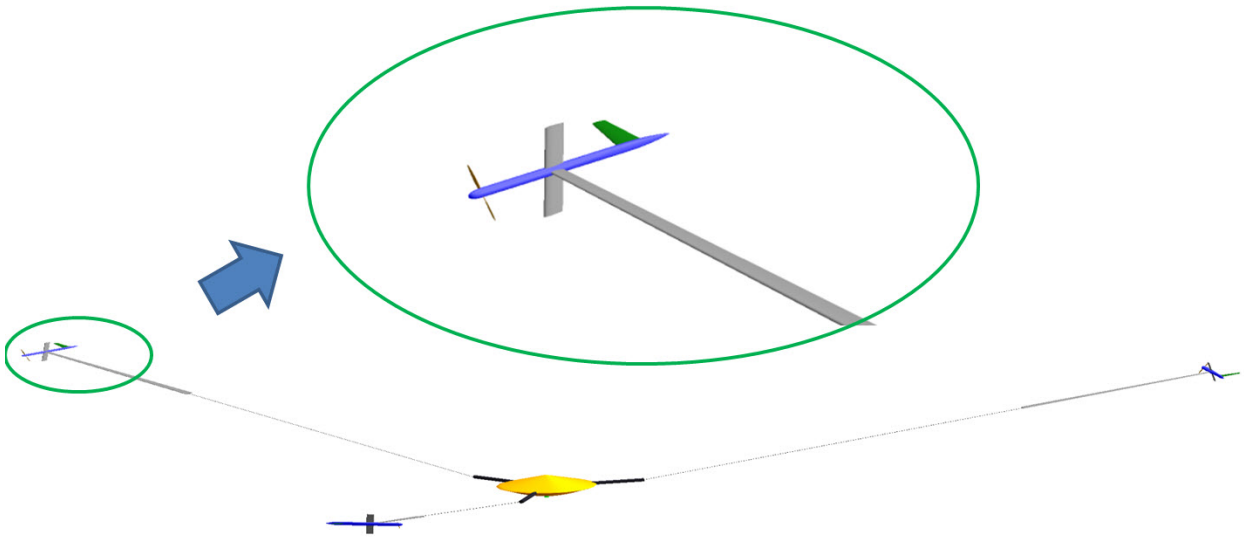

Figure 1.4: Centrifugally Stiffened Rotor (CSR) concept, with zoomed in view of the rotor-wing.

General Description

Three rotor-wing satellites are coupled together through a high tensile, small diameter cable tether. This number provides the least number of rotor-wing satellites necessary to achieve a stable and controllable tip path plane, while achieving the maximum tether centrifugal force. The rotor-wing satellites are located at the ends of each tether, and provide all the lift, propulsion and control for the CSR system.

Approximately 80% of the entire vehicle system mass is located in these components, which is dominated by the battery mass required to provide energy during night time operation without altitude loss. The battery mass is located at the outer fuselage to maximize the centrifugal force and provide stiffening of the rotor-wing structure and alleviate the bending moment that is exerted on the rotor-wing spar.

Each wing-body is driven by a propeller with optimum twist and pitch for the rotation rate. Since the rotor-wing thrust force is a tip driven system, there is no torque transmitted back to the central hub. This propulsion technique is opposite that of a conventional helicopter rotor, where a torque is applied to the central shaft. This requires the need for a counter-torque on the traditional helicopter body to prevent the helicopter body from rotating in the opposite direction. There have been many examples of tip-driven helicopters in the past that have avoided the need for a tail rotor.

Why Three Arms?

More than three satellites could be used, but it would result in a poorer performing system. A system of three components maximizes the rotor-wing Reynolds number along the chord, which is an important factor for achieving the lowest drag with HALE aircraft. Additional rotor-wings would also spread the battery mass to more components. This results in a lower centrifugal force, which is the key method for alleviating the bending moment seen by the rotor-wing spar.

Centrifugal stiffening also allows for relatively thin wing airfoils to achieve increased laminar flow. These thinner airfoils are only possible due to the inherent wing stiffness associated with the centrifugal stiffening. Additionally, a lower centrifugal force (mass x velocity^2 / radius) on the rotor-wing-body component results in a higher bending moment. A higher centrifugal force could be achieved with a higher rotational velocity of the rotor-wing, but this is not desirable as the required power would increase. Therefore, the design objective positions the major-

ity of the vehicle mass as far outboard along the radius of rotation as possible, while maintaining a low rotor-wing speed.

Having more than three rotor-wing satellites also increases the difficulty of maintaining control of each element, because each component can independently vary the lift, thrust, and radial force. More elements may provide increased control robustness (through having the rotor tip path plane over constrained), but at the cost of both the vehicle performance and hub complexity.

When wind conditions are present, each satellite will operate at different speeds. One element is essentially acting in a retreating blade condition, while another is acting in an advancing blade condition. Therefore, the thrust of each element in wind conditions varies throughout each cycle, and the azimuthal locations of each satellite element is non-equally spaced. Proving that the entire multibody vehicle system can maintain control is a key uncertainty of this concept that needs to be answered.

Controls Overview

Each rotor-wing is covered with thin film solar cells to collect solar energy during daylight hours. This provides power to the propulsion system for thrust, which permits the rotor-wings to rotate, and to keep the vehicle aloft. Each satellite includes an electric motor and propeller in the nose of the body for propulsion. Control surfaces are oriented vertically and horizontally to maintain vehicle control.

Pitch control of each wing changes the angle of attack of each individual wing. This is accomplished by a surface extending outward from the wing, and in the same plane as the wing. This pitch trim surface is the equivalent of a tail on a conventional aircraft; however, it operates in the wing wake vortex upwash, so the required angle of attack decreases and the drag is further reduced by providing increased spanwise efficiency. When all wing pitch trim surfaces change together, they provide the equivalent of helicopter collective pitch which increase or decrease the altitude of the vehicle.

Roll control of the entire vehicle system is accomplished by changing the pitch of each rotor-wing differentially. This achieves the equivalence of cyclic pitch change of a helicopter rotor, and enables the tip path plane to either tilt side-to-side or back-to-front. Yaw control is unnecessary for this vehicle since there it is axisymmetric about the center of rotation, and because the rotation is induced at by the wingtip propulsors. When winds are present, the entire vehicle system is angled through differential lift to provide an angular incidence between the forward wind direction and the effective tip path plane of the rotor-wings to provide forward thrust to keep the vehicle in place.

A vertical surface is located on the body at the end of each rotor-wing in a similar fashion to a winglet, but extending both upwards and downwards from the wing. This surface provides the ability to augment or decrement the centrifugal force to provide stability across the different rotor-wing elements through a force that is independent of the rotation rate or thrust.

The method of control for the entire multi-body vehicle system is envisioned where the azimuth location of each element is known to a controller through wireless signals communicated between each element. However, this may not be necessary and this is discussed in detail in the control development section of this report.

1.5.2 Central Hub Payload

While the center hub is described as stationary, it is permitted to rotate at the extremely slow angular rates of the vehicle. Even for small Unmanned Aerial System (sUAS) scales of 55 pounds the rotational rate is less than 20 rpm and for larger satellite systems the rates are less than 5 rpm.

The hub is located at the center of rotation and provides a payload pod independent of the wing cruise speed (i.e. large volume antenna pods that only result in drag during wind conditions). Since the tethers are operated with a large radius of action spanning hundreds of feet, the rotor rotation rate is quite low, with the payload rotating at that same low rate.

The mass of the center pod is around 20% of the total vehicle mass, so the tether angle is relatively small ($<15^\circ$) due to the centrifugal force balancing. Solar cells on the center hub provide the payload

energy, along with the potential to transmit electricity through the tether to the props depending on whether a more complex tether is warranted in case the optimal wing-rotor sizing does not permit sufficient solar cell area for propulsion purposes. However, a conductive tether is significantly larger diameter and results in higher tether drag and weight.

The hub has structural arms where each tether extends from the center section to provide rotation rate stability across each rotor-wing-body component. Specifically if one rotor-wing gets ahead of the others, a restoring angular force will be induced that slows that wing, while an angular force is induced on the other rotor-wings that accelerate the other rotor-wings that are lagging behind. These structural arms hold the tether, and act as 'whips' to induce these stabilizing rotational forces across the entire wing/rotor system. While independent thrust at each rotor-wing permits differential spacing of the elements, the tether structural whips provide a mechanism for incurring a stabilizing force across the system of elements.

1.5.3 Tethers

The tethers connect the rotor-wings to the center hub. Because the vehicle is always in rotation, it only experience tensile loading. This is ideally suited for advanced composite and braided materials designed specifically for high tensile strength, like Spectra. The tether can be reeled in to achieve a compact configuration for takeoff and landing. But this configuration requires significantly more power due to the higher velocities needed to maintain lift and from the non-optimal triangular lift loading distribution across each wing.

In flight, the tether is reeled out to provide a dramatically larger radius, which results in a toroid lift area and an optimal elliptical lift loading distribution across each wing. The amount of area the rotor-wing traverses is the effective disc loading of the vehicle and determines the power required. The tether comprises the inner 70 to 80% of the total diameter when in flight, depending of the optimized wing sizing for different mission needs. The tether is at a slower velocity than the rotor-wing, where the average tether velocity is only 35-40% of the rotor-wing speed. This means that only about 5 to 10% of the total drag of the vehicle comes from the tether. For example, a 0.03" diameter compressed aerospace grade Spectra has a tensile strength of 200 pounds.

1.6 CSR Feasibility Analysis

Having described the general concept of the CSR vehicle, the next task describes the feasibility of this system achieving eternal flight. This section describes the benefits of centrifugal stiffening, and how the CSR achieves high L/D ratios while minimizing parasitic drag. It compares this concept with the leading competitors, and illustrates the distinct advantages this concept offers.

1.6.1 Benefits of Centrifugal Stiffening

The first goal of the CSR concept is to achieve a large reduction in the wing spar mass fraction of the total vehicle mass, which increases the structural efficiency. Another objective is to increase the Lift to Drag ratio, which increases the aerodynamic efficiency of the HALE aircraft. These goals are primarily required for station keeping missions. The CSR system achieves these goals through centrifugal stiffening, just as a helicopter rotor uses CF which allows extremely high aspect ratio blades while using very lightweight rotors.

Most rotorcraft blades have aspect ratios of 30 to 50, but the majority aircraft rarely exceed an aspect ratio of 10, due to the high resulting weight of the wing and aeroelastic constraints. Rotor blades, which develop all the lift of a helicopter, typically weigh only 2 to 3% of the gross helicopter weight. Compare that to aircraft wings which are typically 10 to 20% of the gross aircraft weight. HALE aircraft experience a similar wing weight mass fraction of 40 to 50% of the total aircraft mass. Clearly centrifugal stiffening of high aspect ratio rotors-wings is a highly effective method of taking lifting surfaces to significantly greater aspect ratios, while achieving very low lifting surface weight.

While rotor blades use high tip speeds (600 to 850 ft/sec) to achieve high radial accelerations, centrifugal forces can also be achieved at relatively low

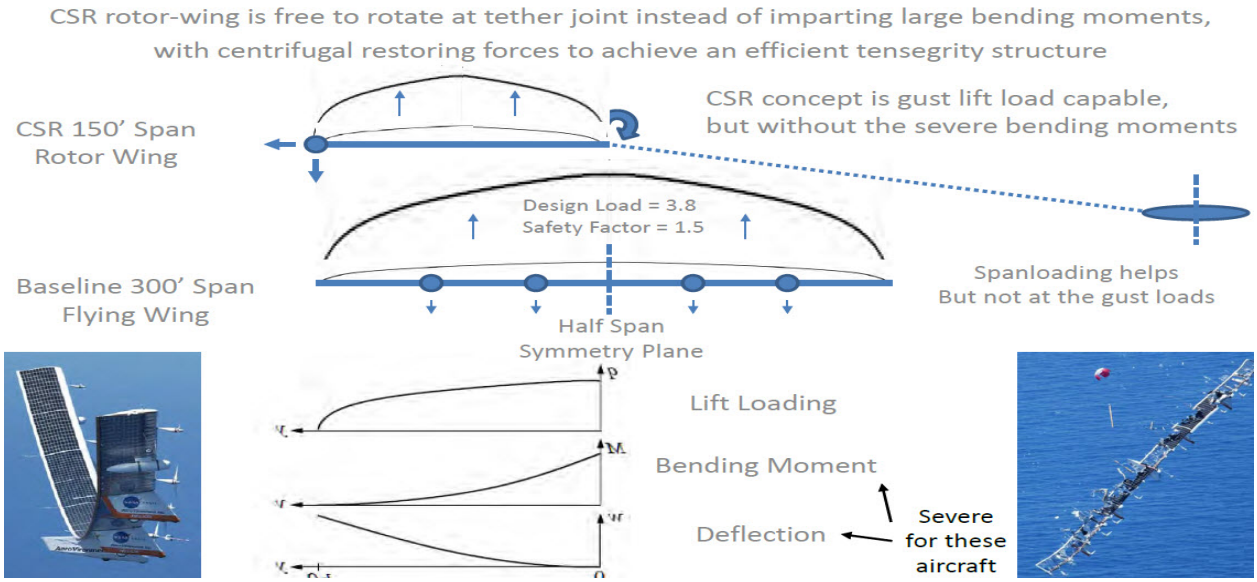

Figure 1.5: Lift load distribution on CSR concept versus conventional wing configuration.

tip speeds by having a large mass at the rotor outer most tip location. Slowed rotor concepts such as the CarterCopter use depleted uranium at the rotor tips to maintain rotor blade stiffness at low rotational speeds. The centrifugal force in rotor blades results in the wing spar material being very small to counteract the rotor lift root bending moment. Helicopter rotors experience 1000's of g's of acceleration, while the CSR rotor-wing needs only about 2 g's in combination with the large tip mass to provide sufficient stiffening for minimal bending.

The CSR provides a tensegrity structure approach to achieve high aspect ratios instead of HPA structures which depend on large wing chords to provide a thick structural spar depth. Spreadsheet and Matlab analysis methods were developed to provide a summation of forces and determination of tensile forces across the wing and tether. This method was first applied to existing HALE conventional wing structures to validate the ability of the method to capture accurate mass trends, and then applied to the CSR structure.

Figure 1.5 shows the lift load distribution on the CSR concept versus a conventional wing configuration showing the distribution of forces and the ability of the rotor-wing elements to pivot at the tether connection to alleviate a root bending moment. The NASA/AeroVironment Helios is shown as an example of HALE aircraft experiencing very high bending moments over large wing spans. The Helios failed during a test flight because the wing fluttered due to a lack of structural stiffness.

1.6.2 Achieving High Lift To Drag Ratios

An objective of the CSR design uses the high aspect ratio rotor-wing to achieve high L/D ratios. Helicopter rotors achieve poor lift efficiency because their lift is developed over the entire diameter. This results in a triangular load distribution with almost the entire lift generated by the outer 25% of the rotor blade. Achieving low induced drag depends on achieving an elliptic load distribution across the lifting surface. Helicopter rotors have high induced drag, because they do not achieve an elliptic loading.

Helicopter rotors also experience high induced drag because each rotor acts in close proximity to the downwash of the blade rotating in front of it, which increases the angle of attack required for lift generation. Instead, the CSR concept has each satellite operating in a downwash field independent of the other rotor-wings due to the large spatial separation. An effective way of visualizing the resulting reduction in downwash induced drag is to consider things

from a rotor disc loading perspective, as seen in Figure 1.6. The CSR concept achieves a downwash field in the shape of a toroid of the traversed rotational rotor-wings based on the extremely large tether diameters. A conventional rotor with 20 foot radius achieves a swept disc area of 1256 square feet, while the same 20 foot radius with an 80 foot tether traverses a swept area of 11,304 square feet. This is far greater than that of the span of the rotor-wing alone. The total rotor disc area relates directly to the induced drag.

In addition, a conventional helicopter rotor has a triangular lift distribution with poor aerodynamic efficiency. However, the tethered rotor-wing achieves an ideal elliptical load distribution because the entire satellite has a relatively constant velocity field. There is approximately 20% variation in airflow velocity, which can be made elliptic through a modest twist and taper distribution across the rotor-wing. The final method for minimizing induced drag uses the same Outboard Horizontal Stabilizer (OHS) layout used by the Boeing Vulture concept, which was originally developed by the WW II Blohm and Voss aircraft concept, and with application as recently as by Scaled Composites Spaceship One.

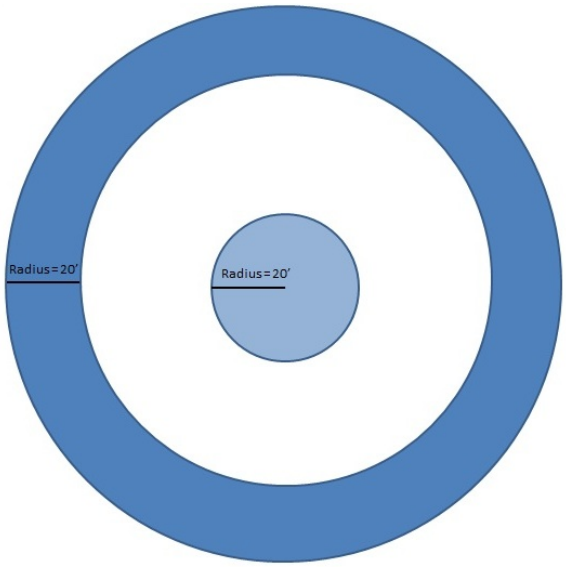

Figure 1.6: Simplified traversed rotor disc area.

1.6.3 Minimizing Parasitic Drag

While the resulting low induced drag of the CSR rotor-wing is critical, operation at the maximum L/D requires that equal portions of induced and parasite drag are achieved in balance. Therefore, it is also important to provide a mechanism for lower parasite (skin friction) drag. This is accomplished in two ways with the CSR concept, which are illustrated in Figure 1.7.

Conventional HALE concepts require that payload volumes move at the same speed as the rest of the vehicle. For bulky antenna or optic payloads this can result in substantial parasite drag. The payload for the CSR concept remains stationary at the hub, which is independent of the required lift generation. The size of the satellite is minimal due to the high density of the enclosed components (electric motor and batteries).

Another mechanism of achieving lower parasite drag comes from the rotor-wings having low thickness to chord (t/c) ratios, because of the low resulting bending moments of the centrifugally stiffened structure. The use of low t/c airfoils is important for HALE aircraft operating at low Reynolds number. This condition maintains laminar flow for much of the airfoil while insuring that laminar separation does not occur.

At first glance the tether drag may appear to significantly increase the parasite drag. The nondimensional cross-sectional Coefficient of Drag (CD) of a cylindrical cable is extremely high (around 1.15 compared to a typical airfoil of .01). As the tether diameter increases with larger scale vehicles, the CD of the tether improves through braided cross-sections. These have improved separation characteristics that achieve CD's of about 0.75.

The tether cable diameter is able to be small because it is extremely structurally efficient at carrying tensile loads. Combined with the fact that the average tether speed is only 40% of the rotor-wing tip speed, the resulting tether drag is only 5 to 10% of the total vehicle drag. Of course, these values depend on the amount of centrifugal tensile load that sizes the tether diameter and whether the tether is designed to conduct electricity for energy sharing across the payload hub and the rotor-wing elements.

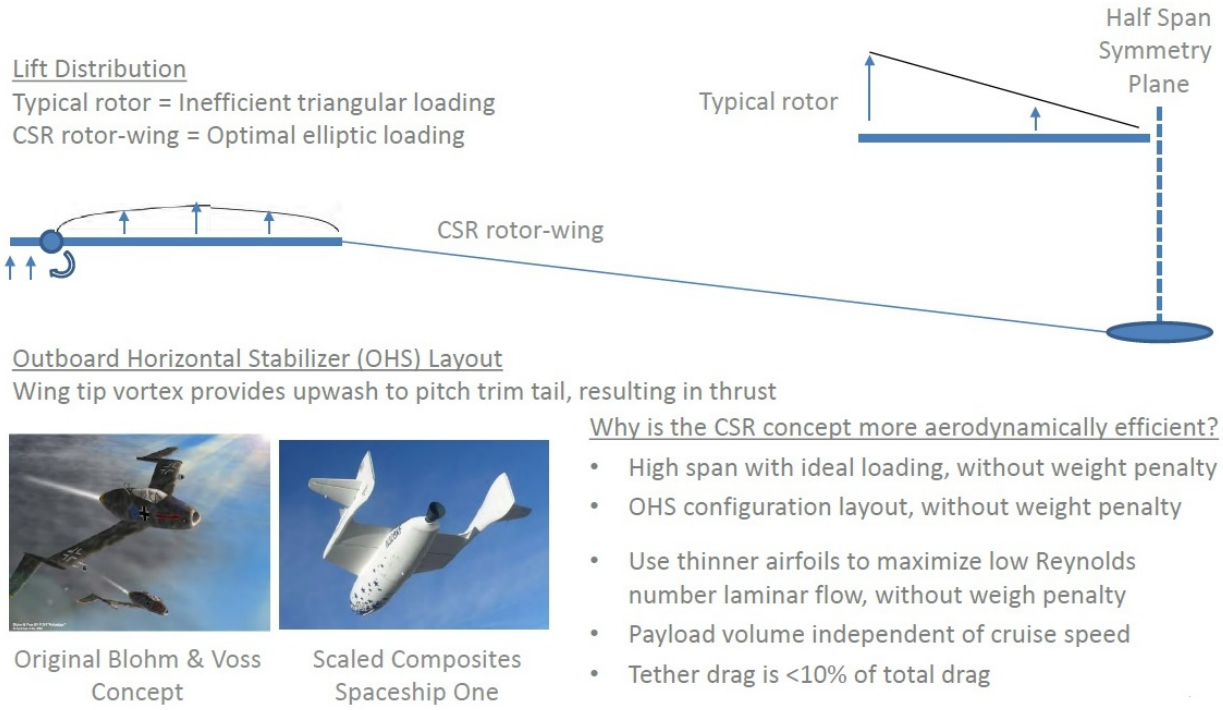

Figure 1.7: CSR aerodynamic loading versus conventional helicopter rotor.

A factor of safety of 6 was applied to the tether tensile load to insure reasonable tether cable diameter. Spectra offers a good match to CSR requirements due to low stretching of about 1%. Spreadsheet and Matlab methods were assembled for calculating the parasite and induced drag of the CSR concept using a blade element aerodynamic analysis.

1.6.4 CSR Comparisons

The prior mass, force balance, and drag methods were combined along with methods to determine the power required for maintaining flight. The results of these analyses are presented within Table 1.2 across several payload sizes ranging from sUAS to full satellite equivalent payloads. The vehicle characteristics shown are not optimized, but merely a result of simple sizing sensitivities to yield reasonable configurations. A useful tracking metric to compare the CSR concept results to other approaches is the power required per vehicle pound to maintain flight.

An interesting comparison reference to the CSR concept is the recent successful winner of the Sikorsky Human Powered Helicopter prize (the Aerovelo Atlas), which lifted a total mass of 281 lbf (121 lbf vehicle plus 160 lbf pilot) for 64 seconds with a human power output of almost 750 watts (2.67 watts/lbf). This was accomplished with a total rotor lift area of 13,700 ft, that had 4 rotors comprising a total of 156 ft diameter, and an incredibly lightweight and flimsy structure that provided no design to ultimate load or safety margins.

A total safety margin over the design load of 3 was utilized for sizing the CSR structure, with the resulting specific power required being somewhat higher across all vehicle sizes than that required by the Atlas. At a similar vehicle weight the CSR concept is able to achieve around 3.5 watts/lbf. As another comparison, the Zephyr 7 is calculated to use approximately 550 watts at cruise for the 110 lbf vehicle, yielding a power required per pound of 5 watts/lbf, which is 45% more power than required for a CSR concept at a similar mass.

	sUAS	Camera	Small AT-Sat	AT-Sat
Geometry				
Diameter - Outer (ft)	70	200	400	800
Diameter - Inner (ft)	56	160	320	640
Span (ft)	7	20	40	80
Chord (ft)	0.5	1.0	1.0	1.5
Aspect Ratio	18.7	26.7	53.3	71.1
Swept Lifting Surface (ft^2)	1385	11304	45216	180864
Forces				
Rotational Rate (rpm)	20	7	4	2.25
Rotor-wing Tip Speed - Outer (ft/sec)	73	73	84	94
Rotor-wing Tip Speed - Inner (ft/sec)	59	59	67	75
Reynolds Number (avg)	233023	466045	532623	898802
Centrifugal Acceleration (g's)	4.52	1.58	1.03	0.65
Rotor-wing Angle vs Horizon (deg)	-15	-12	-12	-18
Tether Tension (lbf)	62	122	256	823
Weights				
Gross Weight (lbf)	39.2	226.8	592.5	2187.7
Rotor-wing Weight/Element (lbf)	13.3	60.5	158.0	583.3
Payload Weight (lbf)	3.9	22.7	59.2	218.7
Swept Disk Loading (lbf/ft^2)	0.028	0.020	0.013	0.012
Drag and Power				
Induced Drag (lbf)	133	646	1363	4835
Parasite Drag (lbf)	18	101	303	1294
Tether Drag (lbf)	9	35	180	602
Power Required (watts)	159	783	1847	6734
Specific Power (watts/lbf)	4.07	3.45	3.12	3.08

Table 1.2: Comparison of CSR concepts across several payload weights.

1.6.5 Analysis Results

The results of this analysis indicate a 35% improvement in the L/D ratio, while at the same time achieving a reduction in structural mass by 50% may be possible. Further gains may be feasible after optimization is applied to the current non-optimum results. Reduction in power by 35% appears possible, which will dramatically increase HALE mission feasibility. The improvement in drag and weight are the critical concept performance ingredients for this mission concept to achieve feasibility.

Applying these improvements potentially enabled by the CSR concept provide a basis for achieving a day/night energy balance while using near-term rechargeable batteries with specific energy of 400 Whr/kg, and thin film solar cells with thin-film efficiency of 35%. Use the same tool methodology developed in NASA/TP-2007-214861, but re-evaluate that analysis at the aerodynamic and structural mass ratios indicated by the CSR concept. This result is visualized in Figure 1.8 where the CSR concept aerodynamic and structural factors are specified for the same Pareto sensitivity frontier analysis of the energy required compared to energy available for completing a day/night cycle during the worst winter day conditions, as a function of the specific energy of the energy storage system and the solar cell efficiency (analysis performed by Mark Guynn of NASA Langley Research Center).

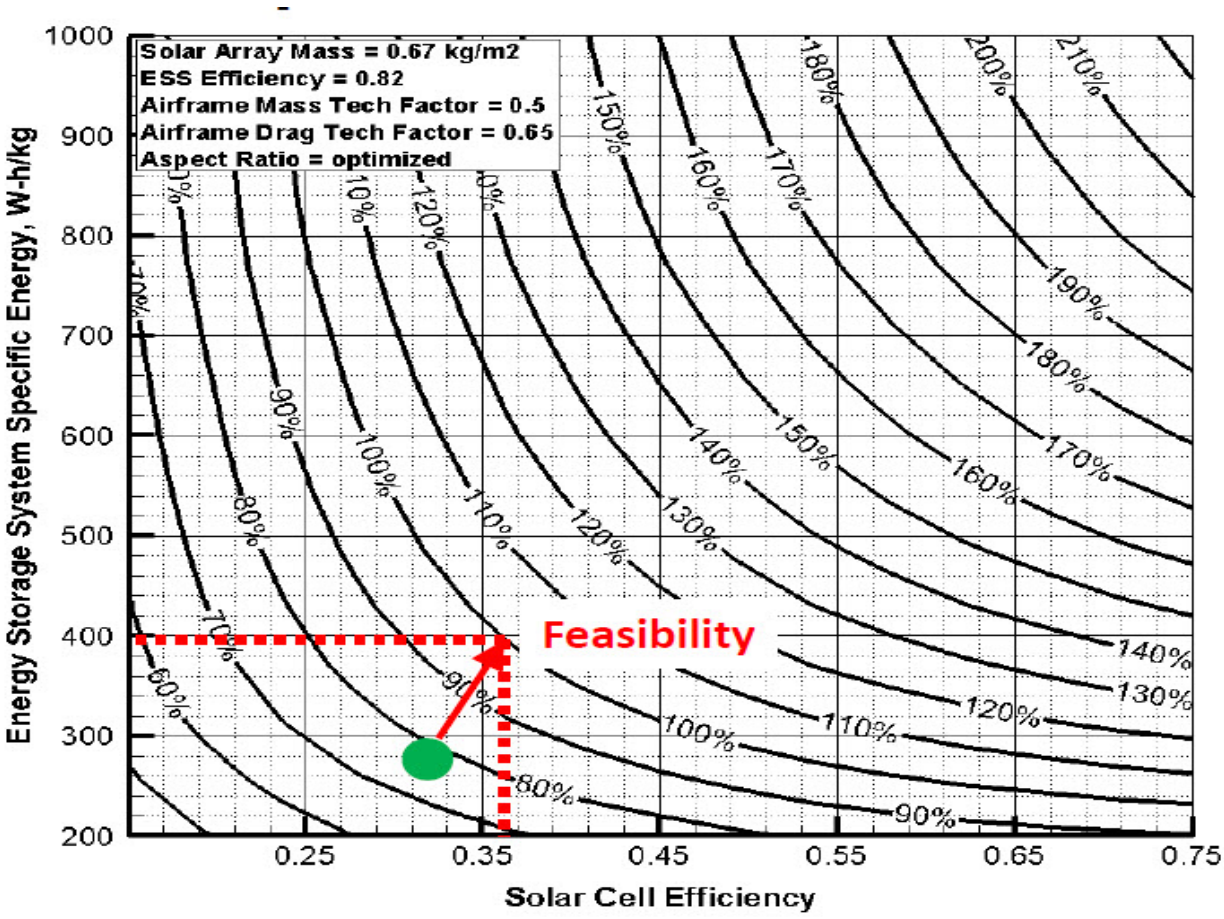

Figure 1.8: CSR concept specified for same Pareto sensitivity frontier.

1.6.6 Remaining Questions

The ability to achieve feasibility with near-term energy solutions provides a compelling reason to further investigate the assumptions buried within this initial analysis. Two assumptions not evaluated in this vehicle performance analysis are the ability to achieve a 10% mass fraction for the center hub structure (including the tether reel-in/out mechanical system), and the ability to maintain control with complex multibody dynamics present in a system that will experience nonuniform disturbances in real world operations.

The remainder of the Phase I investigation was directed towards answering the control feasibility, with detailed development of a multibody analysis method. While not within the scope of Phase I, the researchers were also highly motivated to test the resulting control algorithms while also verifying the assumptions present in the hub mechanics. A subscale test vehicle has been initiated for this purpose; however, it is still in development and will be completed prior to a Phase II proposal submission.

1.7 Unique New Missions

While the primary mission for the CSR concept would be for HALE communication platforms, a number of compelling missions have been identified that map directly into the unique capabilities of the CSR advanced concept. These unique advantages include achieving an extremely high L/D ratio, a stationary center hub, a large swept rotor-wing area, extremely low effective disc loading, and the ability to change the effective disc loading by reeling the tether in/out.

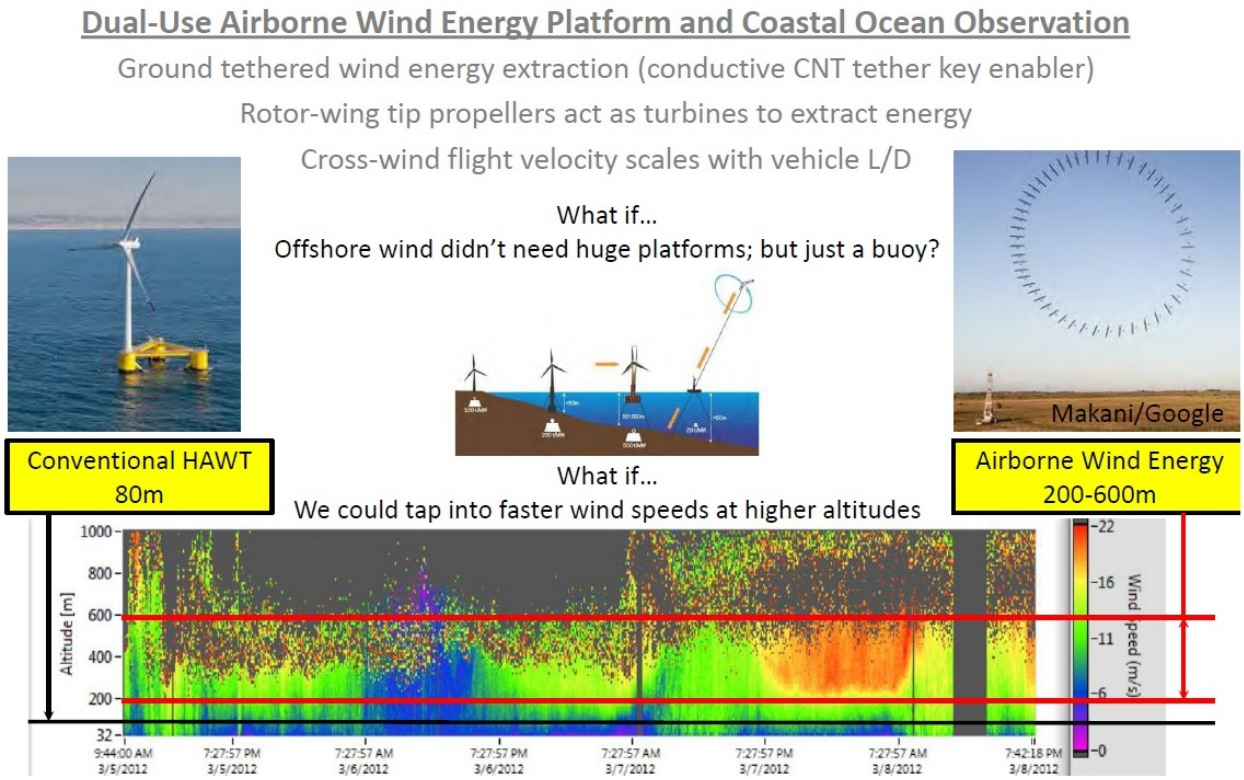

Figure 1.9: Airborne Wind Energy (AWE) and coastal ocean observatory platforms.

1.7.1 Airborne Wind Energy

A number of companies are currently investigating Airborne Wind Energy (AWE) production through aerial platforms. These systems harness the wind at altitudes where the winds are faster, the turbulence is lower, and the winds are more consistently available. Such systems require a tethered connection to the ground to harness wind energy, otherwise they would simply be blown downwind.

Companies such as Makani (purchased by Google this past year) are developing concepts as shown in Figure 1.9. Small aircraft are flown in circles, acting as the tip of a ground-based horizontal wind turbine, since the tips are performing >75% of the energy capture. The FAA ground obstruction rules enable such tethered platforms to be operated at altitudes as high as 2000 feet. With the Makani approach, the entire tether length is moving at the aircraft velocity, which is typically 200 to 300 ft/sec, resulting in high tether drag. Energy is extracted by propellers on the aircraft that act as turbines turning electric alternators, which then transmit the energy down the tether to the ground.

Because the tether connects the aircraft to the ground, the tether orientation to the aircraft is 90 degrees to each other so that the tether imparts a significant bending load on the wing. If the CSR concept were used in place of the conventional Makani aircraft concept, the ground tether would connect to the stationary CSR center hub and not experience a velocity or drag. The resulting drag of the system would be much less, and permit smaller land use as decreased tether angles to the horizon are accomplished. In addition, the CSR approach would maintain the ability to keep the rotating tether between the hub and rotor-wings along the span path to achieve a lighter weight solution.

Makani has already accomplished testing at the 10 to 50 kW scale in Hawaii, which has very high costs of electricity due to this coming from oil based energy production. In time, it may be proven that lower cost power can be achieved, but currently with

these smaller early adopter systems, the cost of energy is quite high, especially when land use costs are considered. If these AWE platforms were able to be positioned in locations where the platforms could act as multi-functional surveillance/communications as well as AWE energy harvesters, there would be the ability to lower the effective costs.

If a CSR platform was operated at 2000 feet, the communication transmission coverage diameter would be nearly 50 miles. The CSR platform could act as a cell phone tower or WiFi provider with a communication payload in the center hub. The visibility of the CSR platform would be far less than the alternatives of a tower or ground-based wind turbine.

The CSR concept achieves a higher Lift/Drag ratio compared to other airborne wind concepts, which results in higher tether angles and less land area under the vehicle radius of operation that depends on incoming wind direction. Off-shore application is particularly appealing since a CSR aerial vehicle would eliminate large and expensive mooring platform, which is required for ground-based wind turbines. Ground-based wind turbines experience huge bending moments in the tower structure and require massive concrete pads, while an AWE transmits no bending moment down the tether.

Off-shore also provides significant dual-use market opportunities. The first long-term civil use of a UAV was recently approved in Australia to fly along the coastline as a shark spotting platform. This was performed previously by small aircraft operating with two people on board, the potential cost savings are considerable. A series of off-shore CSR platforms could be performing a combination of energy harvesting, distressed swimmer surveillance and Wifi from each platform with very lightweight payloads.

While such applications may be considered niche markets, hundreds of thousands of lifeguards in the world monitor coastal waters. Potentially there are even larger markets for this mission concept as it is applied to distributed residential power production, with a sUAS sized version likely capable of providing 2 to 5 kW of power at altitudes of 500 feet with average wind speeds of less than 20 mph.

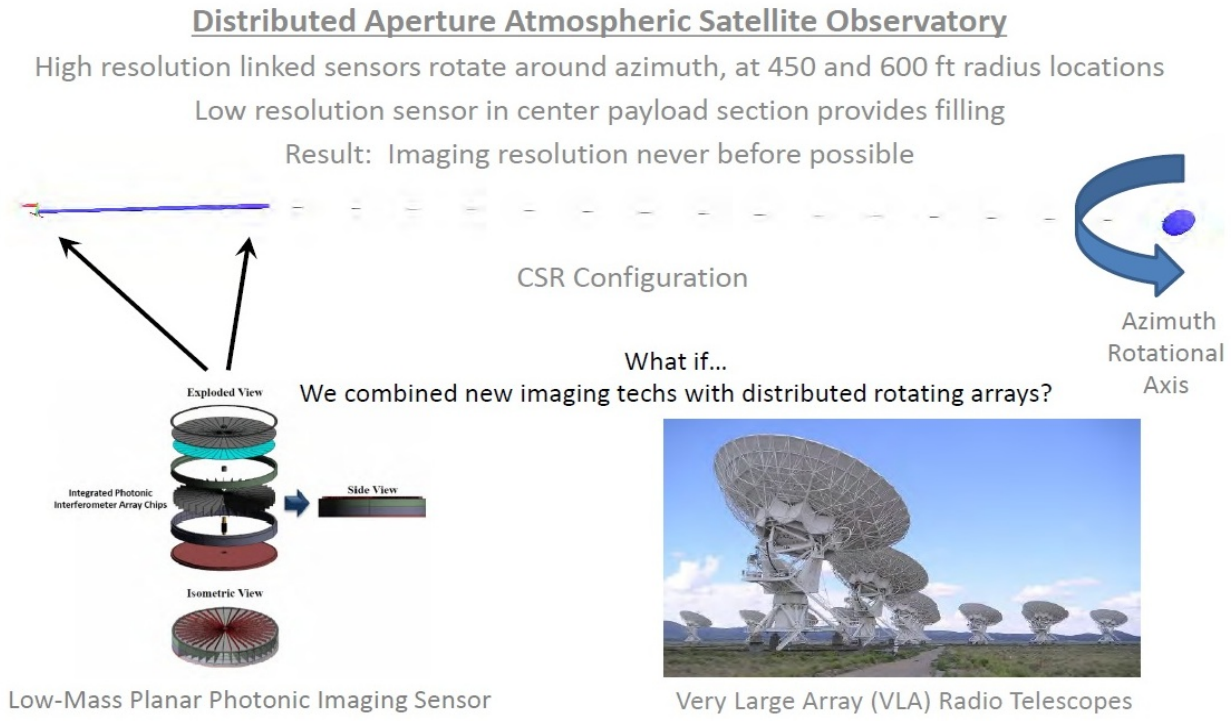

Figure 1.10: Distributed aperture atmospheric satellite observatory mission concept.

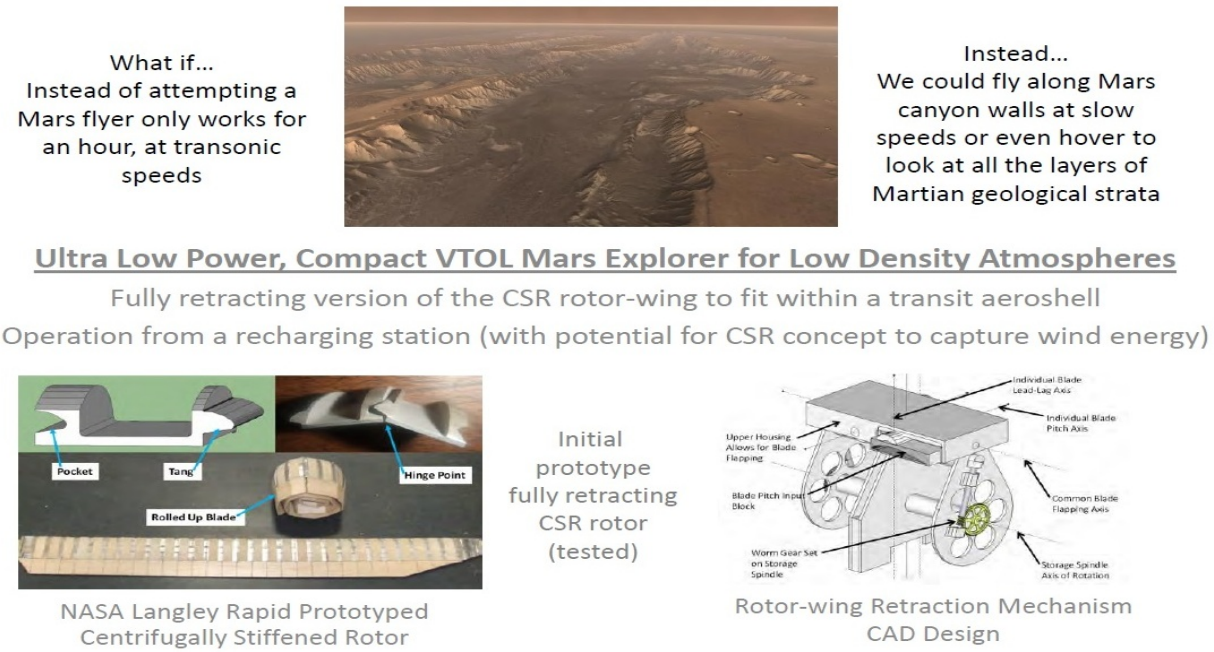

Figure 1.11: Ultra low power, compact VTOL Mars Explorer mission concept.

1.7.2 AT-Sat Observatory

The CSR concept provides a large rotating structure, as well as large volume at the center hub, with the capability of operation above the majority of the atmosphere. Integrating high resolution, compact, linked optic sensors (such as the Low Mass Planar Photonic Imaging Sensor currently being developed as Phase II NIAC research) at the tip and root of each rotor-wing will permit a rotating imaging array across a full 600 diameter azimuth. Combining this with a lower resolution conventional imaging system in the center hub for image filling could provide a resolution never before possible. Such an observatory could be designed as a dual-purpose system that provides imaging both upwards for space investigations, as well as for Earth imaging. A depiction of the device is shown in Figure 1.10.

1.7.3 Compact VTOL Vehicle

A version of the CSR concept has been identified that enables full retraction of the rotor-wing, shown in Figure 1.11 to achieve a highly compact VTOL vehicle that can operate at extremely low discloading (<0.03 lb/ft2) on atmospheres such as Mars that have atmospheric densities similar to Earth at 100,000 feet altitude. Because it was highly uncertain whether the centrifugal stiffening loads would be sufficient to maintain a rigid rotor-wing for this highly faceted spanwise design, a sub-scale version of the fully retracting rotor-wing was fabricated and tested with success. The rotor-wing experiences an increase in weight and complexity with a decrement in performance to achieve compact packaging, however was shown to be a feasible approach that could facilitate very low discloading renewable VTOL aerial vehicles which could be packaged effectively in an aeroshell.

1.7.4 Non-Commercial Applications

A large number of other missions exists for the CSR concept with most relating to HALE missions on Earth. A comprehensive list is provided in Figure 1.12. While clearly Facebook and Google will become major investors in this technology area due to the civil mission application potential, it is interesting to note how many Earth Science and Government Service mission are also of high importance to our societal needs. Because of this, it seems important that government research institutions such as NASA help to establish feasible HALE platforms, which can focus on non-commercial services.

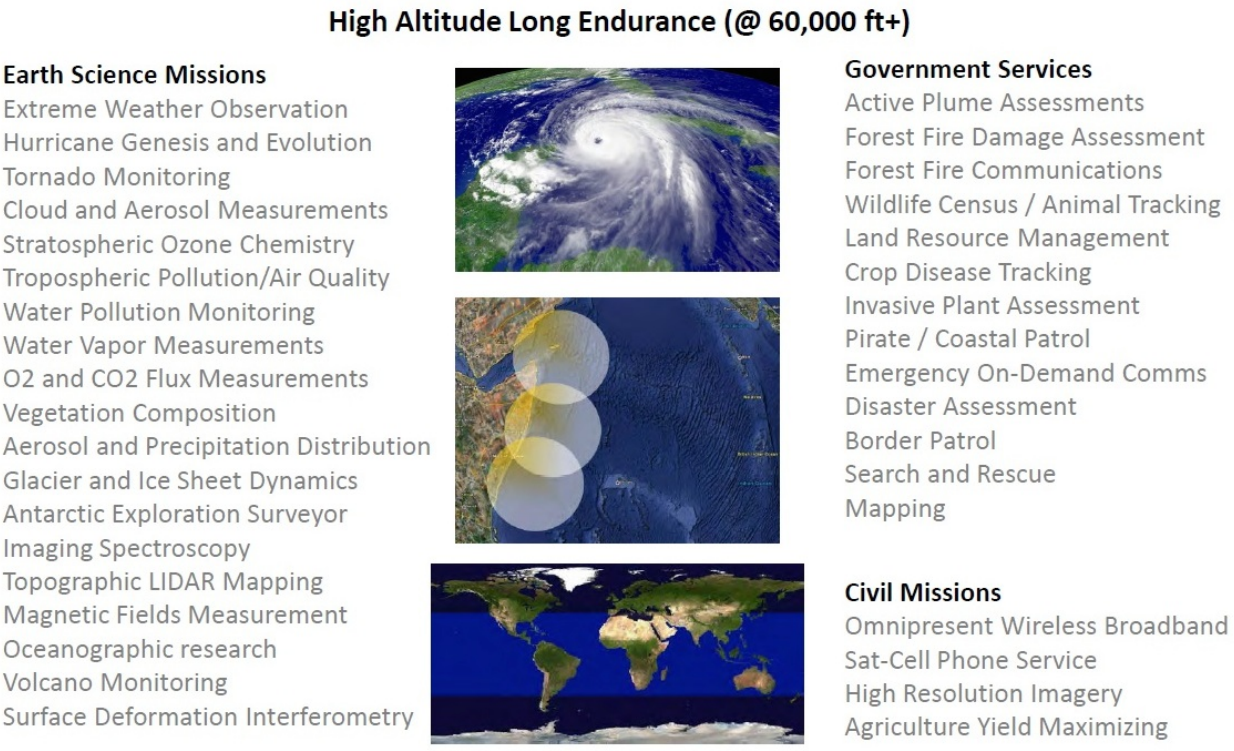

Figure 1.12: HALE missions that relate to CSR concept use.

Chapter 2

Plant Development

This chapter expands the preliminary analysis performed on the CSR vehicle, and develops the plant model required for the controls development. It presents how the system is modeled and derives the equations of motion of the vehicle. These dynamics are implemented in a multi-body dynamics structure which governs the CSR simulations. Finally, the nonlinear system is trimmed and linearized which is the starting point for the controller development.

Motivation

The CSR concept vehicle is a radical departure from conventional fixed-wing and rotor craft design methodology, but this concept offers greater flight capabilities by combining the best features of both fixed-wing and rotor craft designs. However, conventional aircraft dynamics are not applicable to this concept vehicle, so a complete mathematical model for the CSR dynamics needs to be established. Similarly, existing control techniques are not appropriate for this concept vehicle. The primary objective with this initial analysis is to demonstrate that a suitable control law exists and can be successfully implemented on this vehicle.

Proof of concept is demonstrated through scaled prototypes. Before developing the prototypes and full scale vehicle, simulation and analysis are required to gain a better insight into how the system behaves. Before starting the controls analysis the system needs to be linearized so that control theory can be applied, and prior to linearizing the model, a set of initial conditions must be identified which put the system in a steady-state equilibrium condition. Developing the equations of motion (EOM), finding trimmed control inputs, and obtaining a linearized model of the system is a crucial step towards beginning the controls analysis.

Objectives

The goal of this chapter is to develop a complete and accurate description of the CSR system. The design methodology for this vehicle follows an iterative process, so basic models and prototypes are used as starting points, and more refined models and prototypes are developed over time. The models must provide sufficient accuracy to evaluate the system, but also be modular enough to accept more sophisticated models throughout the development process. Different vehicle geometries at various scales are evaluated, so the models must be general enough to accommodate alternate configurations. Parameter files are used to store the vehicle geometry and physical attributes, so various designs can be evaluated by simply changing the parameter files.

The first objective defines the system, develops the equations of motion (EOM), and implements the simulation of the CSR system. The system is reduced to a collection individual subcomponents.

Each component has a description, some physical parameters, and a coordinate frame. As the vehicle moves through space, various forces and moments act on these components. These external forces and moments are calculated for each individual entity at their current state, and then summed together to provide the total force and moment acting on that rigid body. All the relationships between components are compiled into a multibody dynamics structure, which implements the numerical routine responsible for the nonlinear simulation.

The next goal of this chapter takes the developed CSR dynamics, and expresses those relationships in a form suitable for control analysis. Before applying controls, the system must operate in a steady-state equilibrium point, such as hover. Trimming is the process of finding states and control inputs which attain a particular equilibrium point. The trimming routine takes an educated guess value for the system initial conditions, and then optimizes a force balance equality for the lift generated by the system. Once the vehicle is trimmed, a linearization routine takes the nonlinear equations of motion and determines the state space matrices used for control analysis.

Outline

Before undertaking any of the controls development for the CSR system, a complete and accurate description of the vehicle is required. This chapter develops all aspects of the physical plant used during the design and analysis process.

Section 2.1 addresses *Modeling*, which illustrates the main features of the CSR vehicle, then decomposes the system into individual components for the hub, tether, and satellite. It describes the physical properties of all the components, and assigns coordinate frames used during the modeling process.

Section 2.2 derives the *Dynamics* of the CSR system. These are the mathematical relationships that describe the equations of motion of the vehicle. It identifies all the pertinent forces and moments acting on each component, and uses first principles to obtain those force and moment values. Finally, it presents a parallel CFD analysis which models the aerodynamics of the satellite body.

Section 2.3 implements the *Simulation* that models the vehicle within the Matlab environment. It formulates a multibody dynamics structure based on a numerical routine, presents a generalized approach to implement the routine, and applies the theory to the CSR models.

Section 2.4 address *Trimming* the vehicle. This process seeks to obtain the set of states and control inputs that achieve hover. While the CSR is in hover, the system is in a steady-state static equilibrium condition, which is the starting point for linearization and controls development.

Section 2.5 performs *Linearization* on the system. It takes the nonlinear system dynamics and yields linear relationships around the hover condition. The values of the partial derivatives populate the state space matrices used for controls analysis.

2.1 Modeling

Modeling the CSR system is the first step towards deriving the system dynamics, building the simulations, and developing the control analysis. This section presents the overall vehicle structure, describes the individual components, introduces coordinate frames, and illustrates the forces present on each component.

Figure 2.1: Complete Centrifugally Stiffened Rotor (CSR) system.

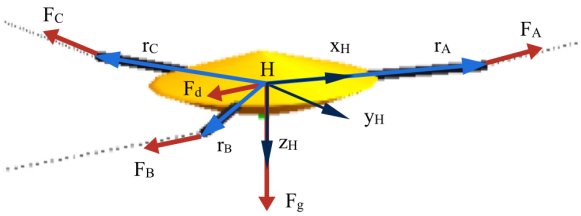

Figure 2.2: Hub model.

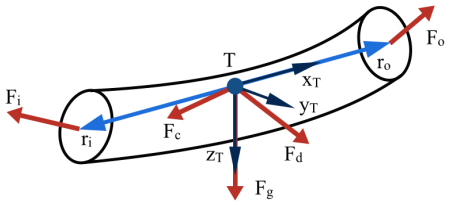

Figure 2.3: Tether model.

2.1.1 System Overview

Three tethered satellite vehicles rotate around a central hub, illustrated in Figure 2.1. Each satellite has a propeller mounted on a fuselage, a horizontal stabilizer with an elevator, a vertical stabilizer with a rudder, and a wing section. Centrifugal forces keep the tethers taught and lifting forces from the wings support each satellite and the central hub. Individual satellites are controlled through their propeller, elevator, and rudder, and the central hub is controlled by manipulating tether forces coming from the three satellite vehicles. The axes for the inertial frame $\{N\}$ are designated as:
`+X: North; +Y: East; +Z: Down.`

2.1.2 Hub Description

The central hub rigid body anchors the three tether systems, illustrated in Figure 2.2. It has mass m_H and moment inertia $J_H = \texttt{diag}\{\, J_{Hx}\, J_{Hy}\, J_{Hz}\,\}$ expressed in the hub frame $\{H\}$. The three tethers are arbitrarily labeled as `A`, `B`, and `C`, to distinguish them from each other. Position vectors (r_A, r_B, r_C) relate the tether anchor points to the CG of the hub. Forces that act on the hub include gravity, tension from the tethers, and aerodynamic forces as the hub moves through space. The frame associated with the hub is located at the CG of the rigid body, with
`+X: Tether A; +Y: Right; +Z: Down.`

2.1.3 Tether Description

Each tether is modeled as a chain of rigid body elements connected together with spherical joints, depicted in Figure 2.3. Each element has a cylindrical shape with mass m_T and moment inertia $J_T = \texttt{diag}\{\, J_{Tx}\, J_{Ty}\, J_{Tz}\,\}$ expressed in the tether frame $\{T\}$. Two position vectors, r_i and r_o, point from the CG of the element to the inboard and outboard endpoints, respectively. Each tether element has four forces acting on it. Two forces, F_i and F_o, come from the joint constraints and are located on each end point of the rigid body. Gravity and aerodynamic drag make up the other two forces, F_g and F_d. The frame of each tether element is located at the CG of the rigid body, with
`+X: Outward; +Y: Right; +Z: Down.`

2.1.4 Satellite Description

The satellites are attached to the tethers, and are the rigid bodies which contain all the control inputs to manipulate the CSR system. A satellite layout is provided in Figure 2.4. Each vehicle moves through the inertial frame as a rigid body, with mass m_S and moment inertia $J_S = \texttt{diag}\{\, J_{Sx}\, J_{Sy}\, J_{Sz}\,\}$ expressed in the satellite frame $\{S\}$. External forces and moments that act on the vehicle come from gravity, the propulsion system, and aerodynamic effects. The aerodynamic forces and moments are generated from the wing section, horizontal stabilizer, vertical stabilizer, elevator, and rudder. The frame origin of the satellite is located at the CG of the vehicle, and its coordinate frame is oriented as
`+X: Nose; +Y: Right; +Z: Down.`

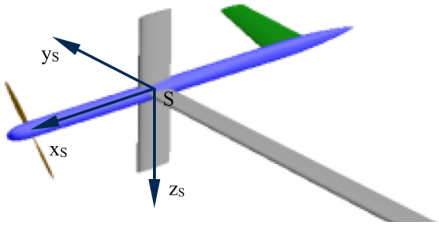

Figure 2.4: Satellite model.

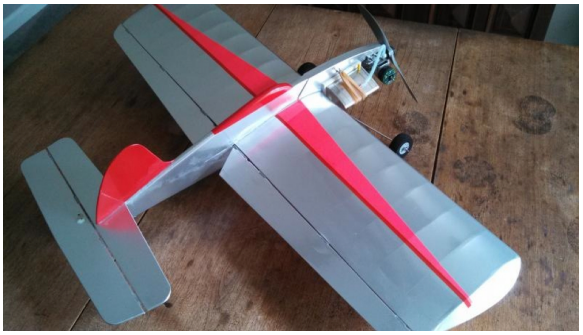

Figure 2.5: COTS Prototype satellite vehicle.

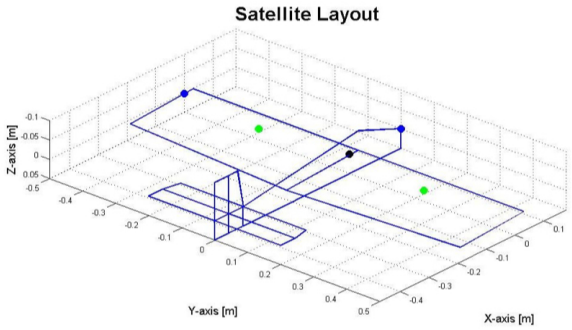

Figure 2.6: Matlab satellite vehicle.

2.1.5 COTS Prototype Vehicle

The first prototype in the spiral development life cycle is a commercial off the shelf (COTS) control line aircraft from Brodak, shown in Figure 2.5. This vehicle was selected as the first prototype platform because it is small, light, inexpensive (< $100), and designed to fly out of the box. The simplicity of this prototype facilitates bench testing to configure new avionics hardware, test system identification techniques, and implement new control laws; all while reducing the risk of a crash from a custom prototype with unknown dynamics. The vehicle weighs 2.5 lbf (11.12 N), has a 38 in (0.97 m) wingspan, with a 24 in (0.61 m) fuselage length.

2.1.6 Matlab Satellite Model

The control line aircraft was modeled in Matlab to store vehicle geometries for simulation purposes. The Matlab satellite model is depicted in Figure 2.6. All the geometries are stored in a parameter file, and the satellite characteristics are calculated from those input dimensions. The satellite structure was assembled with modularity in mind, so parameter files can be changed to reflect different satellite layouts (different prototype versions, and various sized full scale systems). The lifting force is located at quarter chord of the wing, and at the geometric center of all control surfaces. The motor vector includes tilt in pitch and yaw directions, if needed.

2.1.7 Scaled Prototype Satellite

The COTS control line aircraft tests new components and control algorithms. After successful initial demonstrations, testing advances to a scaled prototype. This vehicle more closely resembles the full scale system, and collects data to determine the aerodynamic characteristics of the CSR vehicle. The following sections describe the geometry of the scaled and full sized satellites, and provides dimensions of the prototype vehicle.

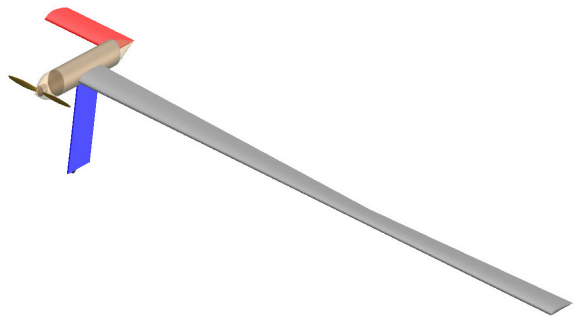

Figure 2.7: Isometric view of the prototype satellite.

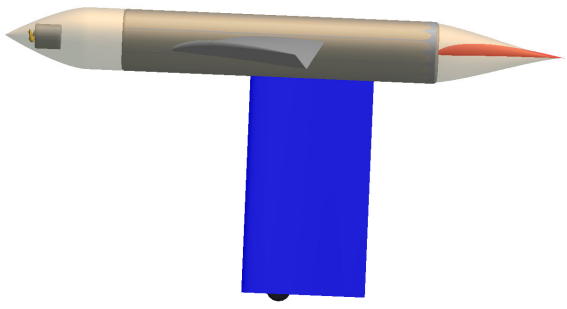

Figure 2.8: Side view of the prototype satellite.

Component	Length/ Span (ft)	Diameter/ Chord (ft)	Shape/ Airfoil
Fuselage	5.5	0.1667	Circular
Wing	7.0	0.5	GOE596
Horz Tail	1.0	0.5	GEO596
Vert Tail	1.0	0.5	GEO596

Table 2.1: Prototype parameters.

Description

The satellite has an asymmetric mono-wing design, inboard wing section, cylindrical fuselage, outboard horizontal stabilizer, and vertical stabilizer below the vehicle. The prototype layout is modeled in Vehicle Sketch Pad (VSP), where Figure 2.7 shows the isometric view of the satellite, and Figure 2.8 illustrates the side profile viewed from inboard to outboard. The figures depict the inboard wing in grey, the vertical stabilizer in blue, the outboard horizontal stabilizer in red, and the fuselage in tan. Dimensions of the prototype satellite are provided in Table 2.1.

Wing Surface

The prototype and full scale systems implement a unique twist distribution on the wing. Because the system is in a constant state of rotation, there is a nonuniform freestream velocity over the wing. The tapered twit geometry was designed to provide an optimized elliptical lift distribution over the lifting surface. The wing has a 7.0 ft (2.13 m) wing span, a constant chord length of 0.5 ft (0.15 m), and is located 0.8 ft (0.24 m) from the nose of the fuselage. Both the root and wingtip have zero incidence angle with a 6.5° linear washout that meet 3 ft (0.91 m) from the inboard wingtip. The wing uses a GOE596 airfoil profile, displayed in Figure 2.9.

Control Surfaces

There is no twist or taper on the horizontal or vertical tail surfaces. The horizontal stabilizer is positioned outboard of the fuselage. This location takes advantage of the wing tip vortices, which generates additional lift across the horizontal surface. The leading edge is located 1.75 ft (0.53 m) behind the nose of the fuselage, and 100% of the control surface is dedicated to pitch control. The vertical control surface extends below the fuselage. Camber is designed into this airfoil, so even with a zero angle of attack the surface generates lift in the outboard direction. The vertical stabilizer houses the landing gear, its leading edge is located 1.0 ft (0.30 m) from the nose of the fuselage, and 25% of the surface is used for yaw control.

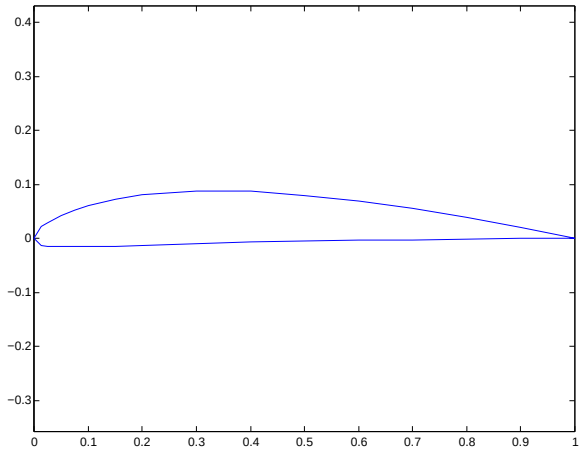

Figure 2.9: GOE596 airfoil profile.

2.2 Dynamics

Modeling defined the individual components that make up the CSR system, outlined relationships between those components, and identified the forces acting on them. This section describes the dynamics of the system, which outlines the mathematical relationships for all the forces and moments acting on each individual component. This establishes the equations of motion that are used for both simulation and controls analysis.

2.2.1 Overview

The following sections outline the various forces and moments that act on each individual component of the CSR system. Then, the total force and moment on the rigid body element is the summation of all the forces and moments acting on that body. Displacement vectors define the locations where forces act on the rigid body, typically located at the CG,

or at the geometric center of a control surface. The forces and displacement vectors determine the moments with the relationship

$$M = d \times F \tag{2.1}$$

where the cross product of the displacement vector d and the force vector F yield the resultant moment M for that subcomponent.

2.2.2 Common Forces

Many forces are common to all the CSR components. Such forces include gravity, centrifugal force, and aerodynamic lift/drag forces. Gravity is always downward (positive z in the inertial frame), and is expressed by

$$F_g = m\, g\, [\, 0\; 0\; 1\,]^T \tag{2.2}$$

where F_g is the force of gravity, m is the mass of the element, and $g = 9.81 m/s^2$ is the acceleration due to gravity. Nearly all CSR components are in a state of rotation which are subject to a centrifugal force. This force is expressed as

$$F_c = m\,(\omega \times (\omega \times r)) \tag{2.3}$$

where the centrifugal force vector F_c is determined by the mass m, angular rate vector ω, and position vector r, of the element. Similarly, all rigid bodies experience aerodynamic drag, and many provide aerodynamic lift. Lift and drag forces are governed by the relationships

$$F_* = (1/2)\rho v^2 A c_*, \quad * = l, d \tag{2.4}$$

where the lift F_l and drag F_d forces are dictated by the density of air ρ, velocity v, cross sectional area A, and the lift c_l and drag c_d coefficients.

2.2.3 Hub Forces

Primary forces acting on the hub include: gravity, tension from the tethers, and aerodynamic drag. Gravity was previously described, and tether tension is accounted for within the simulation. Aerodynamic drag is a direct extension of (2.4), modeled as

$$F_H = [\, F_{Hx}\; F_{Hy}\; F_{Hz}\,]^T, \;\; F_{H*} = c_{Hf*} v_{H*}^2 \tag{2.5}$$

for $* = x, y, z$, which describes a linear relationship between hub drag force F_{H*} and the square of the hub velocity v_{H*}. A similar relationship exists between hub drag moments M_{H*} and the square of the hub angular rates ω_{H*}, described by

$$M_H = [\, M_{Hx}\; M_{Hy}\; M_{Hz}\,]^T, \;\; M_{H*} = c_{Hm*} \omega_{H*}^2 \tag{2.6}$$

for $* = x, y, z$. The coefficients, c_{Hf*} and c_{Hm*}, map the aerodynamic drag relationships for the hub. Initial values for the coefficients are obtained by estimating terminal velocity and maximum torque on the hub. Aerodynamic drag force and moment are expressed in the hub frame and act at the hub CG.

2.2.4 Tether Forces

Each tether element feels five forces acting on it. Two forces, F_{Ti} and F_{To}, come from the inner and outer joint constraints, and are accounted for in the simulation structure. The force of gravity F_{Tg}, and the centrifugal force F_{Tc}, have been previously described. The final force is aerodynamic drag F_{Td}, which is modeled with (2.4). The tether moves through the inertial frame with velocity v_T. Accounting for wind acting on the tether section, yields the relative airflow in the tether frame. The airflow vector component acts at the CG of the tether, and the component perpendicular to the tether gives the velocity v used in

$$F_{Td} = (1/2)\rho v^2 A c_{Td} \tag{2.7}$$

where $c_{Td} = 0.47$ is the drag coefficient around a cylindrical body.

2.2.5 Satellite Forces

The satellites contain all the available control inputs, so controlling the CSR is accomplished entirely through these entities. Each satellite applies its own control locally, and then all the satellites are used collectively to control the complete CSR system. Therefore, an accurate assessment of the satellite behavior is needed for both vehicle simulations and controller design.

Each satellite is modeled as subcomponents, which include: propeller, fuselage, wing, horizontal stabilizer with elevator, and vertical stabilizer with

a rudder. Each component has a designated frame and a position vector pointing from the frame origin to the CG of the satellite. Rotating between frames is done with an Euler rotation matrix R given as

$$R=\begin{bmatrix} c_\theta c_\psi & -c_\phi s_\psi + s_\phi s_\theta c_\psi & s_\phi s_\psi + c_\phi s_\theta c_\psi \\ c_\theta s_\psi & c_\phi c_\psi + s_\phi s_\theta s_\psi & -s_\phi c_\psi + c_\phi s_\theta s_\psi \\ -s_\theta & s_\phi c_\theta & c_\phi c_\theta \end{bmatrix} \quad (2.8)$$

where the attitude (roll, pitch, and yaw) is given by (ϕ, θ, ψ), and s_* and c_* are sine and cosine functions.

The force of gravity and the centrifugal force have already been presented, so the following sections describe the remaining forces acting on the satellite. These include the propulsion from the propeller, skin friction drag from the fuselage, and the lift and drag profiles and how they are applied to the aerodynamic surfaces. Any forces that do not act through the CG of the satellite will have a moment described by (2.1), and the total force and moment on the satellite is the summation of all individual forces and moments.

Propulsion Model

The motor spins at angular rate Ω_P, and generates forces and moments described by

$$F_P = [F_{Px}\ F_{Py}\ F_{Pz}]^T_;\quad M_P = [M_{Px}\ M_{Py}\ M_{Pz}]^T_. \quad (2.9)$$

The inner workings of a brushless DC motor, and the aerodynamic intricacies of a fixed pitch propeller may be handled in future developments. For the initial analysis, a simplified propulsion model is utilized as a first approximation for the propulsion dynamics. Blade flapping and side airflow are neglected, so the force and moment of the propeller only act parallel to the z-axis of rotation; therefore, (2.9) reduces to

$$F_P = [\ 0\ 0\ F_{Pz}]^T_;\quad M_P = [\ 0\ 0\ M_{Pz}]^T_. \quad (2.10)$$

The simplified model contains a linear relationship between the squared rotor angular rate Ω_P and the force and moment (F_{Pz}, M_{Pz}) delivered from the propulsion system. This relationship is expressed as

$$F_{Pz} = c_{Pf}\Omega_P^2,\quad M_{Pz} = c_{Pm}\Omega_P^2, \quad (2.11)$$

where c_{Pf} and c_{Pm} are the propeller coefficients. Future prototypes may include a canted motor, so

$$F_M = R(\ 0, \theta_M, \psi_M\ )F_P \quad (2.12)$$

maps the force from the propeller frame to the motor frame. Similarly, the moment in the motor frame is described by

$$M_M = d_M \times F_M + R(\ 0, \theta_M, \psi_M\ )M_P \quad (2.13)$$

where d_M is the position vector from the CG of the satellite to the motor frame.

Skin Friction

As the satellite moves through space, the fuselage is subjected to skin friction; a type of drag force from the airflow grabbing the fuselage surface. The skin friction drag coefficient is defined as

$$c_{Fd} = \frac{\tau_w}{\frac{1}{2}\rho U_\infty^2} \quad (2.14)$$

where τ_w is the wall shear stress, ρ is the density of air, and U_∞ is the free stream velocity. Treating $U_\infty = v$ yields

$$\begin{aligned} F_{Fd} &= (1/2)\rho v^2 A c_{Fd} \\ &= (1/2)\rho v^2 A \left(\tfrac{\tau_w}{\frac{1}{2}\rho v^2}\right) \\ &= A\tau_w \end{aligned} \quad (2.15)$$

where τ_w is defined as

$$\tau_w = \mu \left.\frac{\partial v}{\partial y}\right|_{y=0} \quad (2.16)$$

and where μ is the dynamic viscosity air, v is the fluid velocity along the boundary, and y is the distance above the boundary layer.

Lift and Drag Profiles

Several prototypes are planned as part of the spiral development design process, and different wing geometries will be evaluated during these design iterations. To easily accommodate these revisions in the simulation, a Matlab function models the lift and drag profiles for each of the control surfaces. The simulation stores lift/drag attributes including: zero angle c_l and c_d, linear range and slope, and max/min c_L values. Then the program uses these parameters, to assemble the lift and drag coefficients as functions

of the relative angle of attack of the surface. The lift and drag functions are depicted in Figure 2.10.

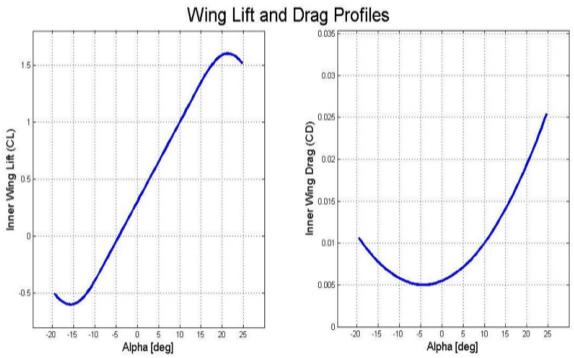

Figure 2.10: Lift and drag profile curves.

Aerodynamic Surfaces

The five surfaces on the satellite include the wing, horizontal stabilizer with an elevator, and vertical stabilizer with a rudder. Each surface has its own lift and drag profile to accurately represent each component. The satellite moves through the inertial frame with a known velocity. Accounting for wind within the simulation, yields an airspeed expressed in the inertial frame. The attitude of the satellite forms a rotation matrix that converts the airspeed vector to the local satellite frame. For each surface, the the airspeed vector is projected onto a plane parallel with the cross section of the surface. This projection yields the relative angle of attack and the magnitude of the airflow over the surface. The relative angle of attack is fed into the lift and drag profile function, which returns the lift and drag coefficients (c_L, c_D) for that particular angle and surface. The magnitude of the airspeed v, together with c_L or c_D, are passed into (2.4) which yields the magnitudes of the lift force and drag force. These magnitudes are converted into vectors where the drag force acts parallel to the airflow, and the lift force acts perpendicular to the airflow. The force vectors act at the quarter chord of the wing surface, and at the geometric center for all other surfaces. Each surface has a position vector pointing from the CG of the satellite to the point where the aerodynamic force acts. Then individual moments are calculated with (2.1).

2.2.6 CFD Aerodynamic Model

Satellite aerodynamics account for the largest contribution towards the CSR equations of motion, so a high fidelity aerodynamic model is desired to accurately simulate the vehicle dynamics. The first approach for modeling the satellite relied on first principles that govern rigid bodies and lifting surfaces. A parallel effort models the satellite vehicle using computational fluid dynamic (CFD) techniques. The following sections describe the software, how the satellite is modeled, the operation point, and the look-up table used within the Matlab simulation.

Athena Vortex Lattice

Satellite aerodynamics are obtained with Athena Vortex Lattice (AVL) software. The AVL program performs aerodynamic analysis on rigid aircraft with arbitrary configurations. It employs an extended lattice vortex model for the lifting surfaces and a slender body model for the fuselage. The software starts with the nonlinear system and generates a full linearization around any flight condition. The satellite is parsed into surfaces and fuselage components, which are input into the AVL program. Surfaces are modeled as a series of attached sections, where each section is described by a chord, leading edge location, airfoil, and pitch angle. Control surfaces have additional parameters which include a gain, hinge location, hinge vector, and sign of deflection. Coordinates of the top and bottom edges define the shape of the fuselage. Finally, all the user-defined sections are joined together through a linear interpolation process which generates the complete vehicle model. Figure 2.11 shows the AVL representation of the CSR satellite.

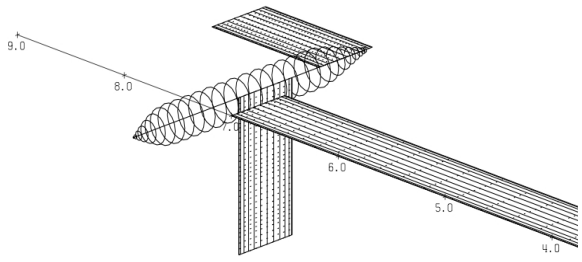

Figure 2.11: AVL representation of CSR satellite.

Modeling Elliptical Lift Distribution

The most important goal of any modeling effort is to generate a model that accurately represents the physical system in the real world. The CSR satellite is designed to have an elliptical lift distribution across the wing surface. This aerodynamic effect is an important contributing factor for eternal flight, and should be reflected in the aerodynamic models. Because the satellite rotates around the central hub, outboard wing sections have faster velocity profiles than inboard sections. The tapered wing is designed to account for this differential velocity while attaining the desired elliptical loading. Unfortunately, AVL does not permit differential velocities within the program. To work around this issue, the twist in the main wing was removed. This adjusted model in a uniform flow field, has a similar elliptical lift distribution as the CSR satellite operating in a state of rotation.

Operating Conditions

Differing scales of the CSR vehicle will have different operating points, which are dependent on the vehicle rotational velocity and the distance between the satellite and the hub. Similarly, each system will have two different operating points for hover and for takeoffs/landings. During start up, the tether is retracted so the satellite must spin more quickly to generate sufficient lift. With a retracted diameter of 22 ft (6.71 m), the vehicle must rotate at 74 rpm (7.75 rad/sec) for takeoffs and landings. Once the vehicle is airborne, the tethers are let out and the satellites generate the necessary lift at lower rotational velocities. When the tether is extended to 100 ft (30.48 m), the hub must spin at 11 rpm (1.15 rad/sec) to maintain the satellite cruise speed. During hover, the linear differential velocity across satellite wing, from inboard to outboard, is 29 mph (12.96 m/s) to 34 mph (15.20 m/s), respectively.

Look-up Table

When the AVL software is run, a unique operating point must be selected, then the software produces a linearized model around that point. However, linearization is only accurate for a small region around the point. To increase the fidelity of the model, a lookup table is populated with trends obtained by running the software at a variety of operating points. These operating conditions span the entire range of the flight envelope and actuator limits, which provide a complete dynamic picture of the satellite. Five parameters are adjusted

- angle of attack,
- side-slip angle,
- velocity magnitude,
- rudder deflection, and
- elevator deflection

and forces and moments are stored for each operating point. Then, a 5D linear interpolation process approximates the forces and moments between points. The AVL program is automated to generate the aerodynamic lookup table, where the boundaries of the variables are shown in Table 2.2.

Variable	Min	Max	Points
AoA (α) [deg]	-12	12	7
Side-slip (β) [deg]	-12	12	7
Rudder (δ_R) [deg]	-25	25	7
Elevator (δ_E) [deg]	-25	25	7
Velocity [m/s]	30	15	8

Table 2.2: Aerodynamic boundaries.

Trends

This section presents a series of figures that showcase the AVL generated results. For all plots, angles are in degrees, forces are in Newtons, and moments are in Newton-meters. Lift and drag are primarily a function of angle of attack α and vehicle airspeed V, so the first four plots demonstrate these relationships in Figure 2.12. The next six plots present the change in force and moment with respect to a change in a single independent variable. The nominal airspeed is 22.5 m/s, and the angle of attack, side-slip angle, rudder deflection, and elevator deflection are all set to zero degrees. Each of the five subplots changes a single variable, while all other variables are held at their nominal values. Figures 2.13, 2.14, and 2.15 showcase the forces, and Figures 2.16, 2.17 and 2.18 present the moments. All the plots demonstrate well-behaved trends which are smooth functions with no discontinuities.

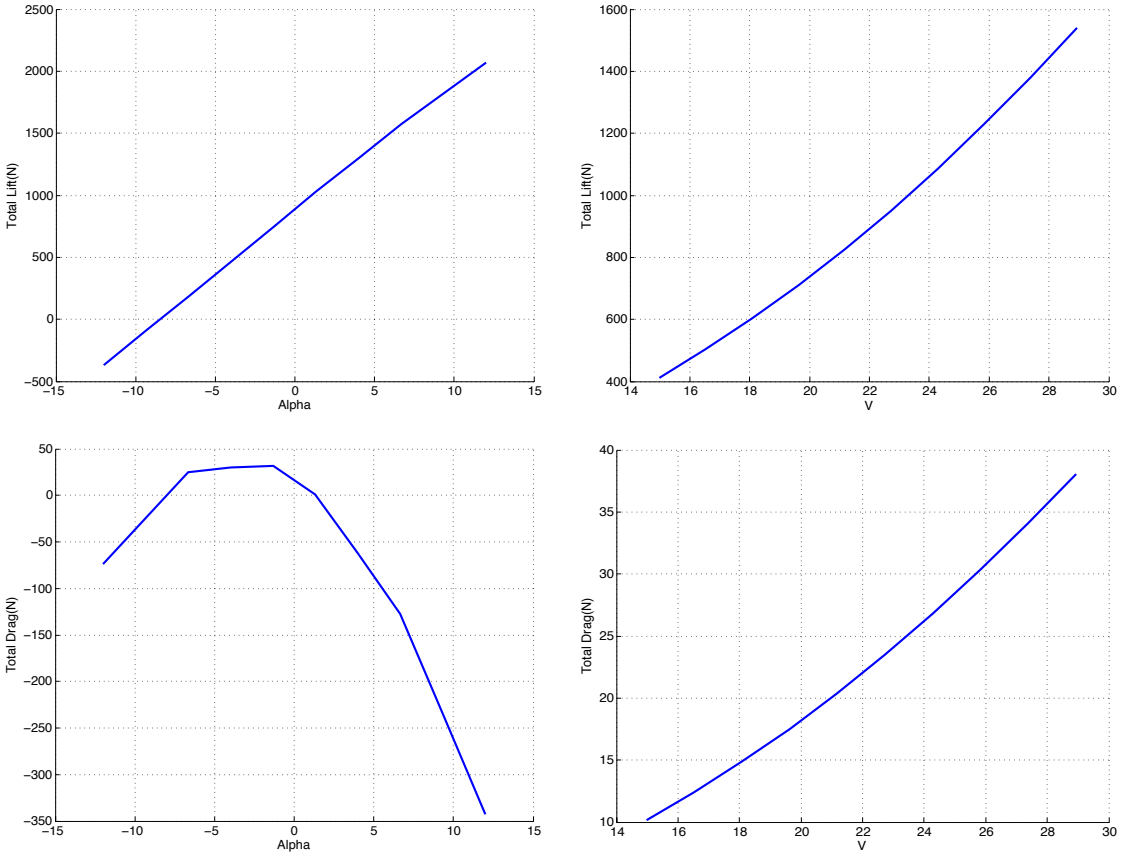

Figure 2.12: Lift and drag forces as functions of angle of attack and airspeed.

2.2.7 Future Revisions

The CSR development is an iterative process, and the presented work only represents the first model development. Several simplifying assumptions are present which will be addressed in future work.

Current derivations treat each satellite vehicle as a rigid body. In reality, the long and slender wing section may experience bend and/or twist during flight. Subsequent developments can model these additional dynamics through a Finite Element Analysis (FEA) or a more refined multibody dynamics model.

The existing model only evaluates individual satellite components, so it does not account for aerodynamic interactions between the components. Items such as wing tip vortices, aerodynamics around the wing and fuselage connection, and interactions between the stabilizers and control surfaces, are not accounted for. Future work will continue to develop the CFD model of the satellite to populate the Matlab look-up table. This data will return forces and moments acting on the satellite for given airspeeds and control inputs.

Finally, a basic linear relationship models the propeller dynamics. More refined models should account for off-axis forces and moments, side airflow into the propeller, blade flapping, and time constants within the motor system dynamics.

2.3 Simulation

With the CSR dynamics established, the final step toward implementing the equations of motion, establishes the relationships between all the rigid body elements. This section formulates the multibody dynamics problem through an illustrative generic example, expands the theory to the Round the Pole (RTP) and CSR systems, and explains how the numerical routine is implemented in Matlab.

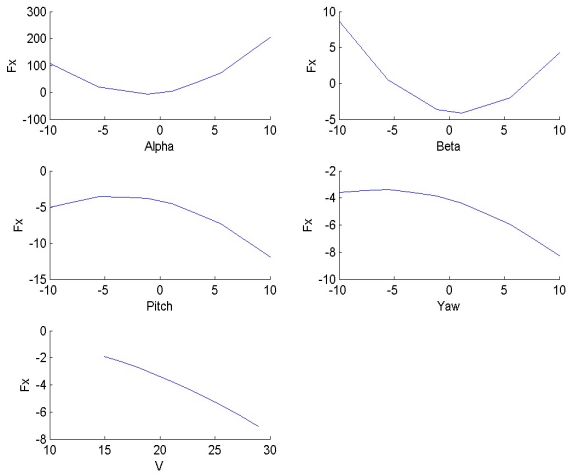

Figure 2.13: Longitudinal force trend.

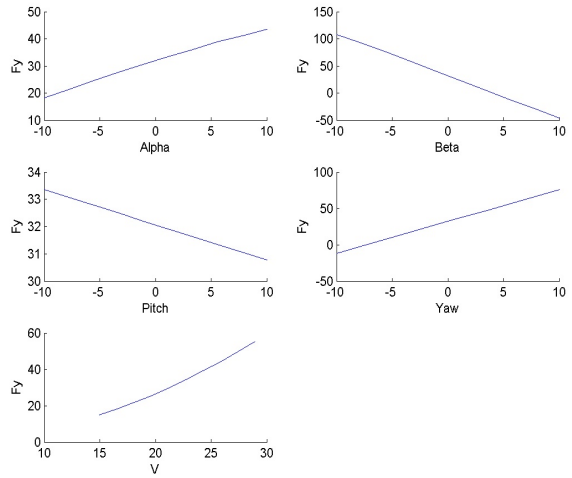

Figure 2.14: Lateral force trend.

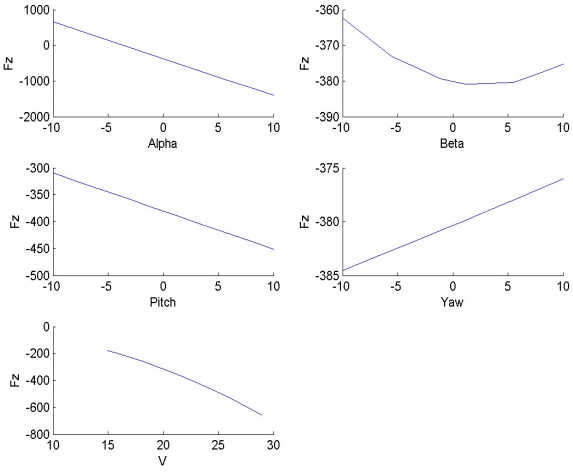

Figure 2.15: Vertical force trend.

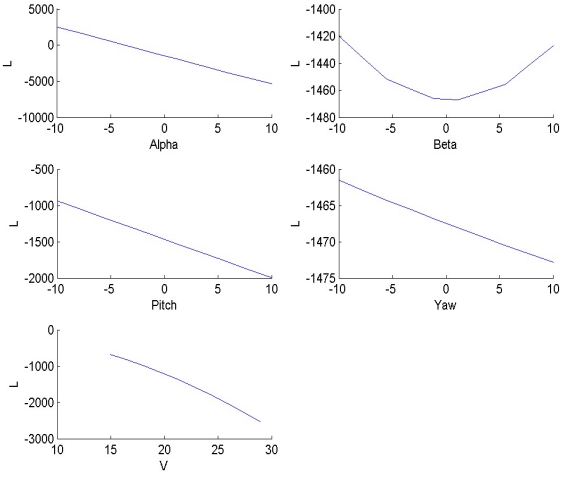

Figure 2.16: Longitudinal moment trend.

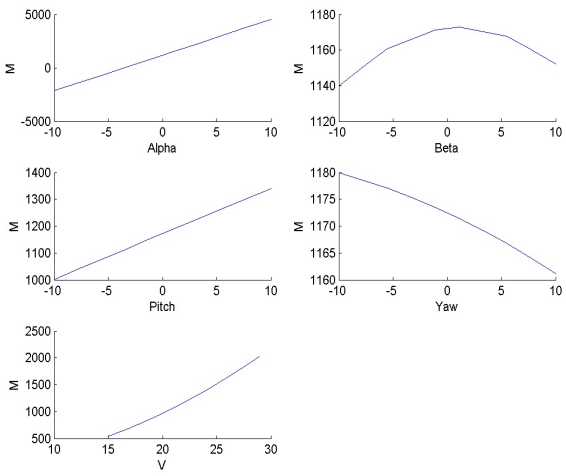

Figure 2.17: Lateral moment trend.

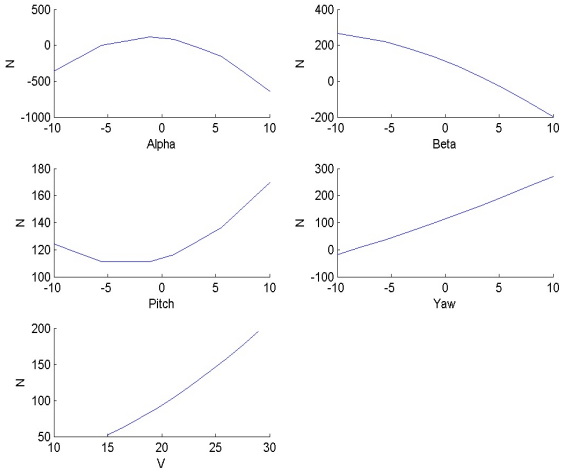

Figure 2.18: Vertical moment trend.

2.3.1 Multibody Dynamics Motivation

Simple elements, like springs and dampers, have an exact representation between forces and states, so a closed form solution is available. With the CSR dynamics, airflow over the tether generates drag forces which are dependent on the current state of the tether, so no closed form solution exists. Therefore, a numerical approach is required to represent the tether in the CSR model.

Several approaches are available to model a multibody system. Hand derivations like Kane's and Lagrange's methods, are laborious and changes to the model or number of elements require new derivations. The following approach is similar to an Finite Element Analysis (FEA) model where each section is modeled as a smaller building block, but FEA linearizes early in the process, and is only suitable for small perturbations.

The CSR simulation implements a multibody dynamics formulation. This approach keeps the nonlinearity in the model, is appropriate for numerical integration, and can be assembled by inspection. This approach offers the most accurate model, and is modular enough to accommodate design revisions and various prototypes during the design process.

2.3.2 Preliminaries

The system is broken down into rigid body subcomponents connected together with spherical joints. The simulation structure represents some states in the inertial frame and other states in a local body frame. This section describes the dynamics of a rigid body, the rotation matrix between coordinate frames, how to express derivatives in different coordinate frames, and a common notation used within the multibody development.

Rigid Body Dynamics

The dynamics of a rigid body under external forces and moments is governed by

$$m\dot{v} = \Sigma F, \quad J\dot{\omega} + \omega \times J\omega = \Sigma M \tag{2.17}$$

where $\Sigma F \in \mathbb{R}^3$ and $\Sigma M \in \mathbb{R}^3$ represent external forces and moments acting on the body, v is the velocity vector in the inertial frame, ω is the angular rate vector, and m and J are the mass and moment inertia of the rigid body.

Rotation Matrix

During the development of the equations of motion, some elements need to be transformed between the inertial frame and its local body frame. When working with Euler angles, the rotation from body frame to inertial frame is given by the rotation matrix R, described by

$$R = \begin{bmatrix} c_\theta c_\psi & -c_\phi s_\psi + s_\phi s_\theta c_\psi & s_\phi s_\psi + c_\phi s_\theta c_\psi \\ c_\theta s_\psi & c_\phi c_\psi + s_\phi s_\theta s_\psi & -s_\phi c_\psi + c_\phi s_\theta s_\psi \\ -s_\theta & s_\phi c_\theta & c_\phi c_\theta \end{bmatrix} \tag{2.18}$$

where sine and cosine (s_*, c_*) act on the attitude (ϕ, θ, ψ) of the element. Rotation matrices possess a special property where the inverse is equal to the transpose, $R^{-1} = R^T$, so mapping from the inertial frame to the body frame is accomplished with R^T.

Derivatives

Differentiation is done with respect to a local frame. The relationship

$${}^N\frac{d}{dt}(v) = {}^B\frac{d}{dt}(v) + {}^N\omega^B \times v = \dot{v} + {}^N\omega^B \times v \tag{2.19}$$

equates time derivatives in the body frame B to the inertial frame N.

Notation

Introduce two operators to keep the notation clean. The cross product of two vectors is equivalent to the matrix multiplication of a skew symmetric matrix and a vector, so that $\tilde{x}y = x \times y$, where

$$\tilde{x} = \begin{bmatrix} 0 & -x_3 & x_2 \\ x_3 & 0 & -x_1 \\ -x_2 & x_1 & 0 \end{bmatrix} \tag{2.20}$$

is the skew symmetric matrix of x. Similarly, a double cross product can be represented in matrix form, so that $\bar{x}y = x \times (x \times y)$, where

$$\bar{x} = \begin{bmatrix} -x_2^2 - x_3^2 & x_1x_2 & x_1x_3 \\ x_1x_2 & -x_1^2 - x_3^2 & x_2x_3 \\ x_1x_3 & x_2x_3 & -x_1^2 - x_2^2 \end{bmatrix} \tag{2.21}$$

is the matrix equivalent double cross product of x.

$$\begin{bmatrix} J_i & 0 & 0 & 0 & -\tilde{r}_i R_i^N \\ 0 & J_o & 0 & 0 & \tilde{r}_o R_o^N \\ 0 & 0 & m_i I_3 & 0 & -I_3 \\ 0 & 0 & 0 & m_o I_3 & I_3 \\ -R_N^i \tilde{r}_i^T & R_N^o \tilde{r}_o^T & -I_3 & I_3 & 0 \end{bmatrix} \begin{bmatrix} \dot{\omega}_i \\ \dot{\omega}_o \\ \dot{v}_i \\ \dot{v}_o \\ F_G \end{bmatrix} = \begin{bmatrix} T_i - \tilde{\omega}_i H_i + T_G \\ T_o - \tilde{\omega}_o H_o - R_o^i T_G \\ F_i \\ F_o \\ R_N^i \bar{\omega}_i r_i - R_N^o \bar{\omega}_o r_o \end{bmatrix} \tag{2.22}$$

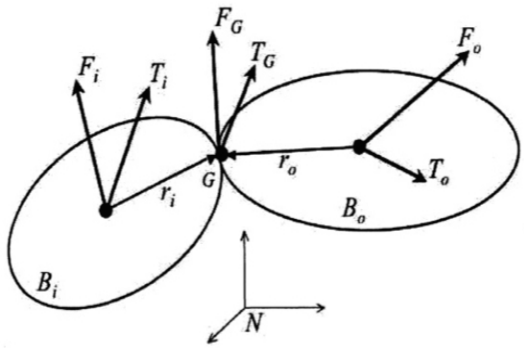

Figure 2.19: Two rigid body model.

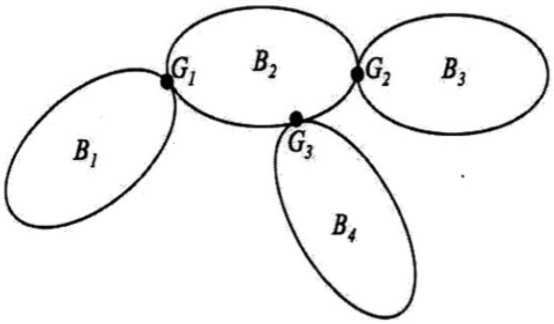

Figure 2.20: Multiple rigid body model.

2.3.3 Two Rigid Bodies

The simplest case to consider is a two body system connected with a spherical joint, which is illustrated in Figure 2.19. There is an inner body B_i and outer body B_o connected at joint G, which has a joint force F_G and joint torque T_G. The joint force and torque are arbitrarily designated as acting in a positive sense on the inner body. Position vectors r_i and r_o extend from each CG to the connection point, and both bodies have a force, F_i and F_o, and torque, T_i and T_o, acting on them.

Euler's equation describes the two relationships for rotation as

$$\begin{aligned} J_i \dot{\omega}_i &= T_i - \omega_i \times H_i + T_G + r_i \times F_G \\ J_o \dot{\omega}_o &= T_o - \omega_o \times H_o - T_G - r_o \times F_G \end{aligned} \tag{2.23}$$

where J_* is the moment of inertia, ω_* is the angular rate vector, and H_* is the angular momentum of the rigid body. When there are no momentum storage devices, the angular momentum term is expressed as $H = J\omega$. Newton's Law gives the relationships for translational as

$$m_i \dot{v}_i = F_i + F_G, \quad m_o \dot{v}_o = F_o - F_G \tag{2.24}$$

where m_* is the mass, and v_* is the velocity vector of the rigid body. A fifth relationship models the velocity of the joint constraint between the two bodies

$$v_G = v_i + \omega_i \times r_i = v_o + \omega_o \times r_o \tag{2.25}$$

and after differentiating within the inertial frame N yields the relationship

$$\dot{v}_i + \dot{\omega}_i \times r_i + \bar{\omega}_i r_i = \dot{v}_o + \dot{\omega}_o \times r_o + \bar{\omega}_o r_o. \tag{2.26}$$

The five equations are put into matrix notation, and rotation matrices are added to convert between coordinate frames. The result is shown in (2.22).

2.3.4 N Rigid Bodies

The previous section laid the ground work for forming the equations of motion. This section expands upon that foundation and generalizes the equations of motion for N rigid bodies, where a sample four body system is depicted in Figure 2.20. A connectivity table identifies the inner and outer bodies of each joint, presented in Table 2.3. Each joint connects two bodies, where i and o designate the inner and outer body, respectively.

	G1	G2	G3
B1	i		
B2	o	i	i
B3		o	
B4			o

Table 2.3: Four body connectivity table.

The equations of motion are formed through inspection using the connectivity table. The matrix relationship for an N rigid body system is given by

$$\begin{bmatrix} J & 0 & R \\ 0 & M & I \\ R^T & I^T & 0 \end{bmatrix} \begin{bmatrix} \dot{\omega} \\ \dot{v} \\ F \end{bmatrix} = \begin{bmatrix} \tau \\ \mathcal{F} \\ \mathcal{C} \end{bmatrix}. \tag{2.27}$$

The states of the system are stored in the first column vector, where $\omega \in \mathbb{R}^{3N}$ contains the angular velocities, $v \in \mathbb{R}^{3N}$ contains the linear velocities, and $F \in \mathbb{R}^{3(N-1)}$ contains the joint constraint forces. The right column vector stores the external torques in $\tau \in \mathbb{R}^{3N}$, the external forces in $\mathcal{F} \in \mathbb{R}^{3N}$, and the constraint relationships in $\mathcal{C} \in \mathbb{R}^{3(N-1)}$. The left matrix is populated with sub matrices. Matrices J and M are each $\mathbb{R}^{3N\times 3N}$ diagonal matrices, that contain the masses and moment inertias for each rigid body. Matrices R and I are both $\mathbb{R}^{3N\times 3(N-1)}$, and follow the same structure as the connectivity table.

Matrix I has negative 3×3 identity matrices for inner body connections, and positive 3×3 identity matrices for outer body connections, formed as

$$I = \begin{bmatrix} -I_3 & 0 & 0 \\ I_3 & -I_3 & -I_3 \\ 0 & I_3 & 0 \\ 0 & 0 & I_3 \end{bmatrix}. \tag{2.28}$$

Matrix R follows an identical sign convention, but is populated with position vectors and rotation matrices, described by

$$R = \begin{bmatrix} -\tilde{r}_{11}R_1^N & 0 & 0 \\ \tilde{r}_{21}R_2^N & -\tilde{r}_{22}R_2^N & -\tilde{r}_{23}R_2^N \\ 0 & \tilde{r}_{32}R_3^N & 0 \\ 0 & 0 & \tilde{r}_{43}R_4^N \end{bmatrix}. \tag{2.29}$$

This concludes the generalized procedure for determining the equations of motion of a multibody system. The next sections apply this procedure to generate the dynamics for two different CSR models.

2.3.5 Round the Pole Model

Part of the CSR development will build a scaled model prototype of the system. Before the complete system is flown in free flight, several development stages will collect data from a single satellite vehicle flying around a fixed pole. This collected data will characterize the satellite and tether model, and flight data compared to simulation data will validate and refine the simulation model. Therefore, a model of the single satellite system is needed for this future work. This section describes the multibody structure of the Round the Pole (RTP) system.

The system layout is shown in Figure 2.21. The multibody structure requires one more rigid body than the number of constraints, so the hub H must be included in the model. The hub should not move with respect to the inertial frame, so it is modeled as a rigid body with an extremely large mass and moment of inertia, and has no gravity acting on the body. This provides a very good model for a pole fixed in the inertial frame.

The model contains a single chain of rigid bodies that start with tether link T_1, work outward to tether link T_n, and finish with the satellite S as the final chain link. The connectivity table has a very simple structure, provided in Table 2.4, which is used to form matrices R and I as described previously.

With n tether elements, there are $N = n+2$ rigid bodies, and $n + 1$ constraints. Each tether element is identical, so they all have the same mass m_T and moment inertia J_T. Sub matrices J and M are both $\mathbb{R}^{3N\times 3N}$ diagonal matrices, where the first three entries contain the hub properties (m_H and J_H), the last three entries contain the satellite properties (m_S and J_S), and the middle $3n$ entries contain the tether properties (m_T and J_T) repeated n times.

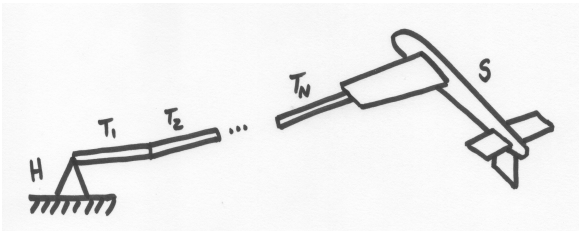

Figure 2.21: Round the Pole (RTP) diagram.

	G_1	G_2	...	G_N
H	i			
T_1	o	i		
T_2		o	i	
$\vdots$			$\ddots$	
T_N			o	i
S				o

Table 2.4: RTP connectivity table.

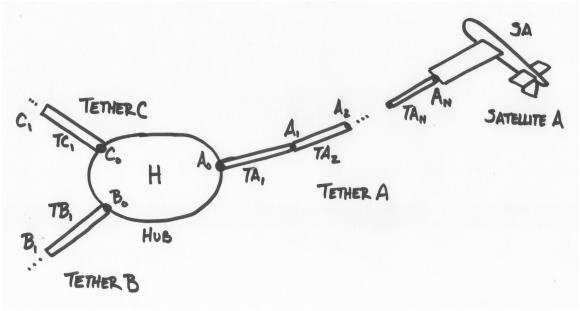

Figure 2.22: Free flight CSR model.

2.3.6 Full System Model

The other model describes the full CSR system. It includes the central hub, three tether arms with satellites, and no external constraints on the system. The system layout is depicted in Figure 2.22.

Several connectivity tables are possible. The most desirable configuration was selected so simulation code could easily scale to accommodate different numbers of tether elements, or additional rigid bodies to model flexibility in the wing section. The connectivity table for the free flight system is shown in Table 2.5, and the other sub matrices are populated in a similar way to the RTP flight model, where the first elements store the hub parameters, the last elements store the satellite parameters, and the inner elements store the tether parameters.

	A_0	B_0	C_0	A_1	...	A_N	B_N	C_N
H	i	i	i					
T_{A1}	o			i				
T_{B1}		o						
T_{C1}			o					
T_{A2}				o				
$\vdots$					$\ddots$			
T_{AN}						i		
T_{BN}							i	
T_{CN}								i
S_A						o		
S_B							o	
S_C								o

Table 2.5: CSR connectivity table.

2.3.7 Future Work

The multibody structure offers a nonlinear model that scales easily and is assembled through inspection. The priority was to develop the dynamics as easily as possible, so controls analysis could begin as soon as possible. However, the current multibody structure has some potential areas of improvement which may be addressed in future work.

The current structure completely models each rigid body and all constraints among them. Many relationships can be expressed in terms of states of neighboring elements. Thus, the current structure models redundant states and does not offer a minimal set. Because the simulation is based on a numerical routine, small numerical discrepancies between these redundant states may accumulate over time.

The simulation runs in Matlab with an ordinary differential equation (ODE) solver. Solving for the derivatives of the states requires the inverse of the square matrix given in (2.27). This is not a concern for a smaller number of rigid bodies, but the size of the matrix grows rapidly with higher fidelity models (more elements are added). The structure of the matrix is predominantly diagonal, so a more efficient inverse procedure may be devised.

2.4 Trimming

Dynamics establishes how the system moves, and the multibody structure implements those equations of motion in the simulation. This section addresses trimming, which seeks the set of states and control inputs that achieve an equilibrium point. In other

words, the set of values that keep the system states and control inputs constant.

Trimming is an important milestone for several reasons. First, it obtains the values for specific flight conditions, like hover and forward flight. These steady state values are also needed to perform linearization, which is required to begin the controls analysis. Finally, trimmed states are used as system initial conditions before running a simulation.

The CSR has a complicated nonlinear model with intertwined states and control inputs, so an analytic approach to determining equilibrium points is not possible. Matlab has built-in functions which can trim certain classes of problems; however, the special structure of the CSR multibody problem precludes the use of these existing functions. This section presents the procedure for trimming the CSR system, addresses limitations with traditional trimming routines applied to multibody dynamics problems, and presents an alternative approach using nonlinear optimization techniques.

2.4.1 Problem Formulation

The objective is to find the system states $x(t)$ and control inputs $u(t)$ to attain an equilibrium point, which means the system is not accelerating. Achieving zero acceleration requires a force balance within all the elements. Thus, the goal is to find values where the forces and moments sum to zero for every rigid body in the system. Following sections illustrate deficiencies with current trimming techniques, and outlines a solution to overcome the problem.

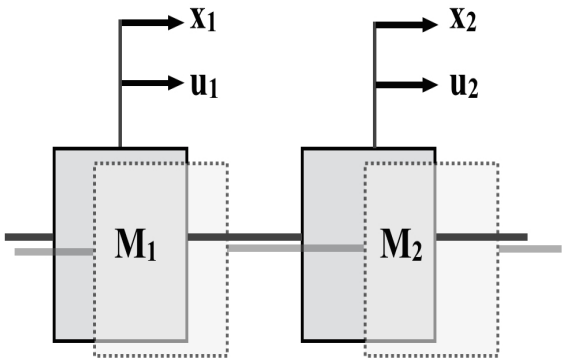

Figure 2.23: Typical model to trim.

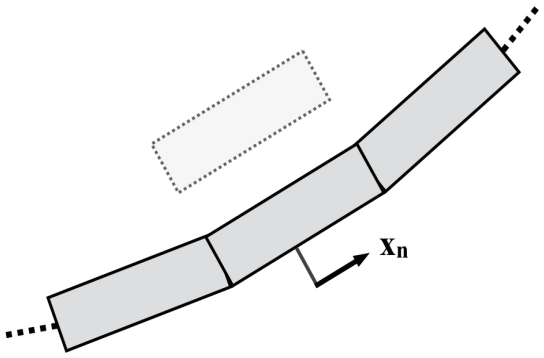

Figure 2.24: Multibody model to trim.

Multibody Trimming Limitation

Many types of modeling problems are formulated as decoupled rigid bodies which are connected together through springs and dampers. Figure 2.23 illustrates this common modeling form. For this arrangement, the masses (and their states) are independent of one another, so a single state can be perturbed while the others remain static. In the multibody dynamics structure, the rigid bodies must maintain joint constraints, so the states of the rigid bodies are not independent. Perturbing a single rigid body element leads to a disjoined chain structure, depicted in Figure 2.24. This is not a viable solution, so an alternative trimming procedure alleviates this concern.

Optimization Function

Trimming is a type of optimization problem. The Matlab function, `lsqnonlin`, solves nonlinear least-squares curve fitting problems. The input is a vector x with initial condition x_0, and a vector as a function of x is the output

$$f(x) = [\ f_1(x)\ f_2(x)\ \cdots\ f_n(x)\ ]^T. \tag{2.30}$$

The optimization routine solves

$$\min_x \|f(x)\|_2^2 = \min_x \left(f_1(x)^2 + f_2(x)^2 + \cdots + f_n(x)^2\right) \tag{2.31}$$

which minimizes the square of the Euclidean norm of the vector function.

Process Overview

The trimming process is accomplished in two loops: an inner loop and an outer loop. The inner loop

starts at a tether anchor point and works outwards toward the satellite. Optimization runs on each rigid body to achieve a force balance within that element. After the satellite has been optimized, the entire tether arm achieves a force balance condition. However, the lift generated by the satellite depends entirely on the initial values used at the hub, so there is no assurance that the generated lift equals the required lift. The outer optimization loop incrementally adjusts the hub rotation and anchor point forces, runs the inner loop again, and reevaluates the amount of lift generated. The outer loop optimization continues until there is a force balance within the central hub.

2.4.2 Optimization

The trimming routine uses several different optimizations to to obtain a force balance within the elements. The first optimization balances a single tether element. Then a loop applies this routine to all the links in the tether. Another optimization finds the satellite states and control inputs to achieve a force balance within the outermost segment of the tether chain. This process completes the inner loop routine. The final optimization seeks a force balance within the central hub. This outer loop optimization adjusts the hub angular velocity and tether anchor force until the lift generated by the satellite equals the weight it needs to support. The following sections describe each process in detail.

Tether Force Balance

Consider a single tether element. The goal is to find the state that achieves a force balance between all the forces acting on the element. These forces include the inner and outer joint constraint forces, F_i and F_o, a centrifugal force F_c, aerodynamic drag F_d, and gravity F_g. Assume that the hub angular rate and the tether's inboard position, velocity, and force are all known. The attitude of the element dictates the CG location and the direction of relative airflow over the tether section. These states determine the drag force, centrifugal force, and outboard endpoint force. The optimization adjusts the attitude of the tether until the force balance equality

$$F_i + F_c + F_d + F_g + F_o = 0 \tag{2.32}$$

is satisfied. A similar relationship balances the moments acting on the tether element.

Tether Projection

The previous section outlined a process that takes an inboard tether state, balances the forces within the element, and returns the outboard tether state. Tether projection describes a program loop that balances all the elements of the tether. The loop starts with the hub anchor force and the angular rate of the hub, and applies the optimization to the inner most tether element. The outboard states of this first element become the inboard states for the next element. The loop proceeds outward through each section until it reaches the final tether element. The outboard states of the final tether are used as the anchor position, velocity and force for the satellite.

Satellite Force Balance

The satellite optimization is very similar to the tether optimization. The tether end point states were determined from the tether projection loop, but the satellite attitude and control inputs are still unknown. As a starting point, the satellite is initialized with a zero attitude, zero control surface deflection, and a reasonable guess value for throttle input. The optimization takes the tether end point states, and the current values for satellite attitude and control inputs. For this particular state, the program evaluates the centrifugal force and aerodynamic forces/moments, calculates the summation of forces and moments on the satellite, and compares this value to zero. The optimization incrementally adjusts the satellite states and control inputs until the net forces and moments are reduced to zero. This completes the inner loop.

Hub Force Balance

The previous sections describe the inner loop which balances the entire tether arm with a satellite. That

process began with an initial guess for the hub anchor force and system angular rate. Using these initial guess values, the lift generated from the satellite may not equal the lift force needed for the system. Therefore, an outer loop optimization is needed to balance the hub forces. The optimization compares the current amount of lift to the force required to support the weight of the entire system. It also balances the moment generated by the tether force with the rotational aerodynamic drag from the spinning hub. If the net forces and moments are non zero, the optimization routine adjusts the hub angular rate and the hub anchor force, and then runs another inner loop optimization. This iterative process continues until the hub and satellite achieve static equilibrium. Once the CSR system is completely balanced, the states and control inputs are stored as initial conditions for the simulation and as operating points for linearization.

2.4.3 Initial Guess Values

All the minimization routines require initial conditions to begin the optimization process. Values for the inner loop optimizations (tether and satellite) were initialized locally. However, the outer loop initial conditions (hub angular rate and anchor force) are still unaccounted for. This section presents derivations that yield approximate values suitable for initializing the outer loop optimization. It addresses the satellite lift force, linear velocity, and position, which is used to estimate the system angular rate and anchor forces.

Lift Force

The masses of the elements are known, so the first step finds the total weight of the system. There are three tether arms, so the lifting force required of each satellite must carry one third of the total weight of the system. The program stores the required lift force F_S which is used in the next section.

Satellite Velocity

The lift equation is given by

$$F_S = (1/2)\rho v_S^2 A c_{SL} \tag{2.33}$$

where F_S is the satellite lift force previously calculated, ρ is the density of air, v_S is the forward linear velocity of the satellite, A is the planform area of the wing, and c_{SL} is the lift coefficient of the satellite wing. The only unknown value in this relationship is the satellite velocity. Rearranging the equation leads to the equality

$$v_S = \sqrt{\frac{2F_S}{\rho A c_{SL}}} \tag{2.34}$$

which yields the forward velocity v_S required to achieve the desired lift force F_S. This result assumes a level flight condition. The true velocity will be slightly greater to because the trimmed satellite attitude will not be perfectly level.

Satellite Position

During flight the tether will curve from aerodynamic drag and from the force of gravity. The amount of curvature is unknown until after the optimization routine. As a starting point, assume the tether has no curvature and projects straight out towards the satellite. The hub anchor position, the length of the tether, and the satellite anchor position have known dimensions, which can be added together to obtain r_S, an approximate starting position for the satellite.

Satellite Angular Rate

With an approximate satellite position and velocity, the next step estimates the angular rate ω_H of the central hub. Relating the satellite position r_S and velocity v_S with

$$\omega_H = \frac{v_S}{r_S}. \tag{2.35}$$

yields the estimated angular velocity ω_H.

Anchor Force

The final set of calculations estimate the force vector acting at the hub anchor points. The estimated satellite position r_S and the hub angular rate ω_H determines the centrifugal force F_x described by

$$F_x = m_S r_S \omega_H^2 \tag{2.36}$$

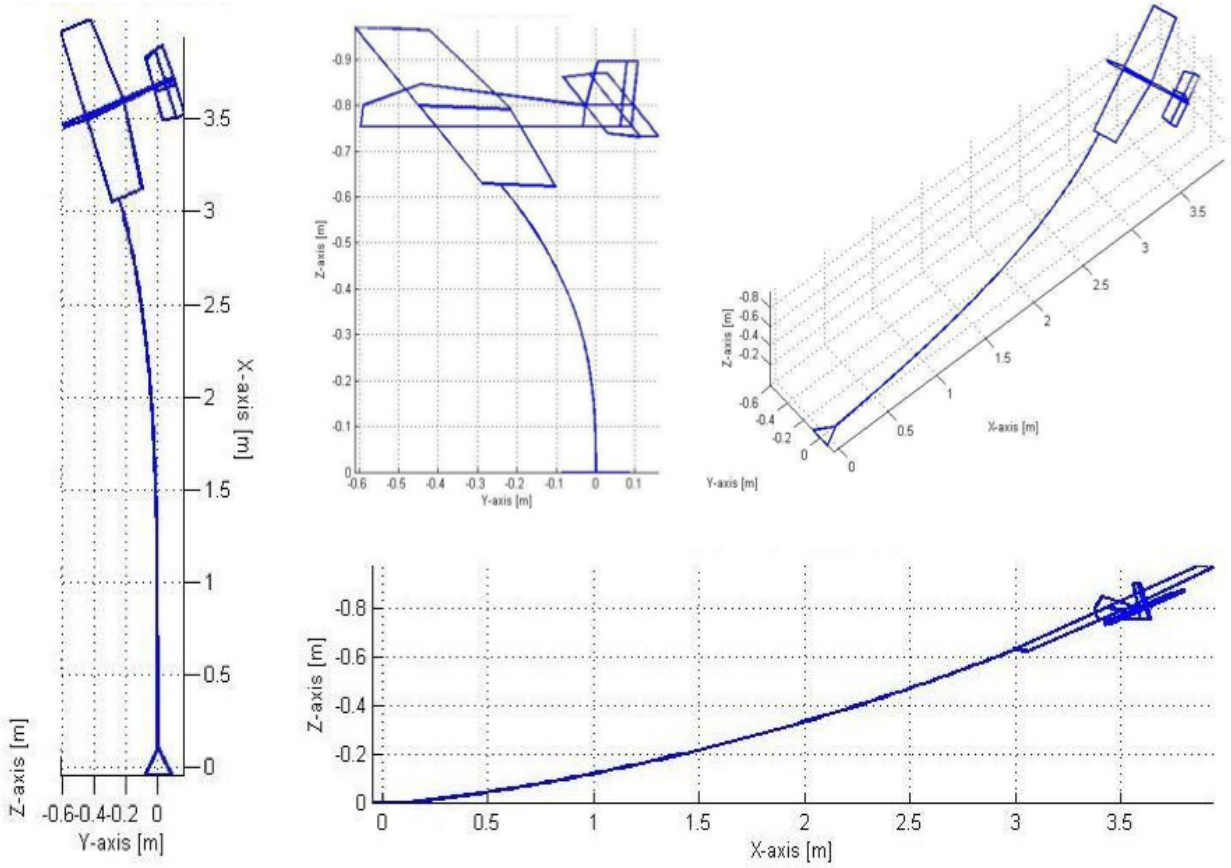

Figure 2.25: Various views of the trimmed RTP system.

where m_S is the mass of the satellite. Rotational aerodynamic drag dictates F_y with

$$F_y = \frac{1}{3}\frac{c_{Hmz}\omega_{Hz}^2}{r} \tag{2.37}$$

where $M_{Hz} = c_{Hmz}\omega_{Hz}^2$ is the z-axis moment on the hub for a particular angular rate, r is the distance from the hub CG to the tether anchor point, and the one third term equally distributes the force to each of the satellite anchor points. The vertical force F_z is influenced by gravity g and the mass of the hub m_H described by

$$F_z = -(1/3)m_H g \tag{2.38}$$

where the one third distributes the total force to each tether arm, and the negative sign remains consistent with the coordinate frame.

2.4.4 Plots of Trimmed Systems

The previous sections described the process for trimming the RTP and CSR systems. This section presents the results of that effort by displaying two figures of the trimmed systems.

Figure 2.25 depicts several perspective views of the trimmed RTP system. Tether parameters (density, diameter, mass) were set to larger values to exaggerate the effects of drag and gravity, and to showcase the trimming routine. Notice, that the tether bends uniformly in the vertical direction from gravity, and the horizontal curvature becomes more pronounced outward as drag increases. Furthermore, the CG of the satellite aligns with the tether endpoint force vector, as expected.

Figure 2.26 displays the states of a trimmed CSR satellite in the inertial frame. The satellite flies a circle around the hub, so the horizontal position and velocity are sinusoidal. The central hub rotates at a constant velocity, as seen in the upper right corner. All other states are in static equilibrium, so they maintain very nearly zero values.

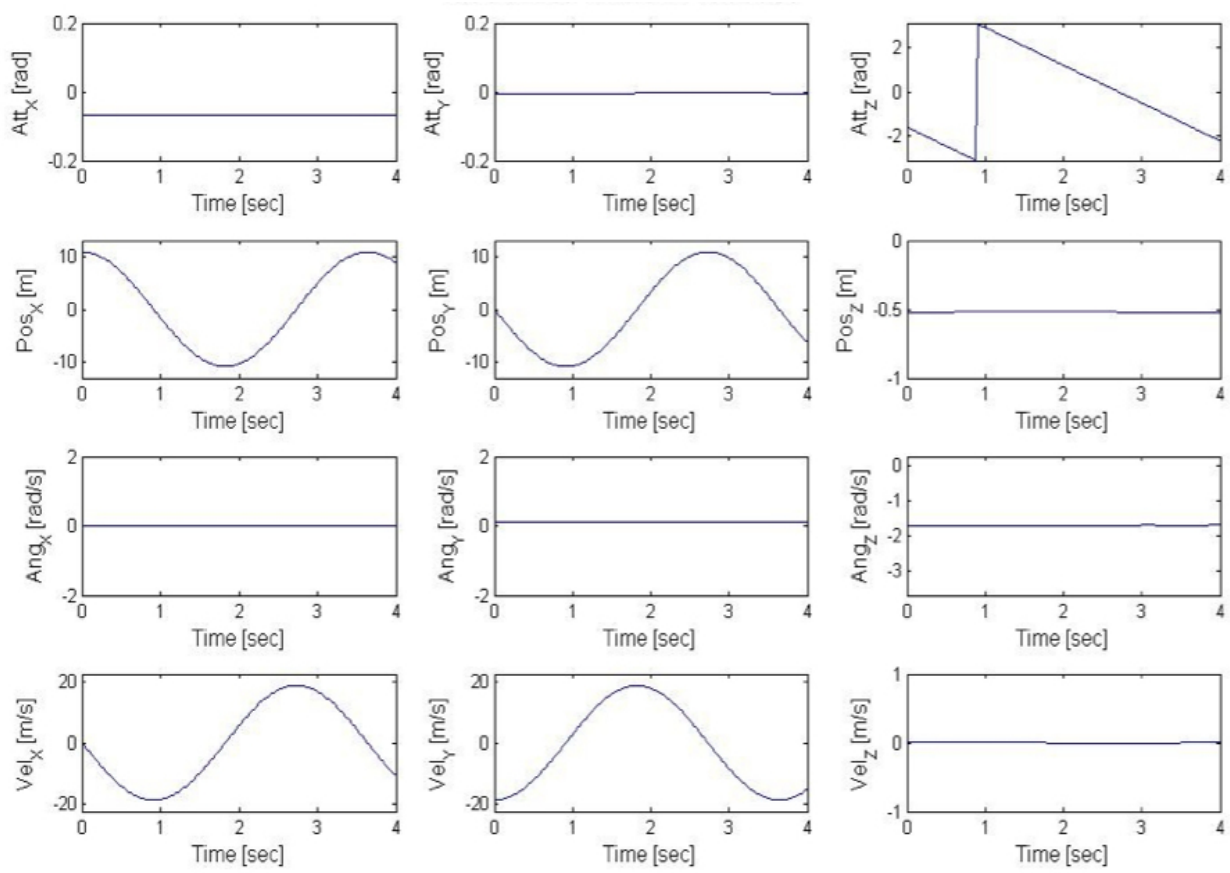

Figure 2.26: Trimmed CSR satellite states in the inertial frame.

2.5 Linearization

Thus far, the CSR plant has trimmed operating points and nonlinear dynamics implemented in the simulation. The last step toward developing the CRS plant, takes the nonlinear system and creates a linear model around those trimmed operating points.

Linearization is an important topic because the vast majority of the controls analysis is based on the linear system model. Linearizing multibody dynamics problems have many of the same hurdles as with trimming, so this research utilizes the alternative trimming technique and adapts it to the linearization process for multibody dynamics problems.

This section presents the Taylor series expansion of a nonlinear model, and describes how the partial derivatives form state space matrices of the linear system. It addresses issues with linearizing multibody dynamics problems, proposes an alternative approach, and presents the matrices that represent the Matlab simulated COTS control line aircraft.

2.5.1 Taylor Series Expansion

The equations of motion of the plant are expressed in compact form as $\dot{x}(t) = f(x(t), u(t))$ where $x(t) \in \mathbb{R}^n$ are the n states of the plant and $u(t) \in \mathbb{R}^m$ are the m control inputs. Denote an operating point as $\hat{x}$ and $\hat{u}$, so that perturbations are described by $\Delta x = x - \hat{x}$ and $\Delta u = u - \hat{u}$.

Taylor series expansion for the nonlinear system is described by

$$\dot{x} = f(x,u) \cong f(\hat{x},\hat{u}) + \frac{\partial f}{\partial x}_{(\hat{x},\hat{u})} (x - \hat{x}) + \frac{\partial f}{\partial u}_{(\hat{x},\hat{u})} (u - \hat{u}) + HOT \tag{2.39}$$

and disregarding the higher order terms (HOT),

yields the form

$$\Delta\dot{x} = f(\hat{x}, \hat{u}) + A\Delta x + B\Delta u \tag{2.40}$$

where the state matrix A is described by

$$A = \begin{bmatrix} \frac{\partial f_1}{\partial x_1} & \frac{\partial f_1}{\partial x_2} & \cdots & \frac{\partial f_1}{\partial x_n} \\ \frac{\partial f_2}{\partial x_1} & & & \\ \vdots & & \ddots & \vdots \\ \frac{\partial f_n}{\partial x_1} & & \cdots & \frac{\partial f_n}{\partial x_n} \end{bmatrix} \tag{2.41}$$

and the input matrix B is given by

$$B = \begin{bmatrix} \frac{\partial f_1}{\partial u_1} & \frac{\partial f_1}{\partial u_2} & \cdots & \frac{\partial f_1}{\partial u_m} \\ \frac{\partial f_2}{\partial u_1} & & & \\ \vdots & & \ddots & \vdots \\ \frac{\partial f_m}{\partial u_1} & & \cdots & \frac{\partial f_m}{\partial u_m} \end{bmatrix}. \tag{2.42}$$

When an operating point is also an equilibrium point (derivatives are equal zero), then $f(\hat{x}, \hat{u}) = 0$ and the system reduces to $\Delta\dot{x} = A\Delta x + B\Delta u$ where future equations omit the Δ symbol for readability.

2.5.2 Process

For simple systems with closed form solutions, the partial derivative terms that form A and B matrices may be obtained by hand calculations. Because the CSR system requires a numerical routine (does not have a closed form solution) this is not a viable option. Matlab has built-in functions that linearize a wide range of systems. However, the Matlab process is expecting a model that resembles Figure 2.23, which is not suitable for multibody problems.

An alternative approach is used. For each entry in the A matrix select a single state (x_j) at equilibrium. Adjust this value by a small increment δ in both directions of its nominal trimmed value (x_j^+, x_j^-), while all other states are kept at their equilibrium values. For reference, call this the *ideal perturbed state vector*. Traditional trimming routines run the system dynamics at this point, but for a multibody problem the perturbed system resembles Figure 2.24, which is not a valid configuration.

The ideal perturbed state vector does not maintain the physical constraints of the problem, so an alternative vector is sought. The goal is to find the set of states that are as close as possible to the ideal perturbed state vector, and call this new set the *actual perturbed state vector*. Run `lsqnonlin` optimization to find the "closest match", which minimizes the Euclidean norm of the difference between the ideal perturbed state vector and the actual perturbed state vector.

Using x_j^+ and x_j^-, two optimizations return two actual perturbed state vectors $\bar{x}_j^+$ and $\bar{x}_j^-$. These state vectors are passed into the system dynamics, which return two derivative function vectors

$$\bar{f}_j^+ = f(\bar{x}_j^+, \bar{u}), \quad \bar{f}_j^- = f(\bar{x}_j^-, \bar{u}) \tag{2.43}$$

Working through each row of the derivative vector yields the partial derivatives

$$\frac{\partial f_i}{\partial x_j} \approx \frac{f_{ji}^+ - f_{ji}^-}{x_j^+ - x_j^-} = \frac{f_{ji}^+ - f_{ji}^-}{2\delta}. \tag{2.44}$$

The code runs through a loop and performs this process for each state x_j for $j = 1, \ldots, n$ which populates the A matrix. An identical process is used with the control inputs u to derive the B matrix.

2.5.3 RTP State Space Form

This section applies the linearization process to the Round the Pole system, where the state Matrix A and input matrix B are provided in (2.45). The first step defines the states and inputs within the system.

There are three control inputs for each satellite; throttle, elevator, and rudder. These control signals influence the relative positions between the hub and the satellite. The throttle impacts relative horizontal states, the elevator impacts relative vertical states, and the rudder impacts relative heading states.

The RTP system has ten total states. The first two are the roll and pitch of the satellite. The next three express relative positions between the satellite and hub. They are heading, horizontal position, and vertical position. The final five states are the derivatives of the first five states.

Initially, it is assumed that all states are available for measurement, which allows for full state feedback control. However, standard GPS is not accurate enough to measure the relative positions of the

$$A = \begin{bmatrix} 0 & 0 & 0 & 0 & 0 & 1 & 0 & 0 & 0 & 0 \\ 0 & 0 & 0 & 0 & 0 & 0 & 1 & 0 & 0 & 0 \\ 0 & 0 & 0 & 0 & 0 & 0 & 0 & 1 & 0 & 0 \\ 0 & 0 & 0 & 0 & 0 & 0 & 0 & 0 & 1 & 0 \\ 0 & 0 & 0 & 0 & 0 & 0 & 0 & 0 & 0 & 1 \\ -22.90 & -0.99 & 2.23 & 0.02 & -3.64 & 0 & 0.00 & -0.00 & 0.01 & -0.07 \\ 0.23 & -59.95 & 7.77 & -0.23 & 0 & 0 & 0 & 0 & 0 & -5.91 \\ -0.27 & -5.50 & -62.64 & 1.39 & -1.92 & 0.00 & 0 & -0.00 & 0.01 & -0.17 \\ 0.39 & 14.19 & -0.67 & -0.00 & 2.00 & -0.00 & 0 & -0.00 & -2.45 & 0.11 \\ 1.71 & -187.75 & 28.26 & -0.91 & 0 & 0 & -0.02 & -0.18 & 1.59 & -9.40 \end{bmatrix} \quad B = \begin{bmatrix} 0 & 0 & 0 \\ 0 & 0 & 0 \\ 0 & 0 & 0 \\ 0 & 0 & 0 \\ 0 & 0 & 0 \\ 0 & 0.11 & -1.33 \\ 0 & 12.41 & 0 \\ -0.01 & 0 & 13.78 \\ -0.54 & 0.01 & -0.04 \\ 0 & 13.70 & 0.07 \end{bmatrix} \tag{2.45}$$

satellites. More elaborate GPS techniques, like differential GPS, RFID triangulation, landmark tracking, and INS navigation might offer a localization solution after further review. As a worst case scenario, this research assumes that relative satellite positions will not be available, and introduces controllers with state estimation and reduced order state estimation which can control the system without measuring the exact location of the satellite.

Chapter 3

Controls Theory

The system dynamics are implemented within the simulation environment, and the vehicle model is trimmed and linearized. The current task reviews the controllers developed for the CSR vehicle. Fundamental concepts are presented which describe the system to be controlled and the properties used during control design. Controllers with progressive levels of sophistication are introduced and related back to their purpose for the CSR system.

Motivation

The CSR concept vehicle is a radical departure from customary aircraft design, so there is no existing research to indicate that a particular control strategy is best suited for this type of system. The general design methodology for this research starts with basic models and controllers, learns more about the particular system, and then refines and expands the models and controller capabilities over time.

The full CSR system does not have any direct control over the central hub. Stabilizing and maneuvering the hub, as well as the rest of the system, is accomplished indirectly through the tension in the tethers, which is manipulated by the control inputs applied to each individual satellite vehicle. Investigating these interactions is the first step towards developing the system controllers.

Understanding the background theory used during the controller development is of utmost importance in understanding how the controller is implemented. The purpose of this chapter introduces concepts of state feedback and state estimation to a technical audience not well versed in control design. Entire text books address the underlying theory of these controllers, so this content strives to deliver the most pertinent concepts needed to understand basic principles used for the CSR controller.

Objectives

The primary goal of this initial research is to demonstrate that the CSR vehicle is a viable design concept, and that a controller exists which can successfully navigate the system. Because no control theory is established for this system, the research on the CSR concept vehicle includes several different controller methodologies. Prerequisite knowledge is required before applying these techniques, so the goal is to present fundamental concepts and then graduate to more advanced strategies.

Before introducing the controllers, it is important to understand the concept of a plant, which is the system to be controlled. Describing how to express a system in state space form, how to determine the eigenvalues, and understanding how those eigenvalues contribute to the overall response of the system, is required to understand the controller theory. Other topics are directly related to the controller development. Theory on controllability and observ-

ability, and canonical transformations are needed to understand the controller formulation.

After developing a firm foundation, the various controllers are presented. The analysis works from simple techniques to more advanced concepts, so the starting point for the controls analysis begins with full state feedback applied to single-input single-output (SISO) subsystems, which provides a foundation for multiple-input multiple-output (MIMO) control. Full state feedback assumes that all the satellite states are available for measurement, which is not possible due to the limitations with GPS. State estimation addresses this issue, where a reduced order estimator is required to estimate unknown states. Finally, parameter identification and mitigating model uncertainty is only achieved through adaptive control techniques.

Outline

Before assessing any eternal flight capabilities, The CSR vehicle must demonstrate an ability to be controlled during flight. This chapter focuses on the controls theory and analysis to address this issue.

Section 3.1 presents the *Controller Methodology* which makes the CSR control problem more tractable. It describes the available control modes, presents an alternative perspective, and defines the roles of the inner and outer loop feedback systems.

Section 3.2 outlines the *System Analysis* performed on the CSR model. It describes its state space representation, transfer matrix, eigenvalues, and system poles and zeros. Topics pertaining to controllability, observability, and decentralized control are related back to the system model.

Section 3.3 describes *SISO State Feedback* which is the first control implemented on the vehicle. A custom designed system response is put into a canonical transformation, and implemented through the state feedback controller.

Section 3.4 expands to *MIMO State Feedback* which accommodates coupling between input and output channels. The SISO structure is generalized to handle multiple inputs and multiple outputs, while still achieving a custom closed-loop response.

Section 3.5 addresses *State Estimation* which is used when some of the CSR states are not directly measured. Control inputs and measured outputs are used to estimate the states and reduce the error to zero over time. Then a reduced order estimator is implemented to only estimate unknown states.

Section 3.6 introduces *Adaptive Control* which accomplishes system identification and mitigates modeling uncertainties. It presents a parameter identification technique where the adaptive laws ensure stability and parameter convergence. Finally, it discusses model reference adaptive control (MRAC) and L_1 adaptive control strategies.

3.1 Controller Methodology

At first glance, controlling the CSR vehicle appears very complicated, which requires full cooperation from all entities involved. However, this research will show that a slight shift in perspective makes the control problem much more tractable.

This section outlines the different control modes available for the CSR system, which leads into an alternative perspective describing the big picture approach developing the system controller. It describes the roles of the inner and outer loop controllers, and draws a parallel between the controller development and the prototype hardware development.

3.1.1 Control Modes

Before embarking on the specifics of the CSR controller development; first recognize that the novel CSR design operates in a perpetual state of rotation. Thus, it is important to redefine some common conventions used within general aviation.

Roll and pitch are synonymous, because there is no “nose” or “side” to differentiate between them. Roll and pitch describe the same flight maneuver for any given direction in the inertial frame. Likewise, yaw is arbitrary, because the system rotates constantly. Yaw only has meaning referring to an instrument (like a camera system) that maintains a static heading. Accounting for the specifics of the CSR geometry, only two inertial descriptions are needed: vertical translation and horizontal translation.

Borrowing from rotorcraft terminology, vertical translation utilizes collective control inputs, and hor-

izontal translation uses cyclic control inputs. Horizontal and vertical translation both have two control modes available to induce each type of motion.

For vertical translation, the first mode applies collective throttle commands. This changes the satellite velocity which alters the lift force. Changing the lift force in unison results in a climb or a descent. The other mode applies collective elevator commands. This changes the satellite pitch angle, which points the nose of the satellite up or down. With all satellites pointing upward or downward, the system enters into a climb or descent.

Similarly, two cyclic control modes exist for horizontal translation. The first mode applies cyclic rudder commands. This changes the relative heading of the satellites, which adjusts the radial tension in the tethers acting on the hub. The command is cyclic, so one point in the rotation has maximum outward tension, and the opposite side has minimum radial tension. Because the forces are imbalanced, the CSR system translates horizontally in the direction of maximum tension. Cyclic elevator commands can also achieve horizontal translation. This command influences the relative vertical position of the satellites, so each satellite flies through a low point on one side and a high point directly opposite. This coordinated flight has the effect of tilting the rotor plane, which tilts the overall force vector and induces horizontal translation.

3.1.2 Alternative Perspective

Controlling the CSR vehicle appears to be a very complicated task. With many different states, multiple tethers and satellites, and force interactions pulling on the central hub, the problem appears to require full cooperation from all entities involved.

In many ways, the coordinated effort resembles a highway traffic system. When viewed from above, the number of vehicles and potential routes make the traffic system appear unmanageable. However, driving is a very simple task as as seen from the driver's seat. As long as each driver adheres to basic rules (stay centered within a lane, keep a safe following distance, obey traffic signals), the complex driving system becomes much more tractable.

The same approach can be applied to the CSR vehicle. Imagine sitting on the hub while peering at an individual satellite, operating in a trimmed state with no external disturbances. From this perspective the satellite will maintain a static position relative to the hub. It will appear to be "fixed" in space.

The control task identifies meaningful relative positions of the satellite with respect to the hub, then applies control signals to manipulate the relative states of the satellite. Altering the relative states changes the tether force vector anchored at the hub. Manipulating the tether anchor forces controls the central hub and the entire CSR system.

3.1.3 Inner and Outer Loop Control

Previous sections described the motion of the CSR system in the inertial frame, and how to control satellites with respect to their local frame. These two tasks indicate that two control loops are required for the control system. An inner loop controller is responsible for stabilization, and an outer loop controller executes the waypoint navigation.

Inner loop control works locally on each satellite. The controller adjusts the throttle, elevator, and rudder of each satellite. These inputs maintain the desired relative positions with respect to the central hub. This subsystem is mirrored as a Round the Pole (RTP) flight model.

Outer loop control works globally on the central hub. This moves the CSR vertically and horizontally within the inertial frame. The controller accomplishes this task by manipulating tether forces acting on the hub anchor points. It achieves this because tether anchor forces are mirrored by the relative positions of the satellites.

3.1.4 Parallel with Hardware Testing

The CSR project follows a spiral development life cycle. Because of the novel design, there is very little existing research to assist the development process. To minimize risk during early development, small incremental steps are taken to learn about the system, collect data, and refine simulation models. More advanced techniques are introduced over time, building upon previous lessons learned.

The first prototype system implements RTP flight. For this model, a single satellite flies around a fixed pole. The main task identifies trimmed control inputs and performs system identification on the vehicle. Collected data is compared to simulation data, and the computer model is revised to more closely match the physical system.

The next milestone is a fixed flight. This model has three satellites constrained to a pole. The primary objective maintains equal spacing between the satellites, and tests coordinated flight maneuvers. Equal spacing between satellites is a requirement before graduating to a free flight test. Similarly, coordinated flights demonstrate collective and cyclic commands executed by the satellites. These capabilities are accomplished within a controlled environment, before advancing to a free flight.

The final stage implements the free flight model. This is the fully unconstrained CSR system. The objective is to demonstrate hover abilities and to achieve waypoint navigation through coordinated flight maneuvers. Once a flying prototype is available, the research will evaluate disturbance rejection and the effectiveness of various adaptive controllers.

3.2 System Analysis

Previous work described the modeling and dynamics that describe the RTP and CSR systems. This section presents concepts that analyze the plant from a controls perspective. It introduces the idea of a plant, and describes the state space and transfer function forms. It covers the characteristic polynomial of the system, the process for determining the system eigenvalues, and how those relate to the poles and zeros of the system. Finally, it addresses controllability, observability, and decentralized control.

3.2.1 System Description

The plant is the physical system to be controlled. It is a mathematical model that relates the control inputs $u(t)$ to the system outputs $y(t)$. A linear time-invariant (LTI) model of a physical system is expressed in state space form as

$$\dot{x}(t) = Ax(t) + Bu(t), \quad y(t) = Cx(t) \tag{3.1}$$

where $x(t) \in \mathbb{R}^n$ is the state vector, $u(t) \in \mathbb{R}^m$ is the control input, $y(t) \in \mathbb{R}^q$ is the system output, $A \in \mathbb{R}^{n\times n}$ is the state matrix, $B \in \mathbb{R}^{n\times m}$ is the input matrix, and $C \in \mathbb{R}^{q\times n}$ is the output matrix. The most general form of a state space system includes a feedforward matrix, $D \in \mathbb{R}^{q\times m}$. However, this term does not appear in physical systems, and is dropped from subsequent derivations.

The system (3.1) describes a multiple-input multiple-output (MIMO) system. For single-input single-output (SISO) systems, the input $u(t)$ and output $y(t)$ become scalar values, and B and C matrices reduce to vectors with appropriate dimensions.

3.2.2 Transfer Function/Matrix

The transfer function $G(s)$ of a SISO LTI state space model expresses the relationship between the control input and the system output of the system with zero initial condition and zero point equilibrium. The plant transfer function $G(s)$ can be obtained directly from the state space model.

Convert the time domain representation of (3.1) to the frequency domain with the Laplace transform

$$sX(s) = AX(s) + BU(s), \;\; Y(s) = CX(s) \tag{3.2}$$

solve for $X(s)$ as

$$\begin{aligned} sX(s) - AX(s) &= BU(s) \\ (sI - A)X(s) &= BU(s) \\ X(s) &= (sI - A)^{-1}BU(s) \end{aligned} \tag{3.3}$$

substitute $X(s)$ into the output equation

$$Y(s) = C(sI - A)^{-1}BU(s) \tag{3.4}$$

and define the transfer function $G(s)$ as

$$G(s) = C(sI - A)^{-1}B \tag{3.5}$$

which satisfies the relationship

$$G(s) = \frac{Y(s)}{U(s)} \tag{3.6}$$

as desired. This relationship is expressed in block diagram notation depicted in Figure 3.1.

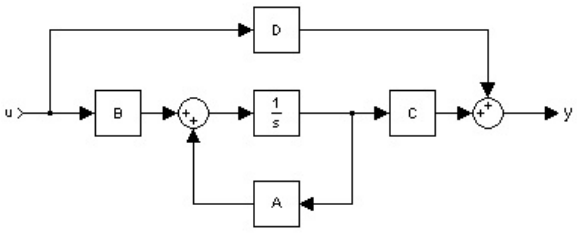

Figure 3.1: Block diagram of the plant model.

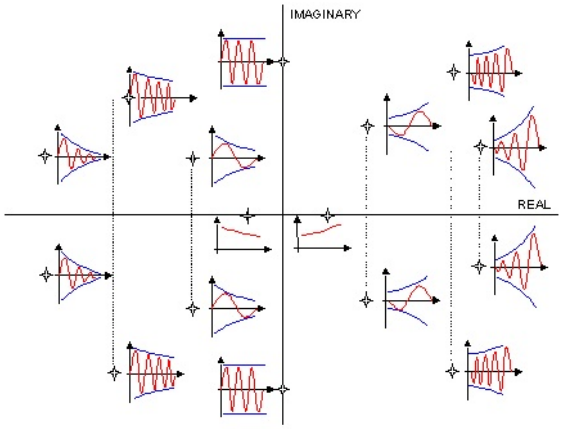

Figure 3.2: System poles in the complex plane.

For a SISO system, the transfer function $G(s)$ is single a rational polynomial that relates a single input to a single output. For MIMO systems, $G(s)$ becomes a transfer matrix which is populated with rational polynomials within the matrix elements.

3.2.3 System Eigenvalues

The transfer function $G(s)$ has an equivalent representation formed by replacing the inverse term

$$G(s) = \frac{C[\text{Adj}(sI - A)]B}{\det(sI - A)} = \frac{n(s)}{d(s)}. \tag{3.7}$$

The denominator $d(s) = \det(sI - A)$, called the characteristic polynomial, describes the response characteristics of the system. It is calculated as

$$\begin{aligned} d(s) &= |sI - A| \\ &= \begin{vmatrix} s - a_{11} & -a_{12} & \cdots & -a_{1n} \\ -a_{21} & s - a_{22} & \cdots & -a_{2n} \\ \vdots & & \ddots & \vdots \\ -a_{n1} & -a_{n2} & \cdots & s - a_{nn} \end{vmatrix} \\ &= s^n + d_{n-1}s^{n-1} + \cdots + d_1 s + d_0 \\ &= (s + \lambda_1)(s + \lambda_2)\cdots(s + \lambda_n) \end{aligned} \tag{3.8}$$

and solving for $d(s) = 0$ yields the system eigenvalues, λ_i for $i = 1, 2, ..., n$.

Eigenvalues (also called system poles) have real and imaginary parts, and their location in the complex plane dictates the response characteristics of the system. The real part of a pole, $\text{Re}[\lambda_i]$, determines its horizontal position. Poles in the Left Hand Plane (LHP) are stable, poles on the vertical axis produce a bounded oscillation, and poles in the Right Hand Plane (RHP) are unstable. The imaginary part of a pole, $\text{Im}[\lambda_i]$, form complex conjugate pairs above and below the horizontal axis. The greater the magnitude away from the axis, the greater the frequency of oscillation. Figure 3.2 illustrates poles and their respective system response.

3.2.4 Poles and Zeros

The numerator and denominator polynomials of a SISO transfer function determine the poles and zeros of the system. The roots of the numerator $n(s)$ are system zeroes, and the roots of the denominator $d(s)$ (or characteristic equation) are poles of the system. Poles of SISO systems are also the eigenvalues of the state matrix A.

Transfer matrix poles and zeros carry slightly different meaning from their transfer function counterparts. For nearly all s, a MIMO transfer matrix $G(s) = N(s)/d(s)$, has $\text{rank}[G(s)] = \min\{m, q\}$. System zeros are defined such that $N(s)$ drops rank, and system poles are $d(s) = \det(sI - A) = 0$.

The Smith-McMillan Form transforms the transfer matrix $G(s)$ into a useful form for evaluating poles and zeros. Given $\epsilon_i(s)$ and $\delta_i(s)$ are a pair of monic and coprime polynomials, $\epsilon_i(s)$ is a factor of $\epsilon_{i+1}(s)$, and $\delta_i(s)$ is a factor of $\delta_{i-1}(s)$, the Smith-McMillan form of $G(s)$ is described by

$$G_{SM}(s) = \text{diag}\left\{\frac{\epsilon_1(s)}{\delta_1(s)}, \cdots, \frac{\epsilon_r(s)}{\delta_r(s)}, 0, \cdots, 0\right\} \tag{3.9}$$

where $r = \text{rank}(N(s))$.

3.2.5 Controllability

Controllability describes whether the control inputs can influence the states of the system. It is an important tool for system transformations and imple-

menting MIMO state feedback. The controllability matrix $\mathbb{C}$ is given by

$$\mathbb{C} = \left[B, AB, A^2B, \cdots, A^{n-1}B\right] \in \mathbb{R}^{n \times nm} \quad (3.10)$$

where the system (A, B) is controllable, if $\mathbb{C}$ is full rank ($\text{rank}(\mathbb{C}) = n$), which signifies that all rows and columns are linearly independent.

Controllability indexes perform a bookkeeping function while working with MIMO systems. Define column vectors of B as

$$B = [\ b_1,\ b_2,\ \cdots,\ b_m\ ], \quad b_i \in \mathbb{R}^n \quad (3.11)$$

then, select the first n linearly independent columns of $\mathbb{C}$, and reorder them as

$$\left[b_1, Ab_1, \cdots, A^{\mu_1 - 1}b_1, \cdots, b_m, \cdots, A^{\mu_m - 1}b_m\right] \quad (3.12)$$

where $\mu_i,\ i = 1, \ldots, m$ are controllability indexes.

3.2.6 Observability

Observability describes whether initial states can be observed from the system outputs. It is an important tool for state estimation when states are not directly measured. The observability matrix $\mathbb{O}$ is given by

$$\mathbb{O} = \left[C, CA, CA^2, \cdots, CA^{n-1}\right]^T \in \mathbb{R}^{nq \times n} \quad (3.13)$$

where the system (A, C) is observable, if $\mathbb{O}$ is full rank ($\text{rank}(\mathbb{O}) = n$), which signifies that all rows and columns are linearly independent.

Observability indexes serve the same function as controllability indexes. Define row vectors of C as

$$C = [\ c_1,\ c_2,\ \cdots,\ c_q,\ ]^T, \quad c_i^T \in \mathbb{R}^n \quad (3.14)$$

then, select the first n linearly independent rows of $\mathbb{O}$, and reorder as

$$\left[c_1, c_1A, \cdots, c_1A^{\nu_1 - 1}, \cdots, c_q, \cdots, c_qA^{\nu_q - 1}\right]^T \quad (3.15)$$

where $\nu_i,\ i = 1, \ldots, q$ are observability indexes.

3.2.7 Decentralized Control

Developing MIMO control theory is more involved than SISO control theory, so applying SISO design techniques to a MIMO system is attractive. Significant coupling between inputs and outputs means SISO techniques are not appropriate. However, when there is strong correlation between input/output pairs, and little cross coupling, then decentralized control is a valid technique.

The objective is to identify one-to-one mappings between control inputs and system outputs, with little coupling between other inputs and outputs. Strong correlations permit SISO design techniques. For example, for the system $Y(s) = G(s)U(s)$

$$\begin{bmatrix} y_1(s) \\ y_2(s) \end{bmatrix} = \begin{bmatrix} g_{11}(s) & g_{12}(s) \\ g_{21}(s) & g_{22}(s) \end{bmatrix} \begin{bmatrix} u_1(s) \\ u_2(s) \end{bmatrix} \quad (3.16)$$

decentralized control is appropriate when $g_{12}(s)$ and $g_{21}(s)$ are "small", because it indicates that $u_1(s)$ maps to $y_1(s)$ and $u_2(s)$ maps to $y_2(s)$. The Relative Gain Array (RGA) is a matrix Λ that quantifies the subjective term "small". It is described by

$$\Lambda = \begin{bmatrix} \lambda_{11} & \cdots & \lambda_{1m} \\ \vdots & \ddots & \vdots \\ \lambda_{m1} & \cdots & \lambda_{mm} \end{bmatrix} \quad (3.17)$$

where $\lambda_{ij} = [G(0)]_{ij} \left[G^{-1}(0)\right]_{ji}$. Large positive terms on the matrix diagonal indicate strong correlations. Nearly zero values for off-diagonal elements imply little coupling between I/O pairs.

3.3 SISO State Feedback

SISO systems have one control input $u(t)$, any number of states $x(t)$, and one system output $y(t)$. These systems are less complex than MIMO systems, so understanding the behavior of the SISO subsystems is a natural progression toward a more complex analysis.

State feedback control is a well established control technique, straight forward to implement, and allows for arbitrary selection of the desired system response. Although, state feedback only utilizes a state gain K and a reference gain k, this control technique achieves any desired system response (within the physical limits of the control inputs). The simplicity of the controller, and the flexibility to design a prescribed system response, makes this controller an ideal starting point. This section introduces fundamental concepts needed to understand the theory implementing state feedback control.

3.3.1 System Response

Consider a generic system represented by a second order dynamic model, described by

$$G(s) = \frac{\omega_n^2}{s^2 + 2\zeta\omega_n s + \omega_n^2} \tag{3.18}$$

where ζ and ω_n are the desired damping ratio and natural frequency, respectively. The characteristic polynomial is described by

$$d(s) = (s + \sigma + \omega j)(s + \sigma - \omega j) \tag{3.19}$$

where $\mathrm{Re}[\lambda] = \sigma$, and $\mathrm{Im}[\lambda] = \omega$.

When designing a feedback controller, it is more convenient to specify the desired dynamics in terms of settling time t_s and percent overshoot M_p. However, implementing the controller requires knowledge of the system poles. Understanding the relationships between the system dynamics and the pole locations aids the design process.

The settling time t_s dictates σ, the percent overshoot M_p yields ζ, and σ and ζ are used to determine ω and ω_n, from the following relationships

$$\sigma = 4.6/t_s \tag{3.20}$$

$$\zeta = \sqrt{\frac{\ln(M_p)^2}{\pi^2 + \ln(M_p)^2}} \tag{3.21}$$

$$\omega_n = \sigma/\zeta \tag{3.22}$$

$$\omega = \omega_n\sqrt{1 - \zeta^2}. \tag{3.23}$$

Starting with the desired system characteristics (t_s, M_p, ζ), the previous equations are used to find the system poles (σ, ω), needed for control design.

3.3.2 Canonical Transformation

Before developing the state feedback controller, the system must be transformed into a canonical form. This alternative description is equivalent to the original system, but has a special simplified structure used during the controls development.

The plant transfer function $G(s)$ is expressed as rational polynomials of $n(s)$ and $d(s)$, given by

$$G(s) = \frac{n(s)}{d(s)} = \frac{n_{n-1}s^{n-1} + \cdots + n_1 s_1 + n_0}{s^n + d_{n-1}s^{n-1} + \cdots + d_1 s_1 + d_0} \tag{3.24}$$

which forms an alternative state space realization with transformed matrices of the form

$$\begin{aligned} \check{A} &= \begin{bmatrix} 0 & 1 & & 0 \\ \vdots & & \ddots & \\ 0 & 0 & & 1 \\ -d_0 & -d_1 & \cdots & -d_{n-1} \end{bmatrix}, \\ \check{B} &= \begin{bmatrix} 0 \\ \vdots \\ 0 \\ 1 \end{bmatrix}, \quad \check{C}^T = \begin{bmatrix} n_0 \\ n_1 \\ \vdots \\ n_{n-1} \end{bmatrix}. \end{aligned} \tag{3.25}$$

The control input can manipulate every state within the model, so the special structure of this realization guarantees the system (A, B) is controllable. An important point to note, is that similarity transforms do not alter the original system eigenvalues.

The mapping between the controller canonical form and the original representation, is handled by a transformation matrix $T \in \mathbb{R}^{n\times n}$, where

$$\check{x} = Tx, \quad \check{A} = TAT^{-1}, \quad \check{B} = TB, \quad \check{C} = CT^{-1} \tag{3.26}$$

and the the transformed system is described by

$$\dot{\check{x}}(t) = \check{A}\check{x}(t) + \check{B}u(t), \quad y(t) = \check{C}\check{x}(t). \tag{3.27}$$

Transformation matrix T is obtained with the controllability matrix $\mathbb{C}$. Starting with (3.10), compute the last row of the controllability matrix inverse as

$$t_n = [\, 0 \; 0 \; \cdots \; 1 \,]\mathbb{C}^{-1} \tag{3.28}$$

construct the transformation matrix inverse as

$$T^{-1} = \begin{bmatrix} t_n \\ t_n A \\ \vdots \\ t_n A^{n-2} \\ t_n A^{n-1} \end{bmatrix} \tag{3.29}$$

and use the transformation matrix T to obtain the transformed state space realization (3.27). The derivation began with a fully controllable realization, then developed the transformation. Therefore, when starting with the transformation to find the canonical form, the system (A, B) must be controllable.

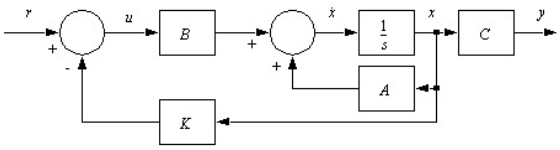

Figure 3.3: State feedback block diagram.

3.3.3 State Feedback Development

The goal of state feedback is to generate a control input $u(t)$ using direct measurements of the states $x(t)$ to arbitrarily place the poles of the closed-loop system in prescribed locations. With a SISO LTI plant described by (3.1), define control law $u(t)$ as

$$u(t) = Kx(t) + kr(t) \tag{3.30}$$

with $r(t) \in \mathbb{R}$ as a reference input, constant state gain vector $K^T \in \mathbb{R}^n$, and constant reference gain $k \in \mathbb{R}$. The block diagram structure of the feedback controller is displayed in Figure 3.3.

Substituting the control law (3.30) into the plant (3.1), produces the following closed-loop system

$$\begin{aligned} \dot{x}(t) &= (A + BK)\, x(t) + Bkr(t) \\ &= \bar{A}x(t) + \bar{B}r(t) \end{aligned} \tag{3.31}$$

where

$$\bar{A} = A + BK, \quad \bar{B} = Bk, \tag{3.32}$$

describes the desired closed-loop system response. The design task is to find K such that the eigenvalues of the closed-loop system $\lambda_i(A + BK)$ match the eigenvalues of some desired characteristic polynomial $\alpha(s)$, and to find k so the output $y(t)$ tracks a constant reference set point $r(t) = r$. The state gain K determines transient response, the reference gain k dictates the steady state response, and the resultant system follows the matching condition (3.32).

When the system is expressed in controller canonical form $(\check{A}, \check{B}, \check{C})$, the closed-loop state matrix $\bar{A}$ is described by

$$\begin{aligned} \bar{A} &= \check{A} + \check{B}\check{K} \\ &= \begin{bmatrix} 0 & 1 & & 0 \\ \vdots & & \ddots & \\ 0 & 0 & & 1 \\ -d_0+k_0 & -d_1+k_1 & \cdots & -d_{n-1}+k_{n-1} \end{bmatrix} \end{aligned} \tag{3.33}$$

and the closed-loop characteristic polynomial is

$$\begin{aligned} \bar{d}(s) = s^n &+ (d_{n-1} - k_{n-1})s^{n-1} \\ &+ \cdots + (d_1 - k_1)s + (d_0 - k_0). \end{aligned} \tag{3.34}$$

This simplified structure allows for direct matching between coefficients in the closed-loop characteristic polynomial $\bar{d}(s)$, and coefficients in the desired characteristic polynomial $\alpha(s)$

$$\alpha(s) = s^n + \alpha_{n-1}s^{n-1} + \cdots + \alpha_1 s + \alpha_0. \tag{3.35}$$

Select the transformed feedback gain $\check{K}$ as

$$\check{K} = [\ d_0 - \alpha_0,\ \ d_1 - \alpha_1,\ \ \cdots,\ \ d_{n-1} - \alpha_{n-1}\ ] \tag{3.36}$$

which places the closed-loop poles of $\bar{A}$ in the desired locations. Because $\check{K}$ is designed for the canonical form, it must be transformed with $K = \check{K}T$ to work for the original system.

The final step determines the reference gain k which achieves steady-state set point tracking. The steady-state of a system is described by the equilibrium point once the state derivatives settle to zero. The closed-loop state equation is expressed as

$$\begin{aligned} 0 &= \bar{A}x_e + \bar{B}r \\ x_e &= -\bar{A}^{-1}\bar{B}r \end{aligned} \tag{3.37}$$

and the output equation becomes

$$y_e = Cx_e = -C\bar{A}^{-1}\bar{B}r. \tag{3.38}$$

For y_e to track r, we need $-C\bar{A}^{-1}\bar{B} = 1$, which is equivalent to

$$-C(A + BK)^{-1}Bk = 1. \tag{3.39}$$

Solving for the reference gain k yields

$$\begin{aligned} k &= -[C(A + BK)^{-1}B]^{-1} \\ &= -[C\bar{A}^{-1}B]^{-1} \end{aligned} \tag{3.40}$$

which forces the steady state system output y_e to track the reference signal r.

3.4 MIMO State Feedback

MIMO systems have multiple control inputs $u(t)$ and multiple system outputs $y(t)$. The theory for MIMO controllers is more involved than SISO controllers, but MIMO control accounts for coupling between inputs and outputs, which offers a more unified response. Furthermore, most adaptive control and system identification theory is based on MIMO systems, so this controller is the next logical progression.

State feedback for MIMO systems maintains the same structure as SISO state feedback. It still only utilizes two gains, and achieves any desired system response. The two gains become matrices K_x and K_r, accounting for additional inputs and outputs.

Although the control structure is identical, obtaining the gain matrices requires some additional derivations. This section presents the theory for developing MIMO state feedback, selecting a desired system response, and obtaining the gain matrices.

3.4.1 Theory Overview

Consider a MIMO LTI system described by (3.1), where system matrices are known and constant, and all states are available for measurement.

Define the control law as

$$u(t) = K_x x(t) + K_r r(t) \tag{3.41}$$

with control input $u(t) \in \mathbb{R}^m$, reference signal $r(t) \in \mathbb{R}^m$, state gain matrix $K_x \in \mathbb{R}^{m\times n}$ and reference gain matrix $K_r \in \mathbb{R}^{m\times m}$. Substitute (3.41) into (3.1) to obtain the closed-loop system

$$\begin{aligned} \dot{x}(t) &= (A + BK_x)x(t) + BK_r r(t) \\ &= \bar{A}x(t) + \bar{B}r(t) \end{aligned} \tag{3.42}$$

where $\bar{A} \in \mathbb{R}^{n\times n}$ and $\bar{B} \in \mathbb{R}^{n\times m}$ are the reference state and input matrices which achieve the desired closed-loop system response. These relationships form the following matching conditions

$$\bar{A} = A + BK_x, \quad \bar{B} = BK_r \tag{3.43}$$

which mirrors the SISO relationships in (3.32).

The design task is to place the closed-loop eigenvalues, $\lambda_i(\bar{A}) = \lambda_i(A+BK_x) = s_i$ at some prescribed locations, and to have the output signal $y(t)$ track a constant reference set point, $r(t) = r$. To implement this control architecture, the system (A, B) must be controllable and $\text{rank}(B) = m$.

3.4.2 Canonical Transformations

Identical to the SISO development, this process begins by putting the system into a canonical form through a transformation $T \in \mathbb{R}^{n\times n}$. The transformed arrays have the same form as (3.26) and the transformed system is still described by (3.27).

With (A, B) controllable, a transformation T exists for the MIMO system, such that

$$\bar{A} = A_0 + B_0 U T^{-1}, \quad \bar{B} = B_0 R \tag{3.44}$$

with

$$\begin{aligned} A_0 &= \text{diag}\{\ A_{01},\ A_{02},\ \cdots,\ A_{0m}\ \} \\ B_0 &= \text{diag}\{\ B_{01},\ B_{02},\ \cdots,\ B_{0m}\ \} \end{aligned} \tag{3.45}$$

where A_{0i} is given by

$$A_{0i} = \begin{bmatrix} 0 & 1 & 0 & \cdots & 0 \\ 0 & 0 & 1 & & 0 \\ \vdots & & & \ddots & \vdots \\ & & & & 1 \\ 0 & \cdots & & 0 & 0 \end{bmatrix} \in \mathbb{R}^{\mu_i\times\mu_i} \tag{3.46}$$

and B_{0i} is described by

$$B_{0i} = [\ 0\ 0\ \cdots\ 0\ 1\ ]^T \in \mathbb{R}^{\mu_i} \tag{3.47}$$

for $i = 1, \ldots, m$, where μ_i are controllability indexes.

3.4.3 Matrix Formulation

Parallel to the SISO derivations, the MIMO theory utilizes a modified controllability matrix as an intermediate step toward finding the gain matrices. Form matrix M^{-1} as

$$b_1, Ab_1, \cdots, A^{\mu_1-1}b_1, \cdots, b_m, \cdots, A^{\mu_m-1}b_m \tag{3.48}$$

and define row vectors as

$$\begin{aligned} M &= [\ M_1,\ M_2,\ \cdots,\ M_n\ ]^T \in \mathbb{R}^{n\times n}, \\ T &= [\ T_1,\ T_2,\ \cdots,\ T_m\ ]^T \in \mathbb{R}^{n\times n}. \end{aligned} \tag{3.49}$$

Matrix M determines the sub matrices of T with

$$T_i = \begin{bmatrix} M_{\mu_1+\cdots+\mu_i} \\ M_{\mu_1+\cdots+\mu_i}A \\ \vdots \\ M_{\mu_1+\cdots+\mu_i}A^{\mu_i-1} \end{bmatrix} \in \mathbb{R}^{\mu_i \times n} \tag{3.50}$$

and populates matrices U and R by

$$U = \begin{bmatrix} M_{\mu_1}A^{\mu_1} \\ M_{\mu_1+\mu_2}A^{\mu_2} \\ \vdots \\ M_{\mu_1+\cdots+\mu_m}A^{\mu_m} \end{bmatrix} \in \mathbb{R}^{m \times n}, \tag{3.51}$$

$$R = \begin{bmatrix} M_{\mu_1}A^{\mu_1-1}B \\ M_{\mu_1+\mu_2}A^{\mu_2-1}B \\ \vdots \\ M_{\mu_1+\cdots+\mu_m}A^{\mu_m-1}B \end{bmatrix} \in \mathbb{R}^{m \times m}. \tag{3.52}$$

This yields all the matrices needed to put the system into the canonical form.

3.4.4 Closed-Loop Response

The closed-loop response is dictated by $\bar{A}$ where

$$\begin{aligned} \bar{d}(s) &= \det(sI - \bar{A}) \\ &= (s - s_1)\cdots(s - s_n) \\ &= s^n + d_{n-1}s^{n-1} + \cdots + d_1 s + d_0 \end{aligned} \tag{3.53}$$

and the desired system response is described by (3.35). The closed-loop state matrix $\bar{A}$ indirectly determines the state feedback gain $\check{K}_x$, defined as

$$\check{K}_x = -R^{-1}UT^{-1} + R^{-1}P \tag{3.54}$$

where P is given by

$$P = \begin{bmatrix} e_{\mu_1+1} \\ e_{\mu_1+\mu_2+1} \\ \vdots \\ e_{\mu_1+\cdots+\mu_{m-1}+1} \\ [\, -\alpha_0,\ \alpha_1,\ \cdots,\ -\alpha_{n-1}\,] \end{bmatrix} \in \mathbb{R}^{m \times n} \tag{3.55}$$

with e_j being the j^{th} row of an $n \times n$ identity matrix. This canonical form leads to

$$\begin{aligned} \bar{A} &= A_0 + B_0 P \\ &= A_0 + B_0(UT^{-1} + R\bar{K}_x) \end{aligned} \tag{3.56}$$

so the closed-loop eigenvalues are given by

$$\lambda_i(\bar{A}) = \lambda_i(\check{A} + \check{B}\check{K}_x) = \lambda_i(A + BK_x) \tag{3.57}$$

where $K_x = \check{K}_x T$, which places the system poles in the desired locations.

The final step calculates the reference gain K_r, so the system output $y(t)$ tracks a constant reference set point $r(t) = r$. Steady-state equilibrium is dictated by

$$y_e = -C\left(A + BK_x\right)^{-1} BK_r r \tag{3.58}$$

so, define the reference gain as

$$\begin{aligned} K_r &= -\left[C\left(A + BK_x\right)^{-1} B\right]^{-1} \\ &= -\ C\bar{A}^{-1}B\ ^{-1} \end{aligned} \tag{3.59}$$

to achieve $y(t) = r$.

3.5 State Estimation

Up to this point, state feedback theory assumes all states $x(t)$ are available for measurement. In practice, many systems have states that are not directly measured, so full state feedback cannot be directly implemented. Later sections will show that the CSR vehicle is one such system, because the location of the satellites is not precisely known. GPS provides sufficient accuracy for waypoint navigation, but does not have enough fidelity to provide the satellite location with respect to the central hub.

State estimation is a powerful control technique that can overcome these short comings. It is designed to make use of all the available measurements and then estimate states that are not measured. The theory is a direct extension of state feedback, so it builds heavily upon the previous foundation. This section introduces the general theory for full state estimation, shows the error reduction process, and expands the theory to a reduced order estimator which only estimates the unknown states.

3.5.1 Theory Overview

State estimation uses information from $y(t)$, $u(t)$ and (A, B, C) to find the estimate $\hat{x}(t)$ of $x(t)$, such that $\lim_{t\to\infty}(x(t) - \hat{x}(t)) = 0$, exponentially. The MIMO LTI system is still described by (3.1), but now the control law becomes

$$u(t) = K_x\hat{x}(t) + K_r r(t) \tag{3.60}$$

which uses the state estimate $\hat{x}(t)$ to calculate the control input $u(t)$. Substituting (3.60) into (3.1) forms the closed-loop system as

$$\dot{x}(t) = Ax(t) + BK_x\hat{x}(t) + BK_r r(t). \tag{3.61}$$

Now, define the estimation system as

$$\dot{\hat{x}}(t) = A\hat{x}(t) + Bu(t) + K_e\left(y(t) - C\hat{x}(t)\right) \tag{3.62}$$

with initial condition $\hat{x}(0) = \hat{x}_0$, and an estimation gain of $K_e \in \mathbb{R}^{n\times q}$.

The estimation system (3.62) has a very specific form. Notice $\hat{y}(t) = C\hat{x}(t)$ is the estimate of $y(t) = Cx(t)$. When the estimate $\hat{x}(t)$ equals the true state value $x(t)$, then $\hat{y}(t) = y(t)$, the final term becomes zero, and K_e has no influence. Similarly, when the estimate has no error, the other terms in (3.62) reduce to (3.1).

3.5.2 Error Reduction

The goal is to select K_e so the state estimate $\hat{x}(t)$ tracks the actual state $x(t)$, and maintains stability within the system. Define the estimation error as

$$\tilde{x}(t) = x(t) - \hat{x}(t) \tag{3.63}$$

and solve for its derivative

$$\begin{aligned}\dot{\tilde{x}}(t) &= \dot{x}(t) - \dot{\hat{x}}(t)\\ &= [Ax+Bu]-[A\hat{x}+Bu+K_e\left(y-C\hat{x}\right)]\\ &= Ax - A\hat{x} + K_e\left(y - C(x-\tilde{x})\right)\\ &= A(x-\hat{x}) + K_e\left(y - Cx + C\tilde{x}\right)\\ &= \left(A + K_eC\right)\tilde{x}.\end{aligned} \tag{3.64}$$

The estimation system dynamics are described by $\lambda_i(A+K_eC)$, so the task is to select K_e to achieve a desired response (stable, fast, etc). Notice the similarity between state estimation $(A+K_eC)$ and state feedback $(A+BK_x)$. The duality between controllability and observability, means selecting K_e follows the same process as selecting K_x. With (A, C) observable, it is known that (A^T, C^T) controllable. The estimation structure is identical to state feedback formulation, so the previous process finding the state feedback gain (K_x from A and B) can be used to find the state estimator gain (K_e from A^T and C^T).

3.5.3 Reduced Order Estimator

All feedback controlled systems have some states available for measurement, so full order estimators have redundancy estimating states that are directly measured. A reduced order estimator is more efficient because it uses the direct measurements and only estimates the unknown states.

Apply a transformation described by (3.26) and (3.27) where the transformation matrix T is selected to achieve a special form of $\check{C}$, such that

$$\check{C} = [\ I_q,\ 0_{q\times(n-q)}\ ] \in \mathbb{R}^{q\times n} \tag{3.65}$$

which leads to $\check{x} = [\ x_m^T\ x_e^T\ ]^T$ where $x_m \in \mathbb{R}^q$ are measured states and $x_e \in \mathbb{R}^{n-q}$ are estimated states. The measured states directly map to the system outputs, so $y = x_m$. The expanded transformed system is described by

$$\begin{aligned}\dot{\check{x}}(t) &= \check{A}\check{x}(t) + \check{B}u(t)\\ \begin{matrix}\dot{x}_m\\ \dot{x}_e\end{matrix} &= \begin{matrix}A_{mm} & A_{me}\\ A_{em} & A_{ee}\end{matrix}\begin{matrix}x_m\\ x_e\end{matrix} + \begin{matrix}B_m\\ B_e\end{matrix}u\end{aligned} \tag{3.66}$$

where $(\ A_{ee},\ A_{me}\ )$ must be observable.

The reduced order estimator has a special structure of $\check{C}$, so the previous estimation system (3.62) cannot be used. Notice that $\check{y} = \check{C}\check{x} = x_m = y$; therefore, $y - \check{C}\check{x} = 0$, so an estimator gain has no influence on this system. To alleviate this concern, select a substitution variable $w = x_e - K_o x_m$ where $K_o \in \mathbb{R}^{(n-q)\times q}$, and $w \in \mathbb{R}^{n-q}$. Now the estimated states are determined from the relationship $x_e = w + K_o x_m$.

The substitution variable dynamics are given by

$$\begin{aligned}\dot{w} &= \dot{x}_e - K_o\dot{x}_m \\ &= [A_{em}x_m + A_{ee}x_e + B_e u] \\ &\quad -K_o\left[A_{mm}x_m + A_{me}x_e + B_m u\right] \\ &= [A_{em}y + A_{ee}(w + K_o y) + B_e u] \\ &\quad -K_o\left[A_{mm}y + A_{me}(w + K_o y) + B_m u\right] \\ &= (A_{ee} - K_o A_{me})w + (B_e - K_o B_m)\, u \\ &\quad +((A_{ee} - K_o A_{me})K_o + A_{em} - K_o A_{mm})y\end{aligned} \tag{3.67}$$

with $w(0) = w_0$. Define the estimation system as

$$\begin{aligned}\dot{\hat{x}}_e &= A_{em}x_m + A_{ee}\hat{x}_e + B_e u \\ &\quad +K_o\left[\dot{x}_m - (A_{mm}x_m + A_{me}\hat{x}_e + B_m u)\right]\end{aligned} \tag{3.68}$$

where $\hat{x}_e$ is the current value of the estimated state x_e. Just like (3.62), this estimation system has a very special structure. Notice that when the estimate $\hat{x}_e$ equals the true value x_e, the last term drops to zero and K_o has no influence on the system. Similarly, when the estimate has zero error, the other terms in (3.68) become the bottom row of (3.66).

The estimation error is described by

$$\tilde{x}_e(t) = x_e(t) - \hat{x}_e(t) \tag{3.69}$$

and the estimation error dynamics are obtained by taking the derivative of (3.69), and substituting in both rows of (3.66) and (3.68). This yields

$$\begin{aligned}\dot{\tilde{x}}_e(t) &= \dot{x}_e(t) - \dot{\hat{x}}_e(t) \\ &= (A_{ee} - K_o A_{me})\,\tilde{x}_e(t)\end{aligned} \tag{3.70}$$

which also has the same structure as the full state feedback and full state estimator designs. When (A_{ee}, A_{me}) observable, finding the value of K_o from A_{ee}^T and A_{me}^T follows the same procedure as selecting K_x given (A, B), or K_e given (A^T, C^T).

3.6 Adaptive Control

Thus far, all the controllers assume perfect knowledge of the plant. In reality, the dynamics of the CSR system are largely unknown due to its novel design. Modeling provides a good starting point, but there is very little research and no wind tunnel data to compare against the simulations. The primary form of model validation will come from collected flight data, meaning the prototypes must fly based on imperfect models.

Adaptive control serves two main purposes for the CSR system. First, certain adaptive control architectures perform system identification, which uses measured signals to determine system characteristics. Values like polynomial coefficients and elements of state space matrices, can validate computer models and aid with future prototype designs. Second, adaptive controllers are deigned to adjust controller parameters in real time, so the controller starts with an imperfect model, and adapts to the true physical plant. Early flights, with little aerodynamic validation, will not have high-fidelity models. Adaptive control mitigates some of this risk by adapting to the imperfect model.

Running system identification on the first set of prototypes is the highest priority, so this section focuses on adaptive control which performs parameter estimation. It also presents a stability analysis, and the conditions that must be present for the parameters to converge to their true values.

3.6.1 Parameter Estimation

The purpose of parameter estimation is to obtain unknown values of the plant. This theory builds upon state feedback control, and will yield the values of the elements within the A and B matrices. These values represent the partial derivatives of the system, so their physical significance is especially useful developing prototypes and validating simulations.

Let $\hat{A}$ and $\hat{B}$ be the estimates of A and B, respectively. Substitute the matrix estimates into the matching condition (3.43), solve for $\hat{A}$ and $\hat{B}$ as

$$\hat{A} = \bar{A} - \bar{B}K_r^{-1}K_x, \quad \hat{B} = \bar{B}K_r^{-1} \tag{3.71}$$

and solve for the control law (3.41) in terms of the reference signal

$$r(t) = -K_r^{-1}K_x x(t) + K_r^{-1}u(t). \tag{3.72}$$

The reference system

$$\dot{\hat{x}}(t) = \bar{A}\hat{x}(t)\bar{B}r(t) \tag{3.73}$$

is identical to (3.42) except the actual states are replaced by reference states $\hat{x}(t)$. Eliminate the state

and reference gains by substituting the reference signal (3.72) into reference system (3.73), so that

$$\begin{aligned}\dot{\hat{x}}(t) &= \bar{A}\hat{x}(t)+\bar{B}[-K_r^{-1}K_x x(t) + K_r^{-1}u(t)] \\ &= \bar{A}\hat{x}(t) + (\bar{A}x(t) - \bar{A}x(t)) \\ &\quad -\bar{B}K_r^{-1}K_x x(t) + \bar{B}K_r^{-1}u(t) \\ &= \bar{A}\hat{x}(t) + (\hat{A} - \bar{A})x(t) + \hat{B}u(t).\end{aligned} \tag{3.74}$$

When $\hat{A} = A$, $\hat{B} = B$, and $\hat{x} = x$ the system reduces down to (3.1). This suggests the adaptive laws should update time varying estimates $\hat{A}(t)$ and $\hat{B}(t)$.

Designing the adaptive observer requires that $\bar{A}$ is stable (all eigenvalues in $\mathrm{Re}[s] < 0$), and the control input $u(t)$ and state $x(t)$ are bounded. State feedback ensures these conditions are satisfied. The closed-loop desired characteristics are reflected in $\bar{A}$, which is designed to be stable. The boundedness of the control input $u(t)$ and the state $x(t)$ were demonstrated in the MIMO state feedback development.

3.6.2 Estimation Errors

Define the parameter estimate errors as

$$\tilde{A}(t) = \hat{A}(t) - A, \quad \tilde{B}(t) = \hat{B}(t) - B \tag{3.75}$$

with the following column vectors

$$\begin{aligned}\tilde{A}(t) &= [\ \tilde{a}_1(t), \cdots, \tilde{a}_n(t)\ ], \\ \tilde{B}(t) &= [\ \tilde{b}_1(t), \cdots, \tilde{b}_m(t)\ ].\end{aligned} \tag{3.76}$$

Because A and B are constant, the parameter estimate error derivatives are given by $\dot{\tilde{A}}(t) = \dot{\hat{A}}(t)$ and $\dot{\tilde{B}}(t) = \dot{\hat{B}}(t)$. The state estimate error is defined as

$$\tilde{x}(t) = \hat{x}(t) - x(t) \tag{3.77}$$

with dynamics described by

$$\begin{aligned}\dot{\tilde{x}}(t) &= \dot{\hat{x}}(t) - \dot{x}(t) \\ &= [\bar{A}\hat{x}(t) + (\hat{A}(t) - \bar{A})x(t) + \hat{B}(t)u(t)] \\ &\quad -[Ax(t) + Bu(t)] \\ &= \bar{A}\tilde{x}(t) + \tilde{A}(t)x(t) + \tilde{B}(t)u(t).\end{aligned} \tag{3.78}$$

The estimate errors form the closed-loop state vector

$$\epsilon(t) = \ \tilde{x}^T,\ \tilde{a}_1^T, \cdots, \tilde{a}_n^T,\ \tilde{b}_1^T, \cdots, \tilde{b}_m^T\ ^T \in \mathbb{R}^{n+m+1} \tag{3.79}$$

which is used for stability analysis.

3.6.3 Adaptive Laws

Select an arbitrary square matrix $Q \in \mathbb{R}^{n\times n}$ where $Q = Q^T > 0$. Find $P \in \mathbb{R}^{n\times n}$, which is the solution to the Lyapunov equation $P\bar{A} + \bar{A}^T P = -Q$, where $P = P^T > 0$. Adaptive laws for $\hat{A}(t)$ and $\hat{B}(t)$ are

$$\begin{aligned}\dot{\tilde{A}}(t) = \dot{\hat{A}}(t) &= -\Gamma_A P\tilde{x}(t)x^T(t) \\ \dot{\tilde{B}}(t) = \dot{\hat{B}}(t) &= -\Gamma_B P\tilde{x}(t)u^T(t)\end{aligned} \tag{3.80}$$

where $\Gamma_A, \Gamma_B \in \mathbb{R}^{n\times n}$ are arbitrary constant gain matrices, such that $\Gamma_A = \Gamma_A^T > 0$ and $\Gamma_B = \Gamma_B^T > 0$.

3.6.4 Stability Analysis

Define a positive definite function V in terms of the estimation errors $\epsilon(t)$ ((t) is omitted for space)

$$V(\epsilon) = \tilde{x}^T P\tilde{x} + \Sigma_A + \Sigma_B \tag{3.81}$$

where

$$\Sigma_A = \sum_{i=1}^{n} \tilde{a}_i^T \Gamma_A^{-1} \tilde{a}_i = \mathrm{tr}\ \ \tilde{A}^T \Gamma_A^{-1} \tilde{A} \tag{3.82}$$

and

$$\Sigma_B = \sum_{j=1}^{m} \tilde{b}_j^T \Gamma_B^{-1} \tilde{b}_j = \mathrm{tr}\ \ \tilde{B}^T \Gamma_B^{-1} \tilde{B} \tag{3.83}$$

and solve for the derivative of V as

$$\dot{V} = 2\tilde{x}^T P\dot{\tilde{x}} + 2\mathrm{tr}\ \ \tilde{A}^T\Gamma_A^{-1}\dot{\tilde{A}}\ \ + 2\mathrm{tr}\ \ \tilde{B}^T\Gamma_B^{-1}\dot{\tilde{B}}\ . \tag{3.84}$$

Substituting (3.78) into the first term of (3.84) yields

$$\begin{aligned}2\tilde{x}^T P\dot{\tilde{x}} &= 2\tilde{x}^T P\ \ \bar{A}\tilde{x} + \tilde{A}x + \tilde{B}u \\ &= 2\tilde{x}^T P\bar{A}\tilde{x} + 2\tilde{x}^T P\tilde{A}x + 2\tilde{x}^T P\tilde{B}u\end{aligned} \tag{3.85}$$

which yields three new terms. The first term is

$$2\tilde{x}^T P\bar{A}\tilde{x} = -\tilde{x}^T Q\tilde{x} \tag{3.86}$$

the second term yields

$$\begin{aligned}2\tilde{x}^T P\tilde{A}x &= 2\mathrm{tr}\ \ \tilde{x}^T P\tilde{A}x \\ &= 2\mathrm{tr}\ \ x\tilde{x}^T P\tilde{A} \\ &= 2\mathrm{tr}\ \ \tilde{A}^T P\tilde{x}x^T \\ &= 2\mathrm{tr}\ \ \tilde{A}^T\Gamma_A^{-1}\Gamma_A P\tilde{x}x^T\end{aligned} \tag{3.87}$$

and the third term follows the same derivation

$$2\tilde{x}^T P\tilde{B}u = 2\text{tr}\ \ \tilde{B}^T\Gamma_B^{-1}\Gamma_B P\tilde{x}u^T \quad . \tag{3.88}$$

Substitute all the manipulated terms back into $\dot{V}$

$$\begin{aligned}\dot{V} = &-\tilde{x}^T Q\tilde{x} \\ &+2\text{tr}\,\tilde{A}^T\Gamma_A^{-1}(\Gamma_A P\tilde{x}x^T) + 2\text{tr}\,\tilde{A}^T\Gamma_A^{-1}(\dot{\tilde{A}}) \\ &+2\text{tr}\,\tilde{B}^T\Gamma_B^{-1}(\Gamma_B P\tilde{x}u^T) + 2\text{tr}\,\tilde{B}^T\Gamma_B^{-1}(\dot{\tilde{B}})\end{aligned} \tag{3.89}$$

where the adaptive laws (3.80), cancel all of the trace terms leaving

$$\dot{V} = -\tilde{x}^T Q\tilde{x} \tag{3.90}$$

which shows that $\dot{V}$ is negative semi-definite. This means the equilibrium state $\epsilon = 0$ of the closed-loop system is uniformly stable, and the solution $\epsilon(t)$ is uniformly bounded. It also proves that $\tilde{A}(t)$, $\tilde{B}(t)$, and $\dot{\tilde{x}}(t)$ are all bounded. Finally, (3.90) implies that $\tilde{x}(t) \in L^2$, so $\lim_{t\to\infty}\tilde{x}(t) = 0$.

3.6.5 Parameter Convergence

The stability analysis shows that all the closed-loop signals are bounded; however, Barbălat Lemma does not ensure $\lim_{t\to\infty}\tilde{A}(t) = 0$ and $\lim_{t\to\infty}\tilde{B}(t) = 0$. Ensuring the parameter estimates converge to their true values requires persistent excitation to make the signal "rich" enough.

Multisine signal injection accomplishes this task. The process applies sinusoidal control inputs to the system. This excites the system dynamics, so the adaptation continues with new measurements.

The control input is persistently exciting if it contains at least $f = n + m + 1$ frequencies. A constant control input contains a single frequency at zero. Sinusoidal inputs with frequency ω and amplitude σ, contribute two frequencies at $\pm\omega$. Therefore, the minimum number of sine inputs f_0 is the smallest integer that satisfies $f_0 \geq (n + m + 1)/2$.

Specify the control input as

$$u(t) = \sum_{i=1}^{f_0} \sigma_i \sin(\omega_i t) \tag{3.91}$$

where $\sigma_i \neq 0$, and ω_i are all distinct, for $i = 1, 2, \cdots, f_0$. Once the persistently exciting signal is introduced into the system, $\lim_{t\to\infty}\tilde{A}(t) = 0$ and $\lim_{t\to\infty}\tilde{B}(t) = 0$, exponentially.

3.6.6 Future Work

Collecting data for the first prototype vehicle is the highest priority for the hardware development plan. Thus, the first adaptive control architecture focused on parameter estimation and system identification. The next steps with adaptive control will develop controllers that adapt to uncertainties within the dynamic model. Two architectures, model reference adaptive control (MRAC) and L_1 adaptive control, will be developed, simulated, and implemented on the prototype vehicles.

Model Reference Adaptive Control (MRAC)

When it comes to adaptive control, MRAC is the *de facto* standard. It is the most widely researched and utilized adaptive control architecture available in the literature. An established reference model contains the desired system dynamics, then the controller feedback gains adapt so the physical system matches the desired model. The type of MRAC presented in Figure 3.4, yields state estimates. Thus, the CSR system can use this architecture even though relative positions of the satellites are not measured. Despite its widespread use, MRAC has some notable limitations. High adaptation gains are desirable to accelerate the adaptation process; however, this leads to high frequency control inputs which may exceed the actuator bandwidth. Selecting appropriate gains is something of a black art, where improper selection may lead to robustness issues. Finally, MRAC is a nonlinear controller, so it is not scalable for alternative prototypes and full scale vehicles.

L1 Adaptive Control

Despite being a relatively new adaptive control architecture, L_1 adaptive control has received a great deal of attention in recent years, because it alleviates many of the issues found with traditional MRAC. Similar to MRAC, L_1 defines a reference model, and the controller adapts so the closed-loop response matches the reference model. The key difference, illustrated in Figure 3.5, is L_1 adaptive control introduces a low pass filter $C(s)$ prior to the control input $u(t)$. This keeps the actuators within appropriate bandwidths, which eliminates the high frequency

control inputs. Because of this feature, the architecture demonstrates guaranteed robustness. Therefore, the adaptation gain can be set as high as possible, which induces fast estimation, and is only limited by the hardware processing speed within the controller. Finally, it shifts emphasis away from a nonlinear stability analysis, and towards the design of a linear filter. This allows for traditional linear design analysis, and ensures inputs and outputs scale uniformly to specified reference signals.

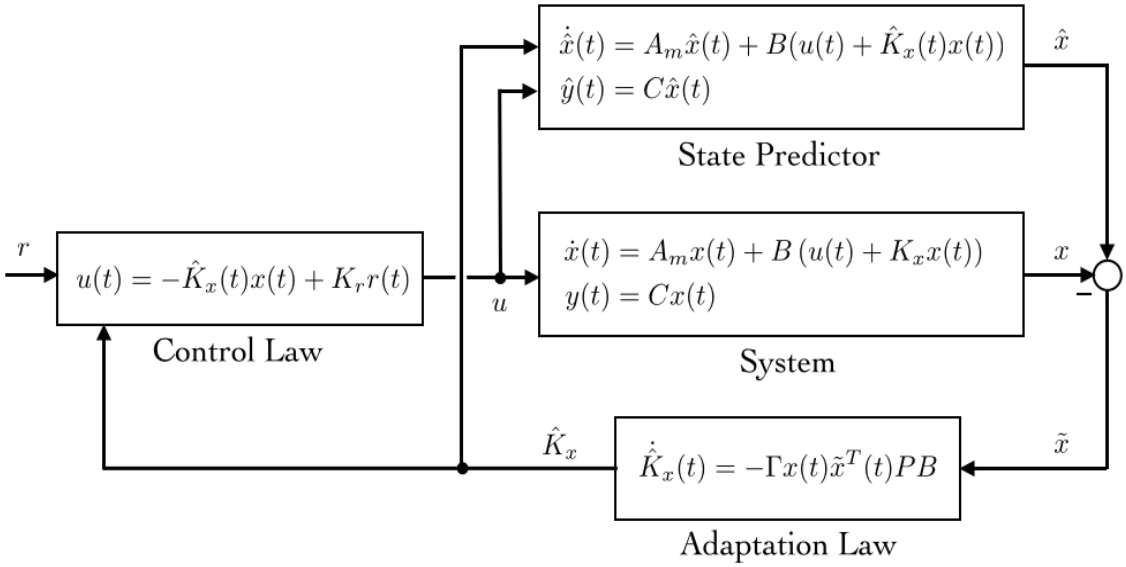

Figure 3.4: Block diagram of MRAC control.

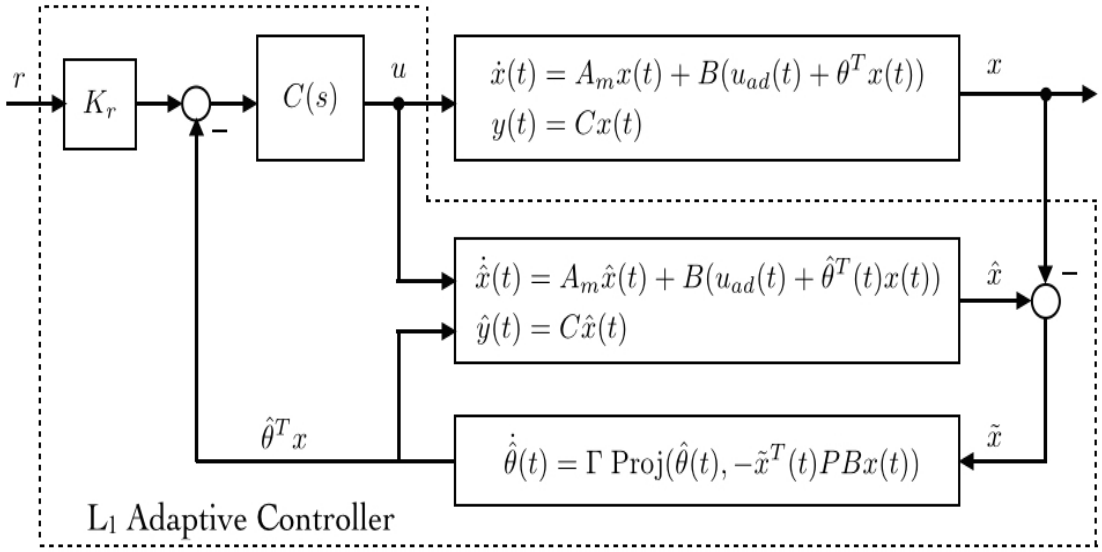

Figure 3.5: Block diagram of L_1 control.

Chapter 4

System Analysis and Simulations

Simulations are the primary means of gaining confidence in the system dynamics and controller effectiveness prior to flying an untested prototype vehicle. Each round of prototype testing exhibits a natural progression from simple tasks to more complex maneuvers, so the simulations follow a similar process which mirrors the prototype development effort.

Motivation

Very little research exists to aid in the CSR design. Whereas, new aircraft designs can utilize existing wind tunnel data and control derivatives from other similar aircraft, there is no existing model or research to start the CSR development. The dynamics are highly nonlinear, so paper analysis and hand derivations are not sufficient enough for the first prototypes. Early controller development will heavily utilize simulations to gain confidence in the vehicle dynamics before flying a physical prototype.

The first research focuses on the RTP flight model, because this system is used early on for data collection, avionics platform development, and system identification. The CSR system does not have any direct control over the central hub. Stabilizing and maneuvering the hub, as well as the rest of the vehicle, is accomplished indirectly through tension in the tethers. These forces are manipulated by the control inputs applied to each individual satellite vehicle, which is exhibited in a RTP flight model. Therefore, successfully implementing the RTP controller is the first step towards controlling the full CSR vehicle, and this controller will be directly applied towards inner loop stabilization.

Objectives

With an established set of control theory, the next objective is to put that theory into practice. The task is to analyze the first prototype vehicle, and identify the linear model to develop the controller. Several types of prototypes will be developed throughout the research process, but this first analysis focuses exclusively on the control line aircraft, because it is the first prototype vehicle. These vehicles are ready for flight out of the box, which is an ideal platform to test the avionics package and flight controls before moving on to a much more expensive custom aircraft with unknown flight characteristics.

The CSR control system is composed of inner loop control for stabilization, and outer loop control for navigation. The first set of simulations address inner loop control which is built upon the RTP satellite configuration. The first objective is to assemble the SISO subsystems that corresponds to the three control inputs available on the satellite vehicles: throttle, elevator, and rudder. The structure of the system and the desired response is defined for each control input, and a control law is developed for each input-output pair. Once SISO control is established, the next objective implements MIMO state

feedback on the RTP model, which achieves the inner loop controller used on the CSR vehicle.

Outline

While the previous chapter developed the controller theory, this chapter applies that theory to the CSR system. It uses the analysis techniques on several CSR models, and showcases the controller performance by simulating the nonlinear system.

Section 4.1 performs the *System Analysis* on the CSR vehicle. It describes the model parameters used during the simulations, the three control inputs for each satellite, the state space signals, and the relative gain array for a decentralized control technique.

Section 4.2 applies *SISO State Feedback* to the round the pole system. It defines the desired system response for each input/output channel, and then calculates the feedback gains needed to achieve that dynamic response.

Section 4.3 expands the analysis to *MIMO State Feedback*. It reviews the characteristics of the MIMO system, reviews controllability and observability, and derives the feedback gains for the controller.

Section 4.4 presents *Simulations* for both SISO and MIMO models. All the controllers are applied to the nonlinear CSR model, and several scenarios are illustrated which demonstrate that the controllers successfully achieve the desired system performance.

4.1 System Analysis

Several different prototypes are developed for this research. The scaled prototype is a carbon fiber Kevlar construction, mono-wing design, that more closely resembles the full scale CSR system. This prototype has many unknown dynamics and aerodynamics, so a commercial off the shelf (COTS) control line airplane serves as the first prototype development, because it is designed to fly out of the box.

4.1.1 Model Description

Before moving to a free flight test, the RTP model will serve as a stepping stone. This tests new avionics hardware and control algorithms before implementing them in a more difficult environment. This section describes the properties of the hub, tether, and satellite that generate the simulation model.

Hub

For the RTP system the central hub is constrained to a fixed pole but is free to rotate about the vertical axis. The bearing is lubricated, but still provides some nominal amount of rotational drag. A magnetometer mounted on the hub rotates with the system, and provides heading measurements.

Tether

The full scale system uses space grade Spectra line for the tether, which is extremely light and strong. The COTS control line airplane prototype comes with a thin steel cable as the tether. The tether is 30 feet (9.14 m) long, with a 3/64 inch (1.19 mm) diameter, and is modeled with a density of 500 lb/ft^3 (8,000 kg/m^3). The tether is completely flexible, but is modeled as 20 rigid body elements.

Satellite

The control line airplane resembles a conventional aircraft with symmetrical wing and horizontal stabilizer, and an upper vertical stabilizer. The plane uses electric power with LiPo batteries, a brushless motor, and a single fixed pitch propeller. The aircraft comes with pitch control already installed, and yaw control is implemented with a custom addition of a servo controlled rudder. The wingspan is 38 inches (96.5 cm) and the planform wing area is 356 in^2 (2297 cm^2). The vehicle is 24 inches (61.0 cm) long with a weight of 2.5 lbf (11.12 N). The wing section has an estimated zero angle of attack coefficient of lift of $c_l = 0.3$, and the wing is inclined 3° (0.052 rad) relative to the water line.

4.1.2 Control Modes

With a general description of the modeled system, the next task formulates how the system will be controlled. All control is accomplished through the satellite, which has three different control inputs: throttle, elevator, and rudder. The next sections look at each mode in detail, describe how the control

impacts the system, and how this is used with the outer control loop. It also describes how the three control inputs are mirrored by the three component force vectors acting at the hub anchor point.

Throttle

The throttle adjusts the amount of force generated by the motor system, which influences the horizontal position of the satellite relative to the central hub. During operation, a lateral tension pulls at the hub anchor point. Adjusting the relative horizontal position, changes the magnitude of the lateral force. A relative position leading the hub increases the lateral tension, and a relative position behind the hub decreases the lateral tension. Throttle control is a very stable subsystem, because the satellite drag counteracts the throttle force from the motor.

Elevator

The elevator adjusts the deflection of the control surface on the horizontal stabilizer, which influences the vertical position of the satellite relative to the central hub. During operation, a vertical tension pulls at the hub anchor point. Adjusting the relative vertical position, changes the magnitude of the vertical force. A relative position above the hub increases vertical tension, and a relative position below the hub decreases the vertical tension. Elevator control is a marginally stable subsystem, because the satellite pivots around a point with no restoring forces.

Rudder

The rudder adjusts the deflection of the control surface on the vertical stabilizer, which influences the heading of the satellite relative to the central hub. During operation, a radial tension pulls outward on the hub anchor point. Adjusting the relative heading, changes the magnitude of the radial force. A relative heading away from the hub increases the radial tension, and a relative heading toward the hub decreases the radial tension. Rudder control is the most stable subsystem, because the centrifugal force acting on the satellite wants to remain aligned with the tether anchored on the satellite.

4.1.3 State Space Signals

To linearize the RTP system, suitable state space signals must be established. The following describes the inputs, states, and outputs used during the linearization process.

Inputs

There are three control inputs for each satellite, where each control input influences a state of the satellite relative to the central hub. The throttle command γ, is in Newtons. It adjusts the force generated by the motor system, and influences the relative horizontal position of the satellite. The elevator command α is in radians. It is a measure of the elevator angle of deflection, and it influences the relative vertical position of the satellite. The rudder command β is also in radians. It describes the rudder angle of deflection, and it influences the relative heading of the satellite. Together they form

$$u(t) = [\ \gamma,\ \alpha,\ \beta\ ]^T \tag{4.1}$$

which is the control input vector signal.

States

The RTP system has ten total states. The first two states describe roll ϕ and pitch θ of the satellite in the inertial frame. The next three states express relative positions between the satellite and hub. They are heading ψ, horizontal position η, and vertical position μ. The final five states are the derivatives of the first five states. The vector signal

$$x(t) = [\ \phi,\ \theta,\ \psi,\ \eta,\ \mu,\ \dot{\phi},\ \dot{\theta},\ \dot{\psi},\ \dot{\eta},\ \dot{\mu},\ ]^T \tag{4.2}$$

describes the states of the satellite system.

Outputs

The outer loop controller uses relative positions of the satellites to impart forces on the central hub. Because the outer loop specifies relative positions, it is natural to design the inner loop controller so that the satellites track these relative positions. The output vector signal is populated as

$$y(t) = [\ \eta,\ \mu,\ \psi\ ]^T \tag{4.3}$$

which are the relative horizontal, vertical, and heading positions. Because there is a direct mapping between states and outputs, define

$$C = \begin{bmatrix} 0 & 0 & 0 & 1 & 0 & 0 & 0 & 0 & 0 & 0 \\ 0 & 0 & 0 & 0 & 1 & 0 & 0 & 0 & 0 & 0 \\ 0 & 0 & 1 & 0 & 0 & 0 & 0 & 0 & 0 & 0 \end{bmatrix} \tag{4.4}$$

which is the state space output matrix.

Linearized System

The selection of states and outputs lead directly toward the output matrix C. A direct relationship between the inputs and the states is not analytically determined. Following the linearization procedure described earlier, yields the state matrix A and input matrix B. Both matrices are provided in (2.45). Together, (A, B, C) form the RTP transfer matrix with $G(s) = C(sI - A)^{-1}B$.

4.1.4 Relative Gain Array

The RGA uses the DC gain of the transfer matrix

$$G(0) = \begin{bmatrix} -1.26 & 52.84 & 0.34 \\ -0.04 & 17.93 & -0.02 \\ -0.04 & 0.86 & 0.30 \end{bmatrix} \tag{4.5}$$

and its inverse

$$G^{-1}(0) = \begin{bmatrix} -0.90 & 2.60 & 1.18 \\ -0.002 & 0.06 & 0.006 \\ -0.11 & 0.15 & 3.45 \end{bmatrix}. \tag{4.6}$$

The elements of the relative gain array Λ are populated with $\lambda_{ij} = [G(0)]_{ij} \ \ G^{-1}(0)\ _{ji}$ which yields

$$\begin{aligned} \Lambda &= \begin{bmatrix} (-1.26)(-0.90) & (52.84)(-0.002) & (0.34)(-0.11) \\ (-0.04)(2.60) & (17.93)(0.06) & (-0.02)(0.15) \\ (-0.04)(1.18) & (0.86)(0.006) & (0.30)(3.45) \end{bmatrix} \\ &= \begin{bmatrix} 1.138 & -0.102 & -0.036 \\ -0.094 & 1.097 & -0.003 \\ -0.044 & 0.005 & 1.039 \end{bmatrix} \end{aligned} \tag{4.7}$$

for the CSR system. The matrix has relatively large positive elements on the main diagonal, and nearly zero values for all other entries. This indicates a strong correlation between the input-output pairs, so decentralized control is a viable option.

4.1.5 SISO Subsystem

The RGA indicates that decentralized control is appropriate, so the first controller development centers around state feedback applied to SISO subsystems within the RTP model. The full A and B matrices are used to extract the linearized SISO models. Linearizing the rudder subsystem yields

$$A_\beta = \begin{matrix} 0 & 1 \\ -62.64 & 0 \end{matrix},\ B_\beta = \begin{matrix} 0 \\ 13.78 \end{matrix},\ C_\beta^T = \begin{matrix} 1 \\ 0 \end{matrix} \tag{4.8}$$

where $x_\beta(t) = [\ \psi(t),\ \dot{\psi}(t)\ ]^T$ is based on the relative heading. Linearizing the throttle subsystem leads to

$$A_\gamma = \begin{matrix} 0 & 1 \\ 0 & 2.45 \end{matrix},\ B_\gamma = \begin{matrix} 0 \\ 0.54 \end{matrix},\ C_\gamma^T = \begin{matrix} 1 \\ 0 \end{matrix} \tag{4.9}$$

where $x_\gamma(t) = [\ \eta(t),\ \dot{\eta}(t)\ ]^T$ uses the relative horizontal position for feedback. The elevator subsystem is marginally stable, so both the relative vertical position $\mu(t)$ and the pitch angle $\theta(t)$ are used as feedback signals. Linearize the elevator subsystem as

$$\begin{aligned} A_\alpha &= \begin{bmatrix} 0 & 0 & 1 & 0 \\ 0 & 0 & 0 & 1 \\ 0 & 187.75 & 9.40 & 0.02 \\ 0 & -59.95 & -5.91 & 0 \end{bmatrix}, \\ B_\alpha &= \begin{bmatrix} 0 \\ 0 \\ 13.70 \\ 12.41 \end{bmatrix},\ C_\alpha^T = \begin{bmatrix} 1 \\ 0 \\ 0 \\ 0 \end{bmatrix} \end{aligned} \tag{4.10}$$

where $x_\alpha(t) = [\ \mu(t),\ \theta(t),\ \dot{\mu}(t),\ \dot{\theta}(t)\ ]^T$.

The SISO controller requires direct measurements of the relative states used as feedback during the control loop. Initially, it is assumed that all states are available for measurement, which allows for this type of control. However, standard GPS is not accurate enough to measure the relative positions of the satellites. This issue is resolved through MIMO state feedback and state estimators. For now, SISO simulations serve as a benchmark to compare against the MIMO controllers.

4.2 SISO State Feedback

The previous section described the input channels as: (1) throttle for relative horizontal position, (2) elevator for relative vertical position, and (3) rudder for relative heading. It also linearized the full nonlinear RTP system and reduced the system into three linear subsystems. This first controls analysis uses those linear models, describes the process for selecting the desired system response, and then implements state feedback controllers on the three SISO subsystems that make up the RTP system.

4.2.1 Desired System Response

The desired closed-loop system response can be arbitrarily selected with state feedback. For illustrative purposes, the first analysis will implement identical response characteristics on each of the subsystems. In future developments, each system may have a uniquely optimized dynamic response to accommodate other design considerations, such as power consumption or disturbance rejection.

As a starting point, the desired settling time should be around $t_s = 0.5$ seconds, and the percent overshoot should be close to $M_p = 5\%$. The goal is to obtain the real and imaginary parts of the complex roots, σ and ω, respectively. Obtain the real part ($\sigma = \text{Re}[\lambda]$) of the complex root with

$$\sigma = \frac{4.6}{t_s} = \frac{4.6}{0.5} = 9.2 \tag{4.11}$$

and solve for the damping ratio as

$$\zeta = \frac{\overline{\ln(M_p)^2}}{\pi^2 + \ln(M_p)^2} = \frac{\overline{\ln(0.05)^2}}{\pi^2 + \ln(0.05)^2} = 0.7. \tag{4.12}$$

The natural frequency is determined by

$$\omega_n = \frac{\sigma}{\zeta} = \frac{9.2}{0.7} = 13.14 \tag{4.13}$$

so the damped natural frequency becomes

$$\omega = \omega_n \quad \overline{1 - \zeta^2} = 13.14 \quad \overline{1 - 0.7^2} = 9.39 \tag{4.14}$$

which yields the imaginary part ($\omega = \text{Im}[\lambda]$) of the complex root. For simplicity during the control development and simulation, the real and imaginary values are rounded slightly to $\sigma = 10$ and $\omega = 10$. This gives the complex pair as

$$s + \sigma \pm \omega j = s + 10 \pm 10j \tag{4.15}$$

so the desired characteristic polynomial becomes

$$\begin{aligned} \alpha(s) &= (s + 10 + 10j)(s + 10 - 10j) \\ &= s^2 + 20s + 200 \end{aligned} \tag{4.16}$$

which yields polynomial coefficients of $\alpha_0 = 200$ and $\alpha_1 = 20$. The rudder and throttle both have two states, so this polynomial is used directly. The elevator has four total states, so a second set of complex poles are added at the same location, which leads to

$$\begin{aligned} \alpha(s) &= (s^2 + 20s + 200)(s^2 + 20s + 200) \\ &= s^4 + 40s^3 + 800s^2 + 8000s + 40000 \end{aligned} \tag{4.17}$$

with polynomial coefficients of $\alpha_0 = 40000$, $\alpha_1 = 8000$, $\alpha_2 = 800$, and $\alpha_3 = 40$.

4.2.2 Rudder Controller

Begin with rudder control, because it is the most straight forward to implement. Rudder angle $\beta(t)$ is the input $u_\beta(t)$ to the subsystem, and the output $y_\beta(t)$ is designated as the relative heading $\psi(t)$. The state space realization of the rudder subsystem is

$$\dot{x}_\beta(t) = A_\beta x_\beta(t) + B_\beta u_\beta(t), \quad y_\beta(t) = C_\beta x_\beta(t) \tag{4.18}$$

where A_β, B_β, and C_β are provided in (4.8). Solve for the controllability matrix as

$$\mathbb{C}_\beta = \begin{matrix} 0 & 13.78 \\ 13.78 & 0 \end{matrix} \tag{4.19}$$

which determines the transformation matrix

$$T_\beta = \begin{matrix} 13.78 & 0 \\ 0 & 13.78 \end{matrix} . \tag{4.20}$$

The canonical form of the subsystem becomes

$$\check{A}_\beta = \begin{matrix} 0 & 1 \\ -62.64 & 0 \end{matrix}, \; \check{B}_\beta = \begin{matrix} 0 \\ 1 \end{matrix}, \; \check{C}_\beta^T = \begin{matrix} 13.78 \\ 0 \end{matrix} \tag{4.21}$$

which has the following characteristic polynomial

$$d_\beta(s) = s^2 + 0s + 62.64. \tag{4.22}$$

Direct matching yields the transformed state gain

$$\check{K}_\beta = \begin{array}{cc} -137.36 & -20 \end{array} \tag{4.23}$$

which determines the system state gain

$$K_\beta = \check{K}_\beta T_\beta^{-1} = \begin{array}{cc} -9.97 & -1.45 \end{array} . \tag{4.24}$$

The closed-loop system is described by

$$\begin{aligned} \bar{A}_\beta &= A_\beta + B_\beta K_\beta \\ &= \begin{array}{cc} 0 & 1 \\ -200 & -20 \end{array} \end{aligned} \tag{4.25}$$

which has the desired closed-loop eigenvalues. The reference gain is given by

$$k_\beta = -[C_\beta \bar{A}_\beta^{-1} B_\beta]^{-1} = 14.51 \tag{4.26}$$

which achieves the desired closed-loop response.

4.2.3 Throttle Controller

Throttle control requires one additional step from the rudder controller development. It uses the relative horizontal position of the satellite with respect to the hub, so a rotation matrix is applied to obtain this value. The throttle $\gamma(t)$ is the input $u_\gamma(t)$ to the subsystem, and the output $y_\gamma(t)$ is designated as the relative horizontal position $\eta(t)$. The state space realization of the throttle subsystem is given by

$$\dot{x}_\gamma(t) = A_\gamma x_\gamma(t) + B_\gamma u_\gamma(t), \;\; y_\gamma(t) = C_\gamma x_\gamma(t) \tag{4.27}$$

where A_γ, B_γ, and C_γ are provided in (4.9). Solve for the controllability matrix as

$$\mathbb{C}_\gamma = \begin{array}{cc} 0 & 0.54 \\ 0.54 & 1.323 \end{array} \tag{4.28}$$

which determines the transformation matrix

$$T_\gamma = \begin{array}{cc} 0.54 & 0 \\ 0 & 0.54 \end{array} . \tag{4.29}$$

The canonical form of the subsystem becomes

$$\check{A}_\gamma = \begin{array}{cc} 0 & 1 \\ 0 & 2.45 \end{array} , \; \check{B}_\gamma = \begin{array}{c} 0 \\ 1 \end{array} , \; \check{C}_\gamma^T = \begin{array}{c} 0.54 \\ 0 \end{array} \tag{4.30}$$

which has the following characteristic polynomial

$$d_\gamma(s) = s^2 - 2.45s + 0. \tag{4.31}$$

Direct matching yields the transformed state gain

$$\check{K}_\gamma = \begin{array}{cc} -200 & -22.45 \end{array} \tag{4.32}$$

which determines the system state gain

$$K_\gamma = \check{K}_\gamma T_\gamma^{-1} = \begin{array}{cc} -370.37 & -41.57 \end{array} . \tag{4.33}$$

The closed-loop system is described by

$$\begin{aligned} \bar{A}_\gamma &= A_\gamma + B_\gamma K_\gamma \\ &= \begin{array}{cc} 0 & 1 \\ -200 & -20 \end{array} \end{aligned} \tag{4.34}$$

which has the desired closed-loop eigenvalues. The reference gain is given by

$$k_\gamma = -[C_\gamma \bar{A}_\gamma^{-1} B_\gamma]^{-1} = 370.37 \tag{4.35}$$

which achieves the desired closed-loop response.

4.2.4 Elevator Controller

The elevator controller is the most complicated subsystem to control. This subsystem is marginally stable, so it uses two different states in the feedback loop. The elevator $\alpha(t)$ is the input $u_\alpha(t)$ to the subsystem, and the output $y_\alpha(t)$ is designated as the relative vertical position $\mu(t)$. The state space realization of the elevator subsystem is given by

$$\dot{x}_\alpha(t) = A_\alpha x_\alpha(t) + B_\alpha u_\alpha(t), \;\; y_\alpha(t) = C_\alpha x_\alpha(t) \tag{4.36}$$

where A_α, B_α, and C_α are provided in (4.10). Solve for the controllability matrix as

$$\mathbb{C}_\alpha = \begin{bmatrix} 0 & 13.70 & 129.0 & 3541 \\ 0 & 12.40 & -80.9 & -1507 \\ 13.70 & 129.0 & 3541 & 18050 \\ 12.41 & -80.9 & -1507 & -16080 \end{bmatrix} \tag{4.37}$$

which determines the transformation matrix

$$T_\alpha = \begin{bmatrix} 3151 & 0.248 & 13.70 & 0 \\ 0 & -197.6 & 12.41 & 0 \\ 0 & 3151 & 0.248 & 13.70 \\ 0 & 0 & -197.9 & 12.41 \end{bmatrix} . \tag{4.38}$$

The canonical form of the subsystem becomes

$$\begin{aligned} \check{A}_\alpha &= \begin{bmatrix} 0 & 1 & 0 & 0 \\ 0 & 0 & 1 & 0 \\ 0 & 0 & 0 & 1 \\ 0 & -546.1 & -60.1 & 9.4 \end{bmatrix}, \\ \check{B}_\alpha &= \begin{bmatrix} 0 \\ 0 \\ 0 \\ 1 \end{bmatrix}, \; \check{C}_\alpha^T = \begin{bmatrix} 3151 \\ 0.248 \\ 13.70 \\ 0 \end{bmatrix} \end{aligned} \tag{4.39}$$

which has the following characteristic polynomial

$$d_\alpha(s) = s^4 - 9.4s^3 + 60.1s^2 + 546.1s + 0. \tag{4.40}$$

Direct matching yields the transformed state gain

$$\check{K}_\alpha = [\, -40,000,\; -7453.9,\; -739.9,\; -49.4\,] \tag{4.41}$$

which determines the system state gain

$$K_\alpha = [\, -12.7,\; -32.0,\; -4.37,\; 0.84\,]. \tag{4.42}$$

The closed-loop system is described by

$$\begin{aligned} \bar{A}_\alpha &= A_\alpha + B_\alpha K_\alpha \\ &= \begin{bmatrix} 0 & 0 & 1 & 0 \\ 0 & 0 & 0 & 1 \\ -173.9 & -251.1 & -50.5 & 11.6 \\ -157.5 & -457.5 & -60.2 & 10.5 \end{bmatrix} \end{aligned} \tag{4.43}$$

which has the desired closed-loop eigenvalues. The reference gain is given by

$$k_\alpha = -[C_\alpha \bar{A}_\alpha^{-1} B_\alpha]^{-1} = 12.69 \tag{4.44}$$

which achieves the desired closed-loop response.

4.3 MIMO State Feedback

SISO design techniques selected the exact desired system response within all the input/output channels. The SISO simulations are an important design tool, while analyzing a disturbance for a single channel. However, implementing the SISO controllers on the CSR is not possible, because they require measurements of the relative states of the satellites. This section presents the MIMO controller development, which is able to overcome the SISO limitations. It presents the MIMO system characteristics, controllability and observability of the system, the desired system response, and the gain matrices needed to implement MIMO state feedback.

4.3.1 MIMO System Characteristics

The desired system response mirrors the values developed for the SISO controllers. The desired closed-loop poles are placed at $s = -10 \pm 10i$. With ten total states, that pole location will have a multiplicity of five, so the desired characteristic polynomial for the MIMO system becomes

$$\alpha(s) = [(s + 10 + 10i)(s + 10 - 10i)]^5. \tag{4.45}$$

Using a compact form of notation (used by Matlab), let a vector represent the polynomial coefficients

$$[\, a_n,\; \cdots,\; a_1,\; a_0\,] \;\Rightarrow\; a_n s^n + \cdots + a_1 s + a_0 \tag{4.46}$$

so the desired system response is expressed as

$$\alpha(s) = \begin{bmatrix} 1 \\ 1.0e2 \\ 5.0e3 \\ 1.6e5 \\ 3.6e6 \\ 5.9e7 \\ 7.2e8 \\ 6.4e9 \\ 4.0e10 \\ 1.6e11 \\ 3.2e11 \end{bmatrix}^T \tag{4.47}$$

and the characteristic polynomial is given by

$$\begin{aligned} d(s) &= \det(sI - A) \\ &= \begin{bmatrix} 1 \\ 14 \\ 140 \\ 1077 \\ 5972 \\ 19369 \\ 73427 \\ 40690 \\ -53512 \\ -352074 \\ -110721 \end{bmatrix}^T \end{aligned} \tag{4.48}$$

The Smith McMillan Form is given as

$$G_{SM}(s) = \text{diag}\ \left[\tfrac{1}{d(s)}, \tfrac{1}{d(s)}, g(s)\right] \qquad g(s) = (s - 4.97e{-}5 \pm 4.79i)(s + 12.78)(s - 12.79) \tag{4.49}$$

so the poles are

$$s_p = \left\{ \begin{array}{r} -6.98 \pm 3.11i \\ 0.08 \pm 6.78i \\ -0.01 \pm 4.79i \\ -1.09 \pm 1.55i \\ 1.51 \\ -0.33 \end{array} \right\} \tag{4.50}$$

and the zeros are

$$s_z = \left\{ \begin{array}{r} 4.97e{-}5 \pm 4.79i \\ -12.78 \\ 12.79 \end{array} \right\}. \tag{4.51}$$

4.3.2 Controllability and Observability

Controllability and observability are formed directly from the MIMO state space matrices (4.4) and (2.45). Using (3.10), the first ten columns of the MIMO controllability matrix $\mathbb{C}$, are presented in (4.54). The matrix is full rank because rank($\mathbb{C}$) = 10, so the system is fully controllable. All of the first 10 columns are linearly independent, so the controllability indexes are

$$\mu_1 = 4, \quad \mu_2 = 3, \quad \mu_3 = 3. \tag{4.52}$$

Using (3.13), the first ten rows of the MIMO observability matrix $\mathbb{O}$, are presented in (4.55). The matrix is full rank because rank($\mathbb{O}$) = 10, so the system is fully observable. All of the first 10 rows are linearly independent, so the observability indexes are

$$\nu_1 = 4, \quad \nu_2 = 3, \quad \nu_3 = 3. \tag{4.53}$$

This is a very important result for the CSR system. Because the system is fully controllable, full state feedback can be applied to the system. Because the system is fully observable, state estimation and reduced order estimation controllers can be implemented. This result is necessary to move forward when GPS is not available to measure the relative states of the satellites.

4.3.3 MIMO System Matrices

The procedure outlined earlier was followed, and the state feedback matrices were obtained. Matrix P, K_x, and K_r are presented in (4.56), (4.57), and (4.58), respectively.

4.4 Simulations

Simulations have been developed for two of the control architectures presented: RTP SISO state feedback, and RTP MIMO state feedback. The simulations show very promising results. Due to time constraints, simulations for the remaining controllers are left as future work.

4.4.1 SISO Simulations

Several simulations were run to demonstrate the controller performance on the RTP control line model. The SISO controllers are applied to the nonlinear model in the simulation to demonstrate the system response, disturbance rejection, and reference tracking capabilities. The simulations are shown in Figures 4.1, 4.2, 4.3, and 4.4, and the trimmed RTP model is displayed in Figure 4.5.

The first three figures present the system response when only the specified controller is applied, and the other two control inputs are left at their trimmed values. Figure 4.4 simulates the system when all control subsystems are applied and disturbances are applied to each input-output pair.

Figure 4.1 shows the simulation when throttle control is applied, and elevator and rudder inputs maintain their trimmed values. At 0.5 seconds, the system has a 5 Newton impulse disturbance applied at the nose of the satellite. At 1.5 seconds, the reference signal changes so the system must track a new relative horizontal position of -0.015 meters.

Figure 4.2 shows the simulation when elevator control is applied, and throttle and rudder inputs maintain their trimmed values. At 0.5 seconds, the system has a 3 Newton impulse disturbance applied downward at the CG of the satellite. At 1.5 seconds, the reference signal changes so the relative vertical position is -0.015 meters of the trimmed value.

Figure 4.3 shows the simulation when rudder control is applied, and throttle and elevator inputs maintain their trimmed values. At 0.5 seconds, the system has a 5 Newton-meter torque impulse disturbance applied on the vertical axis at the CG of the satellite. At 1.5 seconds, the reference signal changes and the system must track a new relative heading of -1.625 radians.

Figure 4.4 shows the simulation when all control signals are applied, and the system experiences disturbances on all three subsystems. At 0.5 seconds, the system has the disturbance applied to the rudder subsystem, at 1.5 seconds, the system has the disturbance applied to the throttle subsystem, and at 2.5 seconds, the system has the disturbance applied to the elevator subsystem.

Each simulation shows that the closed-loop response has a settling time around 0.5 seconds, with approximately 5% overshoot, as specified during the controller design. Additionally, each individual system demonstrates that the overall system has significant decoupling between states, so that each control input mostly influences the desired system state. The final simulation with all control signals applied, shows that each input-output pair does not conflict with the other input-out pairs, and the full system behaves very similarly to the individual simulations.

4.4.2 MIMO RTP Simulation

The SISO controllers are easily implemented within the simulation, and serve as a good tool for evaluating controller performance on a single input/output channel. However, the full CSR satellite will require MIMO control because that is the form needed to perform state estimation when the relative position of the satellite is not known.

To provide an accurate comparison, the full MIMO controller was designed with the same response characteristics as the SISO subsystems. The system was evaluated, and the gain matrices were obtained in a previous section. The simulation of the system was subjected to the same disturbances as the previous SISO simulations, but the MIMO controller was implemented to mitigate the tracking errors. Because the Relative Gain Array (RGA) showed very minimal coupling between the other input/output channels, the MIMO controller simulation should look very similar to the SISO controller simulations. Figure 4.6 demonstrates that this is the case, were the MIMO system response is nearly identical to the SISO subsystem controllers.

4.4.3 Future Simulations

The current simulations show promise for the CSR vehicle. The RGA indicates that there are strong one-to-one mappings between the inputs and outputs. This result is very favorable because implementing the control system is a much more straight forward process when the system is decentralized. The simulations also show that SISO design techniques can be used to formulate the closed-loop system dynamics, and the MIMO controller will very closely mirror the prescribed dynamics.

The next round of simulations will implement the state estimator and reduced order state estimator. Existing control theory states that because the system is both controllable and observable, these controllers will work for the CSR system. However, simulations are still needed to demonstrate this type of control. Additionally, the theory states that the error can be reduced to zero at an arbitrarily fast decay rate; however, faster dynamics require more aggressive control authority. Simulating the estimator controllers will indicate what decay rate is achievable within the actuator bandwidths.

The final set of simulations prior to hardware testing will develop the parameter estimation adaptive controller. Similar to the reduced order controllers, theory states that a persistently exciting signal ensures that the adaptation will push the parameter estimates toward their true values. However, it does not give any indication of what signal frequencies are appropriate. Simulating the parameter estimation is the best way to make sure the multisine signal injection is within the bandwidth of the system dynamics, and that the satellite vehicle has an acceptable transient response.

$$\mathbb{C} = \begin{bmatrix} 0 & 0 & 0 & 0 & 0.11 & -1.33 & -0.01 & -1.10 & -0.07 & 0.07 \\ 0 & 0 & 0 & 0 & 16.37 & 0 & 0 & -61.29 & -0.25 & 5.16 \\ 0 & 0 & 0 & -0.01 & 0 & 13.40 & -0.00 & -2.66 & -0.07 & -0.68 \\ 0 & 0 & 0 & -0.83 & 0.01 & -0.04 & 0.78 & 1.72 & 0.02 & -0.29 \\ 0 & 0 & 0 & 0 & 15.98 & 0.07 & -1.31 & -221.56 & -3.36 & 19.93 \\ 0 & 0.11 & -1.33 & -0.01 & -1.10 & -0.07 & 0.07 & -60.84 & 60.45 & 3.50 \\ 0 & 16.37 & 0 & 0 & -61.29 & -0.25 & 5.16 & -138.94 & 116.82 & -76.68 \\ -0.01 & 0 & 13.40 & -0.00 & -2.66 & -0.07 & -0.68 & -84.00 & -609.03 & 0.48 \\ -0.83 & 0.01 & -0.05 & 0.78 & 1.72 & 0.02 & -0.29 & 238.65 & -9.75 & -0.71 \\ 0 & 15.98 & 0.07 & -1.31 & -221.56 & -3.36 & 19.93 & -457.58 & 423.33 & -281.20 \end{bmatrix} \tag{4.54}$$

$$\mathbb{O} = \begin{bmatrix} 0 & 0 & 0 & 1 & 0 & 0 & 0 & 0 & 0 & 0 \\ 0 & 0 & 0 & 0 & 1 & 0 & 0 & 0 & 0 & 0 \\ 0 & 0 & 1 & 0 & 0 & 0 & 0 & 0 & 0 & 0 \\ 0 & 0 & 0 & 0 & 0 & 0 & 0 & 0 & 1 & 0 \\ 0 & 0 & 0 & 0 & 0 & 0 & 0 & 0 & 0 & 1 \\ 0 & 0 & 0 & 0 & 0 & 0 & 0 & 1 & 0 & 0 \\ 0.40 & 14.19 & -0.67 & -0.69 & 2.00 & -0.00 & 0 & -0.00 & -0.94 & 0.11 \\ 1.72 & -218.56 & 28.26 & -0.92 & 2.78 & 0 & -0.00 & -0.18 & 1.58 & -13.86 \\ -0.28 & -5.51 & -45.50 & 1.40 & -1.93 & 0.00 & 0 & -0.00 & 0.01 & -0.17 \\ -0.17 & -37.02 & 3.81 & 0.55 & -1.57 & 0.40 & 14.19 & -0.69 & 0.36 & 0.34 \end{bmatrix} \tag{4.55}$$

$$P = \begin{bmatrix} -6.56 & 0.00 & -0.65 & 0.01 & 0.03 & 0.03 & 0.00 & 0.00 & -0.00 & -0.00 \\ -0.78 & 0.15 & -0.10 & 0.01 & -0.13 & -6.56 & 0.00 & -0.65 & 0.00 & 0.04 \\ 150.59 & 1.11 & 16.09 & -1.13 & 25.29 & -0.78 & 0.12 & -0.08 & 0.00 & -0.11 \\ 17.75 & 19.17 & -0.58 & -0.05 & 2.68 & 150.59 & 1.11 & 16.12 & -1.32 & 26.49 \\ -0.35 & -0.00 & -0.03 & 0.00 & 0.00 & -0.01 & 0.00 & -0.00 & 0.00 & -0.00 \\ 0.27 & 0.03 & 0.03 & -0.00 & 0.05 & -0.35 & -0.00 & -0.03 & 0.00 & 0.00 \\ 8.04 & -0.15 & 0.89 & -0.06 & 1.35 & 0.27 & 0.03 & 0.03 & -0.00 & 0.03 \\ -3.29 & -0.01 & -0.33 & -0.00 & 0.05 & -0.11 & -0.00 & -0.01 & 0.00 & 0.00 \\ 2.59 & -0.30 & 0.32 & -0.02 & 0.44 & -3.29 & -0.01 & -0.33 & 0.00 & 0.03 \\ 75.62 & -1.62 & 8.37 & -0.57 & 12.73 & 2.59 & -0.32 & 0.33 & -0.00 & 0.31 \end{bmatrix} \tag{4.56}$$

$$K_x = \begin{bmatrix} 3.6e7 & 5.4e6 & 3.2e6 & -2.5e5 & 5.9e6 & 4.0e7 & 3.3e5 & 4.3e6 & -3.6e5 & 7.2e6 \\ 2.9e0 & 9.3e0 & -8.6e{-}1 & -9.2e{-}3 & 1.0e0 & -8.2e0 & 1.5e{-}1 & -8.9e{-}1 & 6.0e{-}3 & -7.6e{-}1 \\ -2.0e6 & -3.1e5 & -1.8e5 & 1.4e4 & -3.4e5 & -2.3e6 & -1.8e4 & -2.4e5 & 2.0e4 & -4.1e5 \end{bmatrix} \tag{4.57}$$

$$K_r = \begin{bmatrix} 1.7e3 & -4.5e4 & -2.2e3 \\ 2.6e{-}2 & -6.1e{-}1 & -2.7e{-}2 \\ -9.8e1 & 2.6e3 & 1.2e2 \end{bmatrix} \tag{4.58}$$

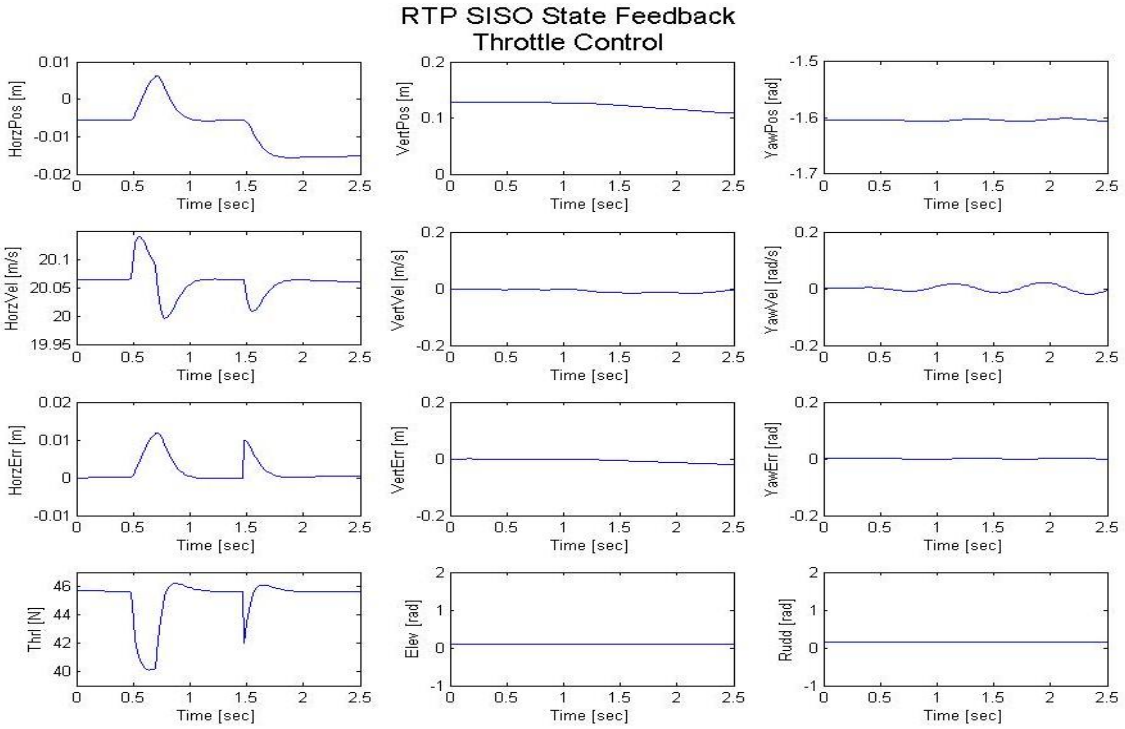

Figure 4.1: SISO throttle control.

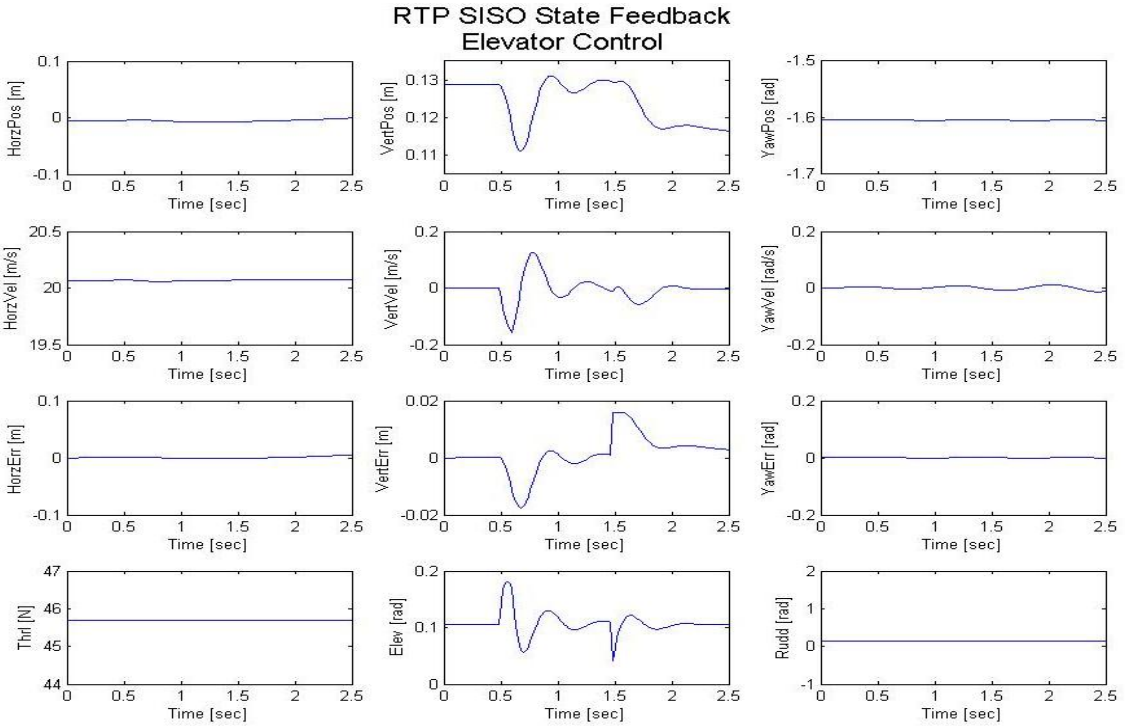

Figure 4.2: SISO elevator control.

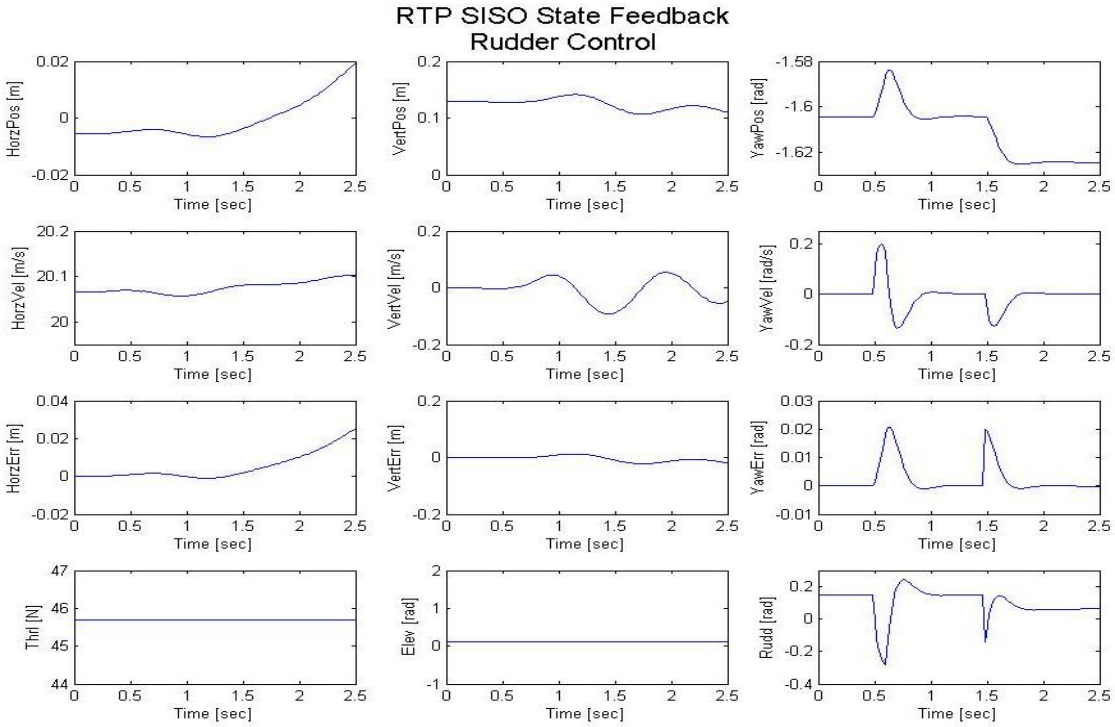

Figure 4.3: SISO rudder control.

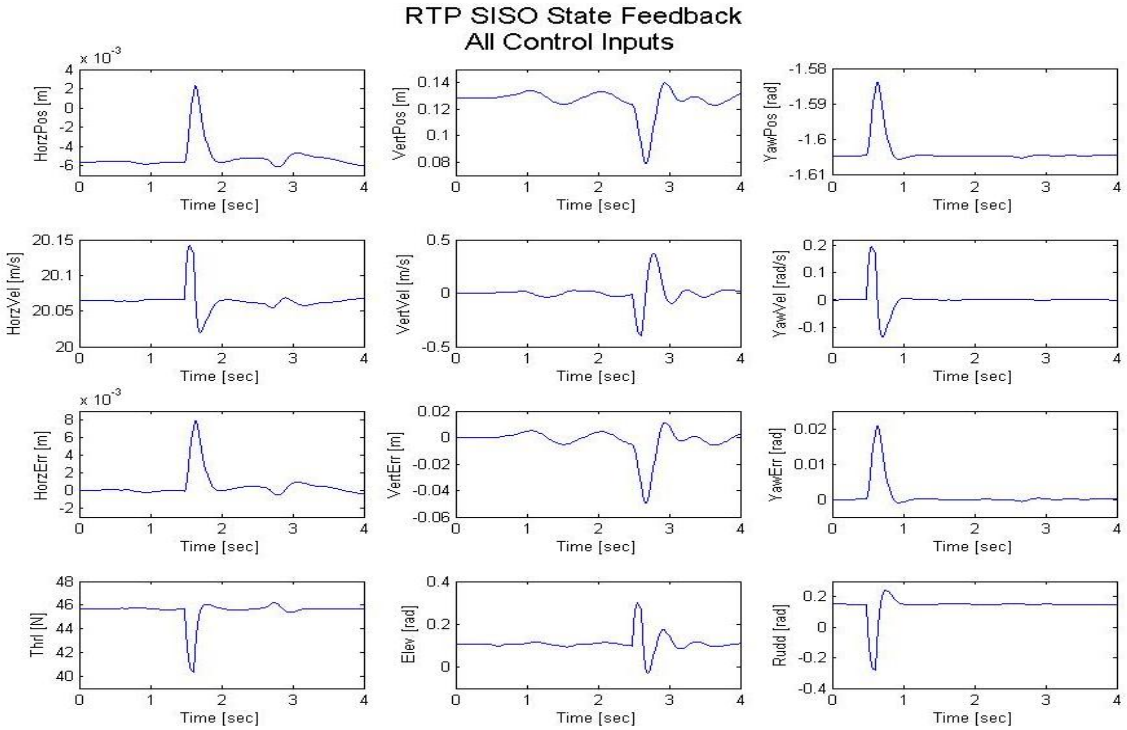

Figure 4.4: SISO all control inputs.

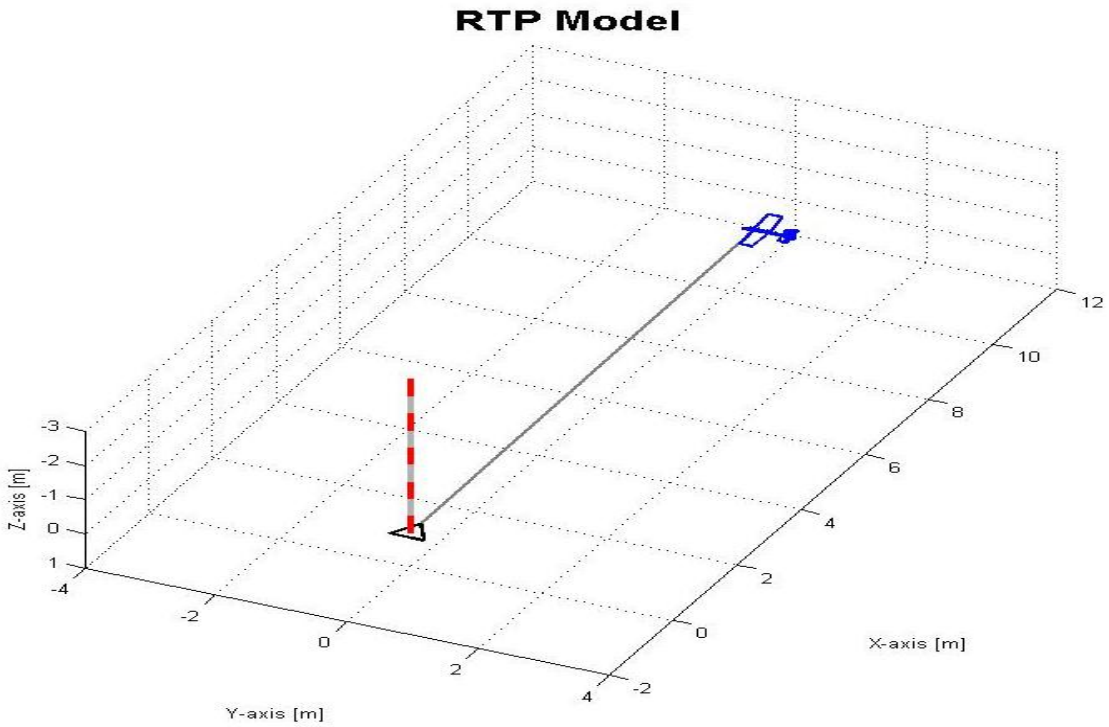

Figure 4.5: Trimmed RTP system.

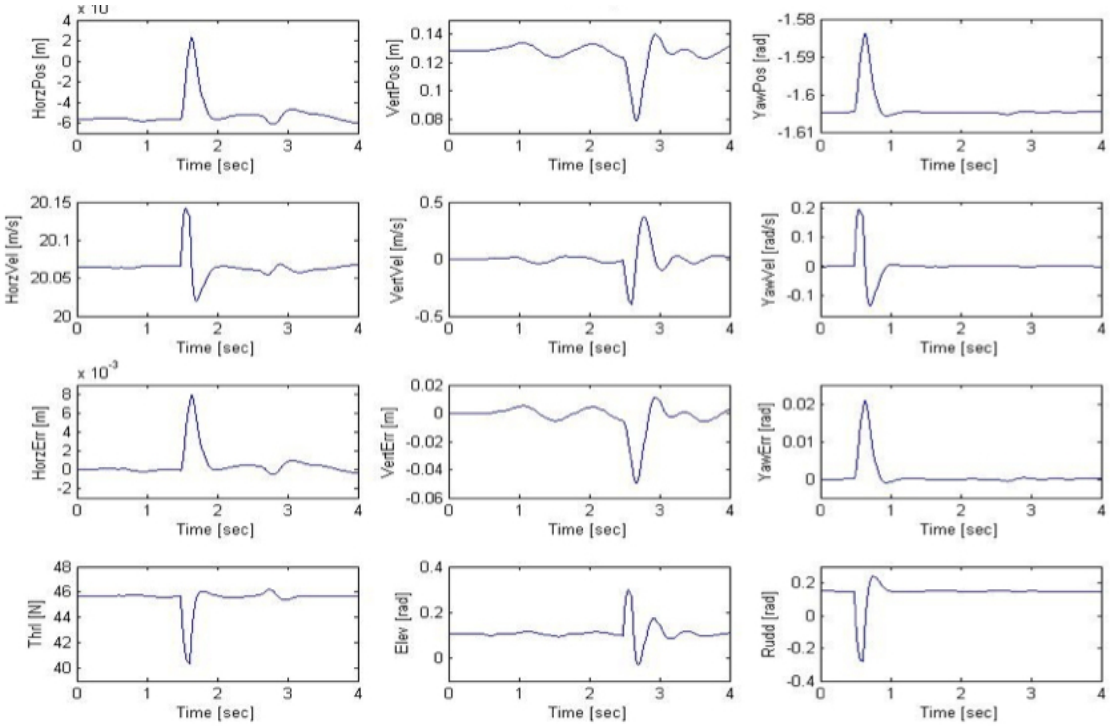

Figure 4.6: MIMO state feedback on RTP system.

Chapter 5

Prototype Testing Plan

As the saying goes, "The proof is in the pudding." Theory, analysis, and simulations are all valid endeavors and serve as useful design tools. However, a series of plots will never be as convincing as a prototype that successfully accomplishes an objective. The only way to truly claim the CSR vehicle is capable of eternal flight, is to demonstrate it on a physical platform.

Motivation

A simulation is only as good as its model. Even with sophisticated analysis, computational dynamics, and detailed modeling efforts, models always contain some discrepancies with the physical system. Some systems, like conventional aircraft, have a sufficient design history where new designs compared to historical data provide some level of validation. However, radically new concepts, like the CSR vehicle, have little basis for comparison, so providing a physical "proof-of-concept" is of utmost importance.

Objectives

The majority of future work focuses on developing hardware prototypes that demonstrate the abilities of the CSR system. The main development methodology for this research project follows a spiral design process. Rough models and prototypes are implemented as quickly as possible, data is collected for those embodiments, the data aids the model improvements, and more refined models lead into more sophisticated prototypes. This section outlines the plan of action that guides the prototype development process. It introduces the concept of a spiral development cycle, describes the prototypes utilized along the way, and illustrates the testing performed on each prototype.

Outline

Simulations serve as useful design tools, but real system validation comes from hardware demonstrations. The only way to claim eternal flight is possible, is to implement the vehicle in the real world. This chapter focuses on the prototype testing plan that progresses the CSR research and design effort.

Section 5.1 introduces *Spiral Development*, which is an alternative type of design process. Unlike a linear design philosophy, spiral development follows a cyclic design progression, which advances in small and manageable incremental steps.

Section 5.2 describes the *Prototype Vehicles* that are part of the spiral development process. Each vehicle serves a unique purpose during each stage of development, and progresses from simple models to more sophisticated and higher fidelity designs.

Section 5.3 outlines the *Testing Plan* that is performed on each prototype vehicle. With each new model, new hurdles and uncertainties are introduced, so the testing plan follows a natural progression from simple tasks to more risky maneuvers.

5.1 Spiral Development

Large engineering projects, like the design of new aircraft, traditionally spend a majority of the time, effort, and expense on upfront tasks. Spiral development is an alternative development process that offers many advantages over a traditional linear design path. This section describes the spiral development process, highlights the advantages and disadvantages, draws a parallel to a Design Build Fly methodology, and explains how spiral development is applied to the CSR research effort.

5.1.1 Description

Spiral development is a cyclic design cycle rather than a traditional linear progression. Instead of developing a single high fidelity model, each cycle utilizes prototypes to obtain a greater understanding of the conceptual system. Early models are very simple and only attempt to capture the most dominant system characteristics. Early prototypes are developed quickly and inexpensively, which serve as a proof of concept. Simulation models are compared against data collected from the prototypes. The validation process is the crucial step with spiral development, where one of two things will happen.

In the first outcome, the analysis may prove the project is infeasible. Unanticipated issues may be uncovered, or seemingly small problems are now recognized as major concerns. Quite possibly, the concept design relies on a key component or feature, which did not work out favorably in the prototype. When this is the case, a considerable amount of time, effort, and money is spared rather than proceeding forward with a doomed project.

For the second outcome, the analysis may indicate the project is feasible and warrants additional consideration. Under this scenario, the collected data validates or improves the existing computer model. The analysis may show that certain simplifying assumptions need to be refined, or it might identify parameter values that were initially estimated.

This refined model initiates a new round of prototype development. It serves as a design tool for sizing features, indicates where revisions are required, and reveals potential design improvements. The spiral development process continues in this cyclic fashion, where improved prototypes lead to refined models, and refined models create improved prototypes.

5.1.2 Spiral Development Pros and Cons

Spiral development is not intended to replace a linear design process under all circumstances. For some projects a traditional design approach is the best course of action. However, spiral development is a very useful tool that offers notable advantages under certain conditions.

Disadvantages

Some projects are not well suited for spiral development. Projects that are sufficiently straight forward may not need a prototype because pure analysis will suffice. Building a bridge is such an example, where analytic tools are available to calculate the loads, and there are minimal dynamics to take into account. Other times, building a prototype is not feasible. A nuclear power plant meets this criteria, because a prototype reactor is not practical or safe.

Advantages

Despite notable limitations, spiral development offers some distinct advantages over a linear design process. Whether spiral development is appropriate reduces down to a simple cost-benefit analysis. A linear design requires upfront costs in the form of building elaborate models, running monte carlo simulations, and processing data. Spiral development cuts many of these costs, but includes the time and expense building a series of prototypes. To determine which design technique is appropriate, simply estimate the total design expense for each. For example, systems with complex dynamics, like large ship building, may benefit from spiral development. An exorbitant amount of effort could go towards modeling the hull hydrodynamics, and the resulting model may still include unaccounted errors. A small scale prototype, tested under appropriate circumstances, would yield the actual hull dynamics.

5.1.3 Design Build Fly Methodology

The aviation industry traditionally follows the linear design process, where a new aircraft is extensively modeled, high fidelity wind tunnel rigs are constructed and tested, and the wind tunnel data is post processed and analyzed. The lead time for a new aircraft typically takes several years of upfront modeling, the wind tunnel models cost around a quarter million dollars, running the wind tunnel costs nearly $10k/hr, and a team of engineers pour over the wind tunnel data to replicate the nonlinear dynamics within their simulations.

The concept of spiral development is catching the attention of the aviation industry, where the term "Design-Build-Fly" (DFB) expresses the spiral development process applied to new aircraft design. Moving towards a design philosophy that uses simplifying assumptions and no wind tunnel data, raises concerns about the safety of these new aircraft. Reducing the fidelity of the model necessitates a comparable improvement in another area. The enabling theory to implement DBF in practice resides in adaptive control, which serve two primary roles.

First, adaptive controllers are built upon estimation and system identification techniques. When applied to a system with uncertain dynamics, these controllers take the inputs and measured outputs, and adjust the model dynamics until the true system parameters have been obtained. This aids in the spiral development process because the prototypes are developed on imperfect information, but the system identification yields the true parameter values which validate or refine the original model.

Second, adaptive controllers reduce risk while flying early prototypes built upon simplified models. These controllers operate in real time and tune controller parameters until the physical system matches the dynamics of a desired model. In essence, adaptive controllers start with an imperfect model and the prescribed desired response. When there is a discrepancy, the controller adapts which adjusts the control inputs until the physical system matches the desired system response. This greatly reduces the risk while flying prototype vehicles because the controller overcomes model uncertainties.

The new buzz term for adaptive control within the aviation industry is "Learn-to-Fly" (LTF). This describes an exaggerated scenario where the flight controller has minimal knowledge of the aircraft dynamics *a priori*, and the vehicle must "learn to fly" before it hits the ground.

5.1.4 CSR Application

Of all the potentially new aircraft concepts, the CSR system is especially well suited for a DBF approach. A lack of aerodynamic data, interactions from the tether, flexibility within the slender wing, and the multibody structure of the CSR, make the system a strong candidate for spiral development.

Data already exists for many fixed-wing aircraft which can ballpark control derivatives for conventional aircraft design. However, minuscule research and aerodynamic data is available for mono-wing designs, which is needed for CSR modeling. Furthermore, the satellites spin around the central hub, so there is a faster velocity outboard than inboard. It is nearly impossible to implement a non-uniform velocity profile within a wind tunnel, so no existing data or analysis is available to aid the satellite design.

A vast majority of aircraft are modeled as rigid bodies. Some research models flexible wings, but these still include a certain amount of rigidity in the structure. Very few applications have modeled a tether as it moves through space. Simple closed form solutions express a catenary model, but they do not account for varying drag forces acting throughout the length of the tether.

Finally, the hub has no independent control authority, so its dynamics are completely dependent on the tension within the tethers. A full multibody dynamics formulation is required to capture the equations of motion and the tether interactions. Controlling a body in such a manner is extremely novel, and not well documented in the literature.

The CSR project follows a spiral development life cycle, because there is very little existing research to assist the development process. Small incremental steps minimize risk during early development. Each cycle helps learn about the system, collects data on the current prototype, and refines simulation models. More advanced techniques are introduced over time, building upon previous lessons learned.

5.2 Prototype Vehicles

True to the spiral development philosophy, several prototypes are slated to aid the CSR design and analysis. A commercially available control line aircraft is the easiest and most economical entry point to test new avionics and control theories. A scaled mono-wing prototype with carbon fiber construction, more closely resembles the full scale vehicle at a manageable scale. A full scale prototype is the final step assessing eternal flight capabilities of the CSR system. At present, the control line aircraft is assembled and ready for data collection, the scaled model is under construction, and no formal plans have been established for the full scale prototype. The following sections describe each prototype vehicle and its purpose within the spiral development cycle.

5.2.1 Control Line Aircraft

The first prototype exhibits the greatest risk. Because it is the first vehicle, no data is available to contribute towards the design, so all preliminary design work is based on unverified simulation models. However, the simulation cannot be validated until the prototype is flown. Similarly, the avionics hardware and sensors have never been implemented on a real flight platform; only bench tested within a controlled environment. The first prototype vehicle falls into a viscous circle, where it is risky to fly without some validation, but the components are only validated through flying the vehicle.

Description

To minimize the amount of risk with the first prototype, the selected embodiment is a commercially available control line aircraft. Prior to RC radios, control line aircraft were the only means for hobbyists to fly. The system has a conventional airplane geometry with a gas engine or an electric motor. A steel cable tethers the plane to a handle, which is held by the operator. The handle has a second line that runs out the plane, which manipulates the elevator control surface. The throttle is run open-loop, the plane flies in a circle around the operator, and the operator maintains the elevation of he vehicle.

Purpose

This platform was selected as the first prototype vehicle, because it is mostly assembled and nearly ready to fly out of the box. A few slight modifications are needed for the CSR prototype application. The control line aircraft is equipped with throttle and elevator, so the rudder control surface is the only custom addition. Servos and a speed controller adjust the control inputs, which eliminates the need for a central operator. Finally, wireless serial radios communicate between the satellite and the central hub, which eliminates the original control line. The primary purpose of this vehicle minimizes risk while developing the custom electrical system. Utilizing a ready made vehicle with stable flight characteristics is the ideal means to implement the custom and untested sensors, avionics, hardware, and software.

5.2.2 Scaled Prototype

The first prototype tested avionics and control algorithms on a stable platform. The second prototype takes the next incremental step, and implements a system that more closely mirrors the CSR concept.

Description

The scaled prototype is a mono-wing design with a fuselage at the outboard tip, an elevator outboard of the fuselage, and a vertical stabilizer under the fuselage. The tapered wing starts with zero incidence angle at the root and wingtip, and gradually moves to a 6.5 $^\circ$ incidence angle about half way through the wing. The wing is carbon fiber Kevlar construction which measures seven feet long. The entire horizontal surface is deflected for pitch control, and 25% of the vertical stabilizer is articulated for yaw control.

Purpose

The purpose of the second prototype is to learn the characteristic aerodynamics of the satellite vehicle. The earliest models have simplifying assumptions which did not account for all the aerodynamics. Wing tip vortices and interactions between the horizontal stabilizer and elevator were not modeled.

The high aspect ratio wing has some degree of flexibility, which needs to be observed. Other aerodynamic features are unique to the CSR system, and not completely known. The rotating system has differential velocity over the wing surface, which may impact the relative heading. This prototype includes the tapered wing which achieves an elliptical lift distribution. Upwash from the wingtip produces lift on the horizontal stabilizer surface. These are significant aerodynamic effects that contributes to the eternal flight capability, and should be accounted for in the simulation model. The goal of this prototype is to observe the dynamics of the scaled system, and revise the simulation model to more accurately reflect these aerodynamic features.

5.2.3 Full Scale System

No formal plans have been established for a full scale prototype. The scaled prototype will shed valuable insight into the vehicle dynamics, which will lead to an improved model and a better understanding of how the full scale system behaves. However, to complete the analysis and to fully assess the eternal flight capabilities, this prototype will need to be built.

Description

The following description is based entirely on preliminary analysis work, and is subject to change once data is collected and evaluated from preliminary prototype models. The full scale CSR is expected to have around a 350 foot diameter. The satellite wing has a high aspect ratio greater than 50, with a 0.7 foot chord and a length of 35 feet. Control surface positions and sizes may change once new data is received, but are anticipated to be in nearly the same positions with the same relative sizes as the scaled prototype. Additional analysis is needed to specify the motor, propeller, batteries, and solar cells.

Purpose

The most obvious purpose of the full scale prototype is to demonstrate eternal flight capabilities. While, the first prototypes validated hardware and collected aerodynamic data, this vehicle is primarily designed to attain eternal flight. This vehicle follows the same testing procedure as the other prototypes which yields valuable information about the vehicle characteristics. As a worst case scenario, the collected data will shed insight into what revisions are needed to improve the performance of the vehicle; and if all goes well, the CSR will be the first aircraft in history to achieve eternal flight.

5.3 Testing Plan

Each prototype is a natural progression that moves from simple vehicles to more complex systems. For each prototype, a similar procedure is used which minimizes risk by first demonstrating fundamental capabilities, and then advances to more complex maneuvers. This section describes the three general types of tests: (1) round the pole, (2) constrained flight, and (3) free flight.

5.3.1 Round the Pole Flight

This test has the least amount of risk because it only involves a single satellite. These tests gather important data that is used for system identification and inner-loop controller design.

Description

The Round the Pole (RTP) flight most closely resembles the control line aircraft. A fixed pole anchors the system to the ground, but the pole has a bearing that is free to swivel about the vertical axis. The rotating hub has the data collection board, the transceiver for the RC radio, wireless telemetry to communicate with the satellite, and a magnetometer and rate gyro to measure heading and angular rate of the hub. A tether is attached to the hub and a single satellite vehicle. The satellite has throttle, elevator, and rudder control inputs which are obtained from the central computer.

Objectives

For each prototype, this test marks the maiden voyage, so the emphasis is on reducing risk to the

untested vehicle and gaining confidence in the system capabilities. All work has been purely analytical and performed in simulations, so these flights serve to validate and refine the computer models. The main goals of these tests are to focus on the inner loop-control mode functionality by:

- demonstrating the new system in flight,
- validating all hardware, sensors, and actuators,
- finding inputs to achieve static equilibrium,
- characterizing system dynamics through system identification,
- comparing flight data to simulations, and
- validating or refine existing model dynamics.

Approach

Testing a new prototype is done through incremental steps to make sure more risky maneuvers are built upon a firm foundation. The first step will bench test all the prototype components. All control inputs will be tested to make sure they work properly. All sensors will be evaluated to confirm good measurement, and that the data logger works properly.

Taxi Test: After the bench test, move on to the taxi test. This has the system in a ready to fly configuration, and throttles up the motor to around 90-95% of the value needed to achieve lift. The vehicle will spin around the hub at nearly flight speeds, but will not be enough to achieve lift. As the satellite runs around the pole, data logging is enabled, sensors acquire data, and the control surfaces are perturbed slightly to evaluate their effectiveness before the vehicle ever leaves the safety of the ground. Post processing will ensure the sensor data looks good, and changes will be made to tune the controller values and RC radio settings.

Trimming: The next series of tests will run the system open-loop controlled by a pilot. The vehicle will throttle up until lift is attained and the pilot will actuate the control inputs. The RC radio is equipped to trim the inputs onsite, so adjustments will be made to find the trimmed RC input values.

Doublets: With trimmed RC inputs, the pilot will command a series of doublets on each control channel. Doublets are a quick maneuver designed to perturb a single input and then quickly bring the vehicle back to a steady-state. The doublets begin with small magnitudes and gradually move up to larger command inputs. At some point the doublet will be deemed "too aggressive" and the test is complete. The data is post processed and the values of the most aggressive doublets are used to design control gains that are appropriate for the system.

Feedback Control: The open-loop flight data sheds light on the system dynamics. This information is used to determine the gains needed for a feedback control algorithm. The system is now flown closed-loop with the feedback controller applying input commands. Data is collected and the feedback control gains are adjusted as needed.

Signal Injection: Once the satellite has a solid feedback control law, the final step is to evaluate the system through multisine signal injection. This process flies the feedback controlled system and superimposes a summation of sinusoidal signals on top of the existing control inputs. These signals excite the system dynamics which generate new measurements that are used in the system identification process. The data is post processed and compared against the the existing simulation model, and revisions are made as needed, until the computer model matches the collected data. This revised computer model is used to develop the controller for the next round of testing: the constrained flight.

5.3.2 Constrained Flight

The RTP tests investigated the behavior of a single satellite vehicle. The constrained flight tests increase the level of difficulty by working with three satellites in unison. However, this series of tests still reduces the amount of risk by constraining the central hub.

Description

The constrained flight test setup is very similar to the RTP setup, except three satellites are tethered to the central hub. The satellite system is setup identically to the RTP system with all the same components and control inputs. The central hub has all the same components but three satellites are tethered to the hub. The first series of test has the hub constrained identically as the RTP system with

one single degree of freedom which rotates about the vertical axis. Subsequent tests relax the number of constraints where first, the hub is free to translate vertically, and then the hub is bounded but unconstrained in all six degrees of freedom.

Objectives

The RTP tests yielded insight into the dynamics of a single satellite which mirrors the inner-loop control. To control the complete CSR system also requires coordination between all the satellites to achieve the outer-loop control. The objective of these tests is to evaluate the effectiveness of the controller to implement coordination between all entities. It begins with the most basic task of maintaining equal spacing between satellites. Then it graduates to coordinated flights, first with a single degree of freedom, then with two degrees of freedom, and finally with bounded six degree of freedom tests. The main goals of the constrained flight tests are to:

- demonstrate equal spacing between satellites,
- single degree of freedom tests,
  - collective throttle and elevator
  - cyclic rudder and elevator
- two degree of freedom tests, and
  - collective throttle and elevator
  - cyclic rudder and elevator
- bounded unconstrained tests
  - collective throttle and elevator
  - cyclic rudder and elevator

Approach

These tests follow a similar progression to the RTP tests. All satellites are tuned using previously collected data and bench tested to confirm all hardware, software, and sensors are working properly.

Taxi Test: The first test is a taxi test. Just like before, all the satellites will throttle up to around 90-95% of their cruising speed and will taxi around the pole. The feedback control will be active on all three satellites. While taxiing the satellites will have the same elevation, so there will be minimal elevator commands. There is no outer-loop command that adjusts the relative heading, so there will be minimal rudder commands. The main demonstration will focus on the feedback controlled throttle commands to determine if the control law can maintain equal spacing between satellites and track a given hub angular rate.

Equal Spacing: Once the taxi test has been successfully completed, the next incremental step takes the vehicles off the ground. The hub is still constrained in all DOF except for vertical rotation. The reference signal increases the angular rate of the central hub, and the controller will ramp up the throttle to track the increased angular rate. Once the satellites attain cruising speed they will lift off. The feedback controller is responsible for all the inner-loop commands for each satellite, so the operator is solely responsible for adjusting the hub angular rate. The collected data will be analyzed and evaluate how effective the system maintained equal spacing. Any deficiencies or errors will be simulated to observe how those errors would impact an unconstrained system. If the data reflects positively, then the next round of testing begins.

Collective Commands: With equal spacing accomplished, the next tests perform more elaborate coordinated flight maneuvers that will be used for outer-loop control. The hub is still constrained to a single degree of freedom while the four outer-loop modes are evaluated. The tests begin with collective modes because they are easier to observe. The first test is collective throttle because it most closely resembles the previous set of tests. The system is ramped up to hover equilibrium state, and a reference command increases the angular rate of the central hub. When the satellites exceed their cruise speed, additional lift is generated and the vehicle will increase altitude. The next test runs collective elevator commands. When the system is in equilibrium, the operator increases the elevator reference signal, and the satellites begin to climb together. Collected data will evaluate whether the satellites maintain the same elevation and attitude during their ascent.

Cyclic Commands: After demonstrating collective commands, attention turns toward cyclic commands. Cyclic rudder is more stable that the elevator, so begin there. The system is brough to hover, and the operator commands a cyclic rudder command. Because the pole constrains the system, there

will be very little to observe onsite. However, the collected data should reveal whether the satellites change their relative headings in a cyclic manner. The final one DOF test is cyclic elevator which tilts the entire plane of rotation. Once in hover, the operator applies the command and the satellites will alter their elevations cyclically. The data should show that each satellite attains a low and high point at the same locations. It should also show that each satellite achieves the same elevation changes while navigating around the hub.

Relaxed Degree of Freedom: After successfully demonstrating coordinated flight with a single DOF hub, the next series of tests relax the number of constraints on the hub. The pole hardware is replaced so the hub is free to both rotate and translate about the vertical axis. The testing process is repeated for each of the four outer-loop control modes to make sure the feedback control is working as expected. The two DOF hub will shed more useful insight on the collective commands because they both influence the vertical translation of the system.

Bounded Free Flight: Demonstrating the horizontal translation is accomplished with the bounded free flight test. This test replaces the central hub connection. Rather than a bearing mounted on the pole, the central hub is fashioned as an annular ring. The ring is larger than the pole diameter so the hub is free to roll, pitch, and translate horizontally. This closely resembles unconstrained free flight dynamics, but still has the added security of placing a boundary on the central hub. Again, each of the four outer-loop control modes is tested under these new constraints, and data is reviewed to make sure the system is well behaved. To further reduce the amount of risk, moving into a fully unconstrained free flight, several rings of various diameters can be constructed to adjust the boundary distance. Smaller rings offer more security by limiting the range of motion. Once the system response behaves as expected, larger rings can showcase the unconstrained system dynamics.

5.3.3 Free Flight

Previous testing paved the way for the pinnacle of the prototype tests: the completely unconstrained free flight of the CSR system. This series of test marks the completion of each prototype, so the information gathered here is intended to aid in the next prototype development.

Description

These tests are run on the complete CSR vehicle. The training wheels have been removed, and it is time to see the big picture at work. All the avionics, hardware and sensors are the same for the satellite vehicles. The annular ring for the central hub has been replaced with the preferred embodiment of a convex cylindrical housing. The hub components are identical to the previous testing. Early tests will take off with the satellite arms fully extended, but more sophisticated prototypes may include a tether retraction mechanism for take off and landing.

Objectives

Unlike previous tests which were focused on developing capabilities needed for the control system, the objectives of the free flight tests are more specific to the individual prototype being tested. The focus of this testing is to acquire enough insight to aid the development of the next prototype, which will have different objectives from one prototype to the next. However, there are many commonalities that are shared among all the prototypes. Testing robustness to disturbances, waypoint navigation, and controller optimality are all accomplished with the free flight tests. The major goals of the free flight tests are to:

- evaluate system robustness to disturbances,
- demonstrate waypoint navigation,
- implement optimal control techniques,
- assess effectiveness of adaptive control,
- measure dynamics of outer-loop control modes.

Approach

Now that the system is flying on its own, this set of testing focuses on pushing the boundaries of the vehicle capbilities. Determining what the current system is capable of is necessary information to progress to the next prototype design.

Disturbance Rejection: After flying with the proverbial safety net from the constrained tests, the first order of business will assess how robust the system is to disturbances. Wind gusts are the most notable disturbances the system must reject. However, the size of the vehicle makes outdoor flying a necessity, which is impossible to create a completely controlled environment. Furthermore, generating a static wind disturbance that acts on the entire vehicle is infeasible. As an alternative, a series of controlled experiments is presented. Consider a wind gust acting on the nose of a satellite. This creates a force that acts longitudinally. Force can also be applied longitudinally by adjusting the throttle command. To test this type of disturbance, code is added which scales up or down the motors outside the control loop. The control law is unaware of the motor scaling, and only acts on the measurements which indicate a tracking error. A similar test may evaluate the elevator channel by dropping a mass in the middle of a flight. The decreased payload simulates a force acting in the vertical direction, which the elevator must mitigate. These experiments can be easily modeled in the simulation environment, so collected data may further validate the computer model.

Waypoint Navigation: Knowing how much disturbance can be rejected leads into the next round of testing: waypoint navigation. Thus far, everything has focused on maintaining a hover equilibrium state. This test will assess the system dynamics outside of the hover condition. The test is extremely straight forward; start the vehicle in one location and command it to go to another point. The controller will be designed to have some prescribed response characteristics, like rise time, overshoot, damping ratio, etc. The goal is to compare the physical response to the prescribed dynamics and confirm that the controller is implementing the desired closed-loop dynamics.

Optimal Control: Once the vehicle is able to navigate to a new position, the next most pertinent issue is how efficiently it gets there. Early controllers use pole placement which exactly specifies the characteristic response. This strategy was used to reduce the risk with early flights by giving the controller enough authority to overcome any unexpected disturbances or modeling errors. However, this added security comes at the price of increased control energy. For an eternal flight vehicle, minimizing the amount of control effort is a primary consideration. Rather than using a pole placement feedback controller, the next test will implement an optimized control law where the gains are obtained through a linear quadratic regulator (LQR) design. The experiment runs the system with the same waypoint navigation, but collects data on the control signals used to navigate to that point.

Adaptive Control Assessment: Adaptive control is an important control technique to mitigate modeling uncertainty for both the prototype development and for the final full scale CSR vehicle. Understanding the capabilities and limitations of the adaptive controller is important to ensure stability and avoid unacceptable transient responses. Previous system identification tests yield the actual plant model dynamics. For this test, the controller gains are designed with slightly erroneous values. The controller should recognize that there is modeling error and adapt to the correct characteristics. Because the correct vehicle dynamics are already known, the adaptation can be evaluated against the true parameters.

Chapter 6

Conclusions

The Centrifugally Stiffened Rotor (CSR) concept is a unique configuration approach that has never previously been attempted, which could fundamentally lead to a new approach for High Altitude Long Endurance (HALE) or ATmospheric Satellite (AT-Sat) missions. AT-Sats map into many missions that existing GEO and LEO satellites simply can not perform, and in particular AT-Sats align with missions were communication transmission time needs to be minimized for such capabilities as omni-present wireless broadband.

The CSR significantly improved structural and aerodynamic efficiency open up the design space to become more feasible, with initial analysis indicating that feasibility may be possible through this concept approach in combination with energy storage of about 400 Whr/kg and thin-film solar cells around 35%. Feasibility relates to accomplishing year round missions at high U.S. latitudes.

The Phase I research focused on developing analysis tools capable of capturing the unique attributes of this multibody approach, including aerodynamic, structural, force balance, and power required. Performance comparisons were made with other HALE tool sets used in the analysis of DARPA Vulture concepts, as well as calibrations of the new tools to the most similar concepts.

The initial performance analysis indicates a reduction in power required on the order of 35% compared to the prior QinetiQ Zephyr 7 HALE endurance record holder, with the Zephyr carrying less than a 5% payload fraction compared to the CSR concept with a 10% payload.

A number of compelling missions have been identified that map directly into the unique capabilities of this advanced concept. Missions include:

Multi-Functional Airborne Wind and Surveillance Commercial Platforms at Lower Altitudes: Aerial platforms that operate at altitudes up to 2000 ft altitude (without FAA impediment of operational feasibility) that can both capture wind energy more effectively than ground-based wind turbines, and provide close proximity surveillance/communications with a coverage diameter of 50 miles. The CSR concept has the potential to achieve a higher Lift/Drag ratio compared to other airborne wind concepts, which results in higher tether angles and less land area underneath the vehicle radius of operation that depends on incoming wind direction. Off-shore application is particularly appealing since a CSR aerial vehicle would eliminate the need for a large/expensive mooring platform, which is required for ground-based wind turbines. The ability of this concept to have a non-moving tether from the ground to the center hub permits the inertial connection to be less complex than current airborne wind turbines. Potentially this mission concept could be applied all the way down to the level of distributed residential power production, with a sUAS sized version likely capable of providing 2 to

5 kW of power at altitudes of 500 feet with average wind speeds of less than 20 mph.

Distributed Aperture AT-Sat Observatory: The CSR concept provides a large rotating structure, as well as large volume at the center hub, with the capability of operation above the majority of the atmosphere. Integrating high resolution, compact, linked optic sensors (such as the Low Mass Planar Photonic Imaging Sensor currently being developed as Phase II NIAC research) at the tip and root of each rotor-wing will permit a rotating imaging array across a full 600 diameter azimuth. Combining this with a lower resolution conventional imaging system in the center hub for image filling could provide a resolution never before possible. Such an observatory could be designed as a dual-purpose system that provides imaging both upwards for space investigations, as well as for Earth imaging.

Extra-Planetary Compact VTOL Exploration Platforms: A version of the CSR concept has been identified that enables full retraction of the rotor-wing to achieve a highly compact VTOL vehicle that can operate at extremely low discloading (<0.03 lb/ft2) on atmospheres such as Mars that have atmospheric densities similar to Earth at 100,000 feet altitude. Because it was highly uncertain whether the centrifugal stiffening loads would be sufficient to maintain a rigid rotor-wing for this highly faceted spanwise design, a sub-scale version of the rotor-wing was fabricated and tested with success. The rotor-wing experiences an increase in weight and complexity with a decrement in performance to achieve compact packaging, however was shown to be a feasible approach that could facilitate very low discloading renewable VTOL aerial vehicles which could be packaged effectively in an aeroshell.

Since the performance analysis indicates a compelling advantage for this concept, the Phase I research focused on addressing the key risk area for this concept, establishing that vehicle control is feasible for this multibody dynamics problem. A complete derivation was presented which outlined how the CSR is modeled, the dynamics that dictate the equations of motion of the system, and a means of trimming and linearizing the system. This transitioned into the theory needed to control this particular vehicle, and simulations demonstrated the controller response implemented on the nonlinear system. The key hurdle to overcome from the controls point of view, is maintaining control when the exact relative position of the satellite is unknown. Estimation and reduced order estimators were shown to be able to overcome this, because the CSR vehicle was determined to be both fully controllable and fully observable. Furthermore, the system dynamics can be arbitrarily selected to meet any desired response within the limits of the actuators. Finally, parameter estimation and adaptive control techniques can be applied to this type of vehicle.

A sub-scale flight demonstrator at the 30 lbf gross weight size has been initiated to validate the ability of the control system to accommodate real world disturbances as well as winds and maintain stable flight. Additionally, the sub-scale prototype permits other study assumptions to be addressed, such as the mechanical complexity of the tether reel-in/out system which has not been analyzed. This demonstrator effort will continue as part of the PhD dissertation for the lead control researcher, and be completed prior to a follow-on proposal for Phase II research.